1225-0767(ISSN Print)
2287-6715(ISSN Online)
한국연구재단 우수등재학술지

Journal of Ocean Engineering and Technology

Vol. 37, No. 4 (Serial Number 173)

August 2023

한국해양공학회지

KSOE

www.joet.org

KSOE The Korean Society of Ocean Engineers

Journal of Ocean Engineering and Technology
한국해양공학회지
Vol. 37 No. 4
(Serial Number 173)
August 31, 2023
www.JOET.org

Published on August 31, 2023
Published by The Korean Society of Ocean Engineers (KSOE)
Room 1302, 13, Jungang-daero 180beon-gil, Dong-gu, Busan, 48821, Korea
TEL: +82-51-759-0656 FAX: +82-51-759-0657 E-mail: ksoehj@ksoe.or.kr URL: http://www.ksoe.or.kr
Printed by Hanrimwon Co., Ltd., Seoul, Korea E-mail: hanrim@hanrimwon.co.kr
ISSN(print) 1225-0767 **ISSN(online)** 2287-6715

This journal was supported by the Korean Federation of Science and Technology Societies (KOFST) grant funded by the Korean government.

Journal of Ocean Engineering and Technology
한국해양공학회지

CONTENTS

Volume 37, Number 4 August, 2023

<Original Research Articles>

<Technical Article>

GENERAL INFORMATION

The **"Journal of Ocean Engineering and Technology" (JOET)** was launched in 1987 and is published bimonthly in February, April, June, August, October, and December each year by "The Korean Society of Ocean Engineers (KSOE)." Its ISO abbreviation is "J. Ocean Eng. Technol." JOET publishes original research articles, technical articles, and review articles on all aspects of ocean engineering, including experimental, theoretical, numerical, and field observations. All manuscripts undergo peer-review by two or more reviewers.

The scope of JOET encompasses the following research areas:

- Ships and offshore engineering:

  Design of ships and offshore structures; Resistance and propulsion; Seakeeping and maneuvering; Experimental and computational fluid dynamics; Ocean wave mechanics; Fatigue strength; Plasticity; Optimization and reliability; Arctic technology and extreme mechanics; Noise, vibration, and acoustics; Concrete engineering; Thermodynamics and heat transfer; Hydraulics and pneumatics; Autonomous and unmanned ship; Greenship technology; Digital twin of ships and offshore structures; Marine materials

- Coastal engineering:

  Coastal, port, and harbor structures; Waves transformation; Coastal and estuary hydrodynamics; Sediment transport and morphological change; Subsea geotechnics; Coastal groundwater management; Prevention or mitigation of coastal disaster; Coastal zone development and management; Shore protection technique; Coastal environmental process; Beach safety

- Ocean energy engineering:

  Offshore wind turbines; Wave energy platforms; Tidal current energy platforms; Floating photovoltaic energy platform; Small modular reactor; Combined energy platforms

- Marine robot engineering:

  Robot sensor system; Autonomous navigation; Robot equipment; Marine robot control; Environment mapping and exploration; Underwater communication and networking; Design of marine robots

 It is indexed in databases such as the Korean Citation Index (KCI), Google Scholar, Science Central, Korea Science, and the Directory of Open Access Journals (DOAJ). JOET offers PDF or XML versions for free on its website (https://www.joet.org). For business matters, authors need to contact KSOE Secretariat by email or phone (e-mail: ksoehj@ksoe.or.kr or Tel: +82 51 759 0656). Correspondences for publication matters can be asked via email to the Editor-in-Chief (e-mail: heroeswise2@gmail.com).

KSOE

Journal of Ocean Engineering and Technology 37(4), 129-136, August, 2023
https://doi.org/10.26748/KSOE.2023.017

pISSN 1225-0767
eISSN 2287-6715

Original Research Article

Study on the Manoeuvring Performance of a Fishing Vessel Based on CFD Simulation of the Hull Forms and Rudder Shapes

Hyeonsil Choi[3], Soo Yeon Kwon[1,2], Sang-Hyun Kim[4] and In-Tae Kim[5]

[1]*Team leader, Safety Research Department/Fishing Vessel Safety Research Team of Korea Maritime Transportation Safety Authority, Sejong, Korea*
[2]*Doctor's Course, Department of Naval Architecture & Ocean Engineering, Inha University, Incheon, Korea*
[3]*Master's Course, Department of Naval Architecture & Ocean Engineering, Inha University, Incheon, Korea*
[4]*Professor, Department of Naval Architecture & Ocean Engineering, Inha University, Incheon, Korea*
[5]*Reserahcer, Safety Research Department of Korea Maritime Transportation Safety Authority, Sejong, Korea*

KEYWORDS: Manoeuvrability, Fishing vessels, Computational fluid dynamics (CFD), Hull forms, Rudder shapes

ABSTRACT: *To evaluate manoeuvring performance of merchant ships, the mathematical modeling group (MMG) or computational fluid dynamics (CFD) simulations are used. However, it is difficult to use the MMG to evaluate the manoeuvring performance of fishing vessels, thus research using CFD simulations is necessary. Also, since the course-changing and turning ability is crucial in fishing operations, a rudder design suitable for fishing vessels is necessary. This study designs a rudder using National Advisory Committee for Aeronautics (NACA) airfoil sections and evaluates its manoeuvring performance. A CFD model is used to evaluate the manoeuvring performance of the fishing vessel, and turning and zig-zag tests are conducted. The effectiveness of using CFD simulations based on Reynolds averaged Navier-Stokes equations to assess the manoeuvring performance of fishing vessels was validated. No significant difference was found in the manoeuvring performance for hull forms and rudder designs for course-changing ability. However, the original hull form showed superior turning performance. Among five rudders with varying aspect ratios and shapes, the rudder with 5.5% aspect ratio had the best turning performance. Regarding the rudder design for fishing vessels, NACA airfoil was employed, and a rudder aspect ratio of 5.5% based on the immersed hull side area is recommended.*

1. Introduction

The manoeuvring performance of merchant ships is estimated starting in the design stage through empirical equations using the principal dimensions of the ship, hydrodynamic derivatives obtained from a captive model test conducted using a model ship, a virtual captive model test using computational fluid dynamics (CFD), and mathematical modeling of the manoeuvring of the ship. For fishing vessels, on the other hand, most studies target constructed fishing vessels and estimate their manoeuvring performance through a comparison between a buoy bearing method using a real ship and differential global positioning system, an analysis of turning circle changes according to rudder angle and ship speed, and a zig-zag test. Research on estimating and evaluating manoeuvring performance in the design stage is scarce (Lee et al., 2018).

A study conducted on the manoeuvring performance characteristics of fishing vessels (Lee et al., 2018) used empirical equations and analyzed the effects of empirical equations on the estimation of the manoeuvring performance of fishing vessels. The authors used empirical equations considering stern shape and not considering stern shape in a turning movement simulation, and verified whether the manoeuvring performance standards of the International Maritime Organization (IMO) were satisfied. They further compared the results with the turning movements of a real ship. Their results showed that the IMO manoeuvring performance standards were satisfied, but a significant difference with the turning movement results of the real ship was found. The reason is attributable to the fact that the manoeuvring performance of fishing vessels was assessed based on the empirical equations of merchant ships; it was thus deduced that the parameters to estimate the manoeuvring performance of fishing vessels considering their shapes and motion characteristics arerequired. Kim et al. (2020) also performed a simulation on the

Received 5 June 2023, revised 1 July 2023, accepted 19 July 2023
Corresponding author Soo Yeon Kwon: +82-44-330-2570, kissiny@komsa.or.kr

turning movements of fishing vessels utilizing empirical equations consisting of the characteristics of hull shape parameters of fishing vessels. The simulation results showed a substantial error in turning movement estimation due to a difference in hull forms between merchant and fishing vessels. These results implied the necessity of empirical equations considering hull forms of fishing vessels to improve the estimation accuracy of turning performance.

In a study related to the rudder of fishing vessels, Kim et al. (2022) investigated the design practice of a rudder area for which assessment criteria and design standards were not clearly established among 153 fishing vessels operating in Korea, and statistically confirmed that the majority of fishing vessels were designed with a rudder area which does not satisfy international standards. Park et al. (2013) performed sea trials of fishing vessels equipped with a fiber-reinforced plastic (FRP) rudder and a square-shaped metal rudder, and verified that the FRP rudder outperformed the square-shaped metal rudder in turning when the rudder area was identical.

As explained above, the manoeuvring performance and rudder of fishing vessels have been investigated; however, insufficient efforts have been made on estimating hydrodynamic derivatives considering the hull form of fishing vessels in the design stage or assessing manoeuvring performance using a manoeuvring motion model. Furthermore, fishing vessels have large hydrodynamic nonlinearity depending on the changes in the submerged hull body and significant differences in hull forms according to fishing methods. Since there is a limitation in assessing manoeuvring performance by creating a manoeuvring motion mathematical model of the mathematical modeling group type, the manoeuvring performance of fishing vessels needs to be more directly assessed using a CFD simulation based on Reynolds averaged Navier-Stokes (RANS) equations. A proper rudder needs to be designed for fishing vessels since their veering and turning performance is particularly important considering their operation characteristics; however, there is insufficient data on principal dimensions and rudders for small fishing ships and on the correlation between the fishing ship and rudder. Therefore, a proper rudder design for small fishing ships must be devised by evaluating the changes in manoeuvring performance according to the rudder cross-section changes in the rudder area of fishing vessels.

This study directly assessed the manoeuvring performance of small fishing ships having various bow hull shapes using a RANS-based CFD simulation. A variety of rudder shapes were applied to fishing vessels to perform turning and zig-zag simulations, and rudder design measures were proposed considering changes in manoeuvring performance according to the rudder cross-section and area.

2. Manoeuvring Performance Assessment According to Hull Form

2.1 Target Vessel

The target vessel analyzed in this study was a 4.99-ton coastal fishing vessel in which three different types of bow hull–one chine original, bulbous bow, and spoon bow–were used as shown in Fig. 1. A model ship with the 1:11 ratio was used in the simulation, and the principal dimensions are presented in Table 1. The presented specifications are as follows. *Lpp* is the length, *B* is the width, *D* is the depth, *T* is the draft, *Fn* is the Froude number, *A* is the lateral area of the hull submerged below the waterline of the fishing vessel without a rudder, which was measured using a commercial CAD program. The lateral area of the submerged hull is shown in yellow lines in Fig. 2.

2.2 Shape and Specifications of a Plate Rudder

The principal dimensions and shape of the rudder, defined as a plate rudder, attached to the coastal gill netter fishing vessel analyzed in this study are presented in Table 2. A_R defined in Table 2 represents the lateral area of the rudder, which was directly calculated using a CAD program.

Table 1 Principal dimensions of model ships ((a), (b), and (c))

Item	Value
Scale ratio (-)	1/11
Design speed (m/s)	2.42
Lpp (m)	1.02
B (m)	0.27
D (m)	0.07
T (m)	0.05
Fn (-)	0.76
A (m^2)	0.07

(a) (b) (c)

Fig. 1 Gross tonnage (G/T) 4.99 gill netter fishing vessel: (a) One chine original, (b) Bulbous bow, and (c) Spoon bow

(a) (b) (c)

Fig. 2 Side view of a hull submerged below the waterline (a) One chine original, (b) Bulbous bow; and (c) Spoon bow

Table 2 Principal dimensions of plate rudder

Plate rudder	Item	Value
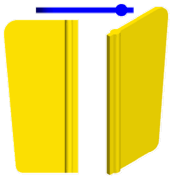	Chord mean (m)	0.495
	Span (m)	1.118
	Aspect ratio (-)	2.26
	Thickness (m)	0.033
	A_R (m^2)	0.553
	A_R/A (%)	6.5

2.3 CFD Model Verification: Resistance Simulation

Before performing the free-running simulation in calm water, a resistance simulation was performed for verifying the CFD model of the target vessel in this study. The computational domain for the simulation is shown in Fig. 3. The computational domain was set to satisfy the recommended procedures and guidelines of the International Towing Tank Conference (ITTC) (ITTC Resistance Committee, 2017). The length from the center of the vessel to the bow is 5.5 *Lpp*, 12.5 *Lpp* toward the stern, 7.5 *Lpp* toward the port side and the starboard side, and 5.0 *Lpp* toward the bottom and the deck each the boundary conditions of each boundary in the computational domain are shown in Table 3.

For the simulation, commercial CFD software STAR-CCM+(16.06 ver) was used. To create a mesh, the trimmed mesh and prism layer features of STAR-CCM+ were used. The mesh density was set differently using the trimmed mesh feature depending on the flow characteristics. A boundary layer mesh was used around the hull and on the surface to ensure that the flow at the boundary layer was accurately calculated. Furthermore, the dynamic fluid body interaction

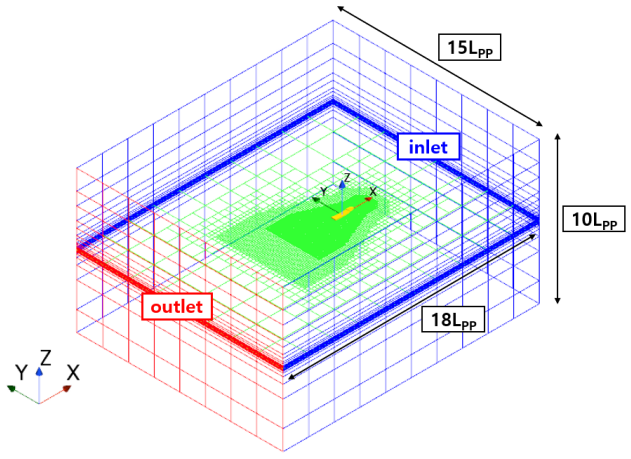

Fig. 3 Computational domain

Table 3 Boundary condition

Boundary	Boundary condition
Inlet, Side, Top, Bottom	Velocity inlet
Outlet	Pressure outlet
Ship	Wall

Table 4 Total resistance comparison according to hull forms

Hull forms	Total resistance (N)	C_{TM} (e-3)
One chine original	13.72	12.73
Bulbous bow	13.35	12.47
Spoon bow	13.47	12.50

feature was used to consider the changes in the position of the hull, and an overset mesh was used to discretize the entire computational domain on the hull movement. The volume of fluid feature was used to consider multiphase flows to implement the free surface.

In Table 4, The total resistance of a ship is nondimensionalized and described using the C_{TM}, and it can be calculated through Eq. (1). In Eq. (1), v, ρ, and Aw represent the design speed of the ship, water density, and the wetted surface area of the ship, respectively.

As shown in Table 4, the resistance simulation result demonstrated that resistance decreased in the order of one chine original, spoon bow, and bulbous bow, and the resistance performance of the bulbous bow was most outstanding.

Fig. 4, Fig. 5, and Fig. 6 illustrate the wave patterns of each hull form generated during the resistance simulation.

$$C_{TM} = \frac{Total\,resistance}{0.5\rho A_w v^2} \quad (1)$$

2.4 Turning Simulation According to Hull Form

A starboard +35° turning simulation was performed to evaluate the turning performance according to hull forms. The turning trajectory, which is the simulation result, is illustrated as a dimensionless value in Fig. 7; the comparison of advanced length and tactical diameter of each hull form is presented in Table 5. The turning radius according to the hull form increased in the order of one chine original, bulbous bow, and spoon bow. The turning performance was compared between the hull forms with respect to the tactical diameter and advance length, which are the turning performance indicators. The one chine original form exhibited the most outstanding turning performance. Because the resistance performance of the one chine original form was the least

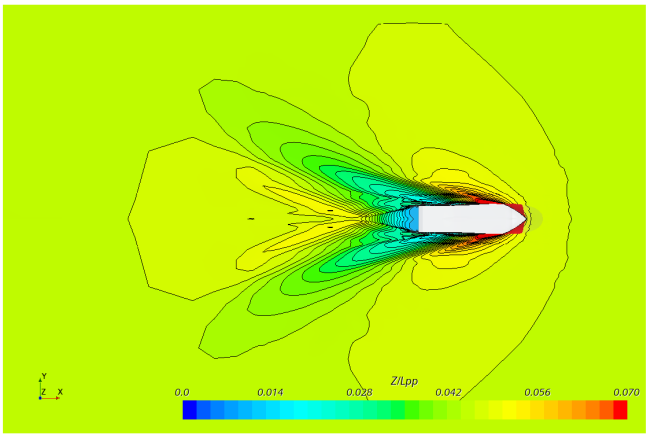

Fig. 4 Wave pattern of one chine original

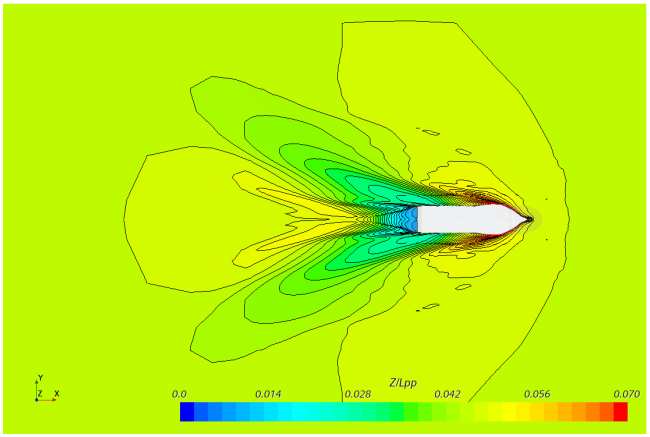

Fig. 5 Wave pattern of bulbous bow

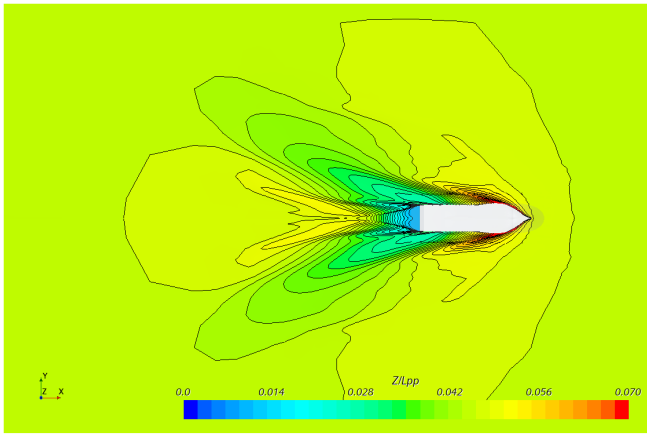

Fig. 6 Wave pattern of spoon bow

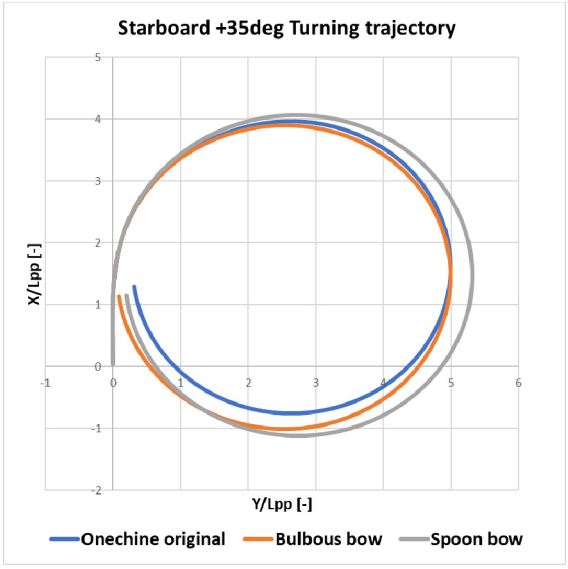

Fig. 7 Trajectory according to hull forms

Table 5 Turning performance of hull forms

Hull forms	Tactical dimeter	Advancae length
One chine original	4.68 *Lpp*	3.97 *Lpp*
Bulbous bow	4.91 *Lpp*	3.90 *Lpp*
Spoon bow	5.12 *Lpp*	4.07 *Lpp*

outstanding, the relatively larger thrust and wake fraction of the propeller compared to other hull forms increased the direct compressive force of the rudder resulting in excellent turning performance.

2.5 Zig-zag Simulation According to Hull Form

A -10°/10° zig-zag simulation was performed to evaluate the veering performance according to hull forms. The simulation results are summarized in Fig. 8 and Table 6; only a minor difference in the veering performance was found between the three hull forms of one chine original, bulbous bow, and spoon bow. The 1st overshoot angle, which is the veering performance indicator, decreased in the order of the bulbous bow, one chine original, and spoon bow, and all three hull forms satisfied the IMO standard, which implies that the target vessel has adequate veering performance and course stability performance as a fishing vessel.

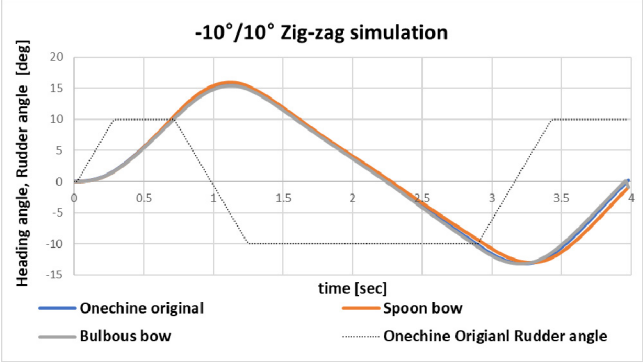

Fig. 8 Heading angle and rudder angle of hull forms

Table 6 Results of overshoot angles of zig-zag manoeuvring

Hull forms	1st overshoot (deg)	2nd overshoot (deg)
One chine original	5.57	-3.24
Bulbous bow	5.97	-2.97
Spoon bow	5.44	-3.20

3. Modeling of Rudder Shape Having Various Cross-Sections and Aspect Ratios

3.1 Rudder Shape Modeling by Applying NACA Cross-Section

The cross-section was varied to model five rudder shapes to evaluate the manoeuvring performance with respect to the rudder cross-section. The National Advisory Committee for Aeronautics (NACA) airfoil cross-section was applied to increase the lateral force applied to the rudder. For the comparison with a plate rudder which was previously used in the manoeuvring performance simulation evaluation according to hull form, the thickness of the rudder cross-section was varied with respect to NACA0006 having the same maximum thickness as the plate rudder in which the rudder shape was modeled using five cross-sections: NACA0003, NACA0006, NACA0010, NACA0012, and NACA0025. The respective results are shown in Table 7.

Table 7 The cross-sectional shape and specifications of a rudder

Rudder shape	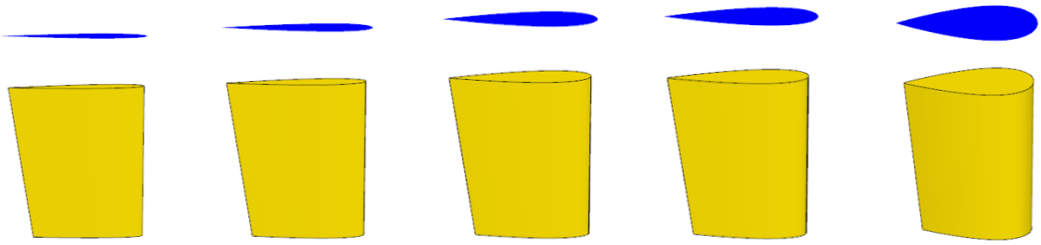				
Rudder section	NACA 0003	NACA 0006	NACA 0010	NACA 00012	NACA 0025
Chord mean (m)			0.495		
Span (m)			1.118		
Aspect ratio (-)			2.26		
A_R (m^2)			0.553		
A_R/A (%)			6.5		

3.2 Comparison of Lateral Force on the Rudder According to Rudder Cross-Sectional Shape

For comparing the performance between the rudder modeled in Section 3.1 and the plate rudder, the lateral force acting on the rudder was calculated by changing the steering angle from 10° to 40° at the increment of 10°. The lateral forces on the rudder having NACA cross-section and the plate rudder are shown in Fig. 9. The maximum lateral force occurred at 30° in all rudders, and the lateral force decreased beyond 30° due to the occurrence of the stall. Additionally, the NACA0006 rudder having the same thickness as the plate rudder 0006 receives a greater lateral force than the plate rudder, thus being more advantageous in terms of improving the manoeuvring performance of fishing vessels.

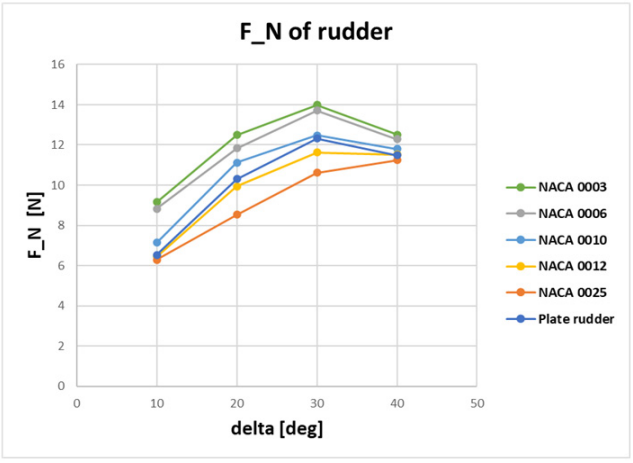

Fig. 9 Lateral force on the rudder at various angles

3.3 Modeling of Rudder Shapes Having Various Aspect Ratios

From the calculated lateral force applied to the plate rudder and five rudders having NACA cross-sections, rudder shape modeling was performed by changing the rudder area of the NACA0003 rudder, which had the highest lateral force. Based on 6.5% aspect ratio (A_R/A) of the lateral area of the submerged hull to the rudder area of the plate rudder, the aspect ratio of five rudder shapes was varied by 4.5%, 5.5%, 6.5%, 7.5%, and 8.5% to model the rudder shape. The constraint of rudder span caused by the stern shape was taken into consideration

Table 8 Shape and specifications of rudders for various aspect ratio

Rudder shape	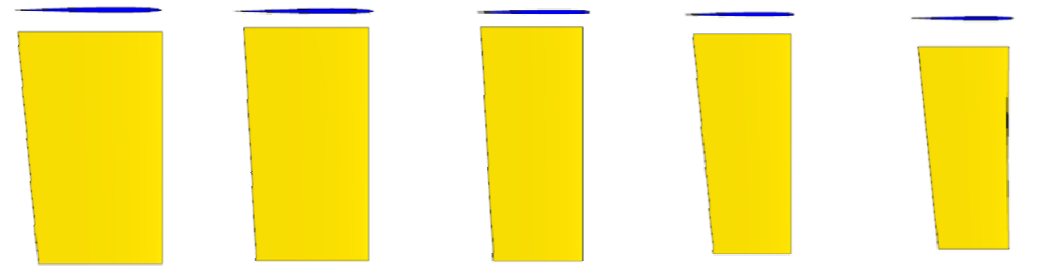				
Rudder type	NACA0003 8.5%	NACA0003 7.5%	NACA0003 6.5%	NACA0003 5.5%	NACA0003 4.5%
Chord mean (m)	0.645	0.565	0.490	0.430	0.393
Span (m)	1.118	1.118	1.118	1.075	0.975
Aspect ratio (-)	1.7	2.0	2.3	2.5	2.5
A_R (m^2)	0.721	0.632	0.548	0.462	0.380
A_R/A (%)	8.5	7.5	6.5	5.5	4.5

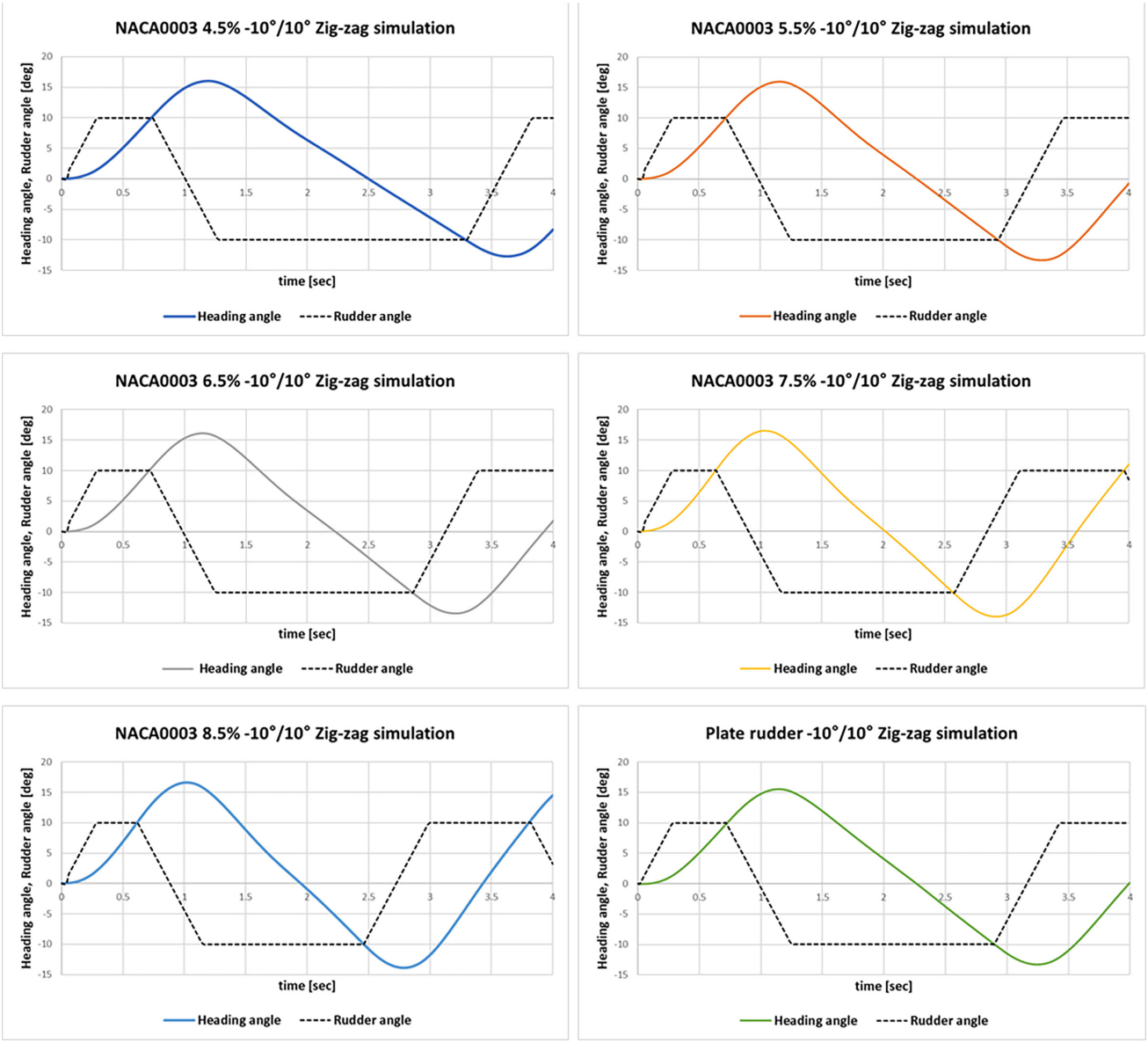

Fig. 10 Heading angle and rudder angle of rudder aspect ratio

in the rudder modeling, and a larger aspect ratio was assigned to the same rudder area considering the lift characteristics. The shape and specifications of the modeled rudders are shown in Table 8.

4. Manoeuvring Performance Assessment According to Rudder Aspect Ratio

4.1 Zig-zag Simulation Results According to Rudder Aspect Ratio

To assess the veering performance of rudders having various aspect ratios as modeled in Section 3.3, a -10°/10° zig-zag simulation was performed for the one chine original form, which demonstrated the best manoeuvring performance; the relevant results are illustrated in Fig. 10 and Table 9. As shown in the results of the zig-zag simulation, the overshoot angle increased as the rudder aspect ratio increased. However, IMO manoeuvring performance standards for vessels of *Lpp* 100 m or above were satisfied in all rudder aspect ratios. Therefore, sufficient veering performance and course stability were expected when the NACA003 cross-sectional rudder, having five aspect ratios modeled in this study, was applied to the target fishing vessel.

Table 9 Results of overshoot angles of zig-zag manoeuvrs

Rudder type	1st overshoot (deg)	2nd overshoot (deg)
NACA0003 4.5%	5.96	-2.71
NACA0003 5.5%	6.04	-3.33
NACA0003 6.5%	6.16	-3.40
NACA0003 7.5%	6.51	-3.94
NACA0003 8.5%	6.59	-3.90

4.2 Turning Simulation Results According to Rudder Aspect Ratio

To assess the turning performance of rudders having various aspect ratios as modeled in Section 3.3, a +35° turning simulation was

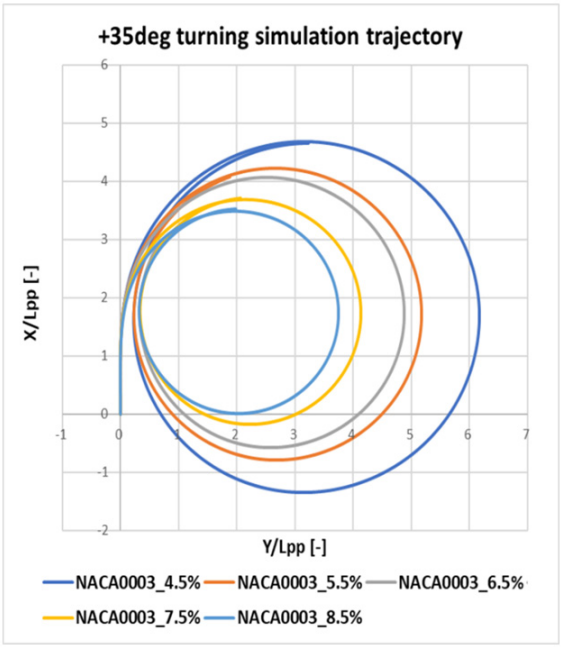

Fig. 11 Trajectory according to the aspect ratio of rudders

Table 10 Turning performance of rudder aspect ratio

Rudder type	Tactical diameter	Advance
NACA0003 4.5%	5.93 *Lpp*	4.69 *Lpp*
NACA0003 5.5%	5.05 *Lpp*	4.22 *Lpp*
NACA0003 6.5%	4.53 *Lpp*	4.08 *Lpp*
NACA0003 7.5%	3.77 *Lpp*	3.72 *Lpp*
NACA0003 8.5%	3.40 *Lpp*	3.53 *Lpp*

performed for the one chine original form, which demonstrated the best manoeuvring performance. The turning trajectory, which is the simulation result, is illustrated as a dimensionless value in Fig. 11; the tactical diameter and advance length are summarized in Table 10. As shown in the turning simulation results, both tactical diameter and advance length decreased as the rudder aspect ratio increased, in which NACA0003 6.5%, 7.5%, and 8.5% rudders all satisfied the IMO manoeuvrability standard requirements. NACA0003 4.5% and NACA003 5.5% rudders did not satisfy the IMO manoeuvrability standard requirements; however, the IMO standard targets vessels of *Lpp* 100m or above. Therefore, the target vessel is deemed to have sufficient turning performance considering that it is a small fishing ship with a small *Lpp*.

As shown in Table 10, the tactical diameter decreased by 16.78% and 14.84% when the rudder aspect ratio increased from 6.5% to 7.5% and from 4.5% to 5.5%, respectively. However, the aspect ratio decreased from 2.3 to 2.0 owing to the constraint of the stern shape when the aspect ratio was 7.5%. This is disadvantageous from the perspective of rudder lift characteristics and resistance performance of fishing vessels. Thus, the most efficient change in the aspect ratio for the target vessel is an increase from 4.5% to 5.5% in terms of manoeuvring performance.

5. Conclusion

This study assessed the manoeuvring performance of a small fishing vessel having various hull forms using a CFD simulation, aiming the propose the design direction for the rudder shape of fishing vessels by considering the changes in the manoeuvring performance according to cross-sectional shape and area of rudders. The following conclusions were drawn.

First, turning and zig-zag simulations were carried out using CFD to assess the manoeuvring performance of fishing vessels. Without the use of empirical equations or an MMG manoeuvring motion model, the effectiveness of directly assessing the manoeuvring performance of fishing vessels using a RANS-based CFD simulation was verified.

Second, turning and zig-zag simulations were performed for three types of hull forms–one chine original, bulbous bow, and spoon bow – to evaluate manoeuvring performance according to hull form. The simulation results showed that the manoeuvring performance was in the order of one chine original, bulbous bow, and spoon bow. The hull form of the fishing vessel must be determined by comprehensively reviewing the manoeuvring performance as well as resistance and self-propulsion performance.

Third, when the manoeuvring performance was compared according to the changes in rudder cross-sectional shape, the rudders with NACA cross-section outperformed the plate rudder in terms of lateral force and manoeuvring performance, particularly in terms of turning performance. Furthermore, the manoeuvring performance assessment conducted according to rudder shape confirmed that the improvement of manoeuvrability with respect to 1% increase in rudder aspect ratio was the most efficient for the rudder aspect ratio of (A_R/A) 5.5%.

Therefore, this study suggests the design of the rudder in fishing vessels employs NACA cross-section and the rudder area to adopt the aspect ratio (A_R/A) that reflects the lateral area of the submerged hull. This study also proposes the selection of the rudder aspect ratio that results in the most efficient improvement of the manoeuvring performance with respect to the increase in the rudder area. However, the cross-section and area of the rudder cannot be simply determined based on the lift characteristics and manoeuvring performance; thus, further research is required on rudder shape design of small fishing vessels by comprehensively considering rudder span according to stern shape, constraints of chords, structural stability, and productivity of the rudder.

Conflict of Interest

No potential conflict of interest relevant to this article was reported.

Funding

This research was funded and conducted under 「the Competency Development Program for Industry Specialists」 of the Korean Ministry of Trade, Industry and Energy (MOTIE), operated by Korean

Institute for Advancement of Technology (KIAT). (No. P0012646, HRD program for Global Advanced Engineer Education Program for Future Ocean Structures)「Development and demonstration of data platform for AI-based safe fishing vessel design (202202102)」of the Ministry of Oceans and Fisheries, Republic of Korea.

References

ITTC Resistance Committee. (2017). Uncertainty analysis in CFD verification and validation methodology and procedures. *ITTC - Recommended Procedures and Guidelines*, 1−13.

Kim, M. R., Woo, D. H., & Im, N. K.(2022). Analysis of the design of rudder aspect ratio for domestic fishing vessel. *Journal of the Korean Society of Marine Environment & Safety, 28*(2), 235−243. https://doi.org/10.7837/kosomes.2022.28.2.235

Lee, C. K., Kim, S. H., Lee, J. G., Lee, S. M., & Kim, M. S.(2018). A study on the characteristics of maneuverability of fishing vessel. Journal of the Korean Society of Fisheries and Ocean Technology*l, 54*(3), 239−245. https://doi.org/10.3796/KSFOT.2018.54.3.239

Kim, S. h., Lee, C. K., & Kim, M. S.(2020). A study on the characteristics of hull shape parameter of fishing vessel types. *Journal of the Korean Society of Fisheries and Ocean Technology, 56*(2), 163−171. https://doi.org/10.3796/KSFOT.2020.56.2.163

Park, C. H., Jang, H. Y., Park, M. S., & Im, N. K.(2013). Result analysis of sea trial test for offshore fishing boat attached FRP rudder. *Journal of Ocean Engineering and Technology, 27*(6), 112−118. https://doi.org/10.5574/KSOE.2013.27.6.112

Author ORCIDs

Author name	ORCID
Choi, Hyeonsil	0000-0002-5882-8674
Kwon, Soo Yeon	0000-0002-5928-7101
Kim, Sang-Hyun	0000-0002-3625-2328
Kim, In-Tae	0000-0003-1382-3471

KSOE

Journal of Ocean Engineering and Technology 37(4), 137-144, August, 2023
https://doi.org/10.26748/KSOE.2023.009

pISSN 1225-0767
eISSN 2287-6715

Original Research Article

Visualization of Turbulent Flow Fields Around a Circular Cylinder at Reynolds Number 1.4×10^5 Using PIV

Jun-Hee Lee[1], Bu-Geun Paik[2], Seok-Kyu Cho[2] and Jae-Hwan Jung[3]

[1]*Ph.D. Student, Department of Naval Architecture & Ocean Engineering, Inha University, Incheon, Korea*
[2]*Principal Researcher, Korea Research Institute of Ships & Ocean Engineering, Daejeon, Korea*
[3]*Senior Researcher, Korea Research Institute of Ships & Ocean Engineering, Busan, Korea*

KEYWORDS: Circular cylinder, Turbulent flow fields, PIV (Particle image velocimetry), High Reynolds number, Cavitation tunnel

ABSTRACT: *This study investigates the experimental parameters of particle image velocimetry (PIV) to enhance the measurement technique for turbulent flow fields around a circular cylinder at a Reynolds number (Re) of 1.4×10^5. At the Korea Research Institute of Ships & Ocean Engineering (KRISO), we utilized the cavitation tunnel and PIV system to capture the instantaneous flow fields and statistically obtained the mean flow fields. An aspect ratio and blockage ratio of 16.7% and 6.0%, respectively, were considered to minimize the tunnel wall effect on the cylinder wakes. The optimal values of the pulse time and the number of flow fields were determined by comparing the contours of mean streamlines, velocities, Reynolds shear stresses, and turbulent kinetic energy under their different values to ensure accurate and converged results. Based on the findings, we recommend a pulse time of 45 μs corresponding to a particle moving time of 3–4 pixels, and at least 3,000 instantaneous flow fields to accurately obtain the mean flow fields. The results of the present study agree well with those of previous studies that examined the end of the subcritical flow regime.*

1. Introduction

Circular cylinders, one of the shapes that are commonly used to represent bluff bodies, are targets that provide the most fundamental physical insight to improve the hydrodynamic performance' of engineering systems. Since the 1960s, many studies have been conducted to understand the load and flow characteristics of cylinders (Roshko, 1961; James et al., 1980; Schewe, 1983; Williamson, 1996; Zdravkovich, 1997; Chen, 2022).

Although the study of flow characteristics around a cylinder is a traditional problem, research on this subject has been conducted until recently because in spite of the simple geometry, the flow characteristics are extremely complex and highly dependent on the Reynolds number (*Re*). These characteristics are very important for evaluating the fluid performance of marine structures or risers that have basic cylinder geometry because they are the direct cause of the scale effect that may occur between a model and a full-scale ship.

Most previous studies have considered the subcritical flow regime, where the wakes are turbulent while the boundary layers are laminar on the object surface, in the range $10^3 \leq Re \leq 10^4$.

In recent years, several studies have focused on flow with $Re \geq 10^5$ as well as in the critical and supercritical regimes (van Hinsberg, 2015; van Hinsberg et al., 2018). The highest Reynolds number in the sub-critical regime, i.e., 10^5, has engineering significance and can be actually observed when a riser or marine structure column support is considered with its characteristic length.

The Strouhal number is maintained at 0.2 in the sub-critical regime (Blevins, 1977) because the vortex shedding period decreases due to rapid turbulent transition in wakes with increase in the velocity. Therefore, the flow characteristics at a relatively higher Reynolds number of 10^5 can be predicted through existing flow field measurement studies within $10^3 \leq Re \leq 10^4$. However, actual flow field measurements can provide direct clues to understand the flow characteristics in wakes according to the change in position of turbulent transition. This may hold importance as an experimental data base (DB) for validation with recent developments in computational fluid dynamics. Most studies conducted at a Reynolds number of approximately 10^5 (Schewe, 1983, van Hinsberg, 2015, van Hinsberg

Received 17 April 2023, revised 21 June 2023, accepted 19 July 2023
Corresponding author Jae Hwan Jung: +82-51-604-7828, jaehwan@kriso.re.kr
It is noted that this paper is revised edition based on 2018 Fall Conference of The Korean Society of Visualization in Pusan (Lee et al., 2018).

et al., 2018) were focused on changes in load characteristics. However, there is insufficient experimental data on flow characteristics around a cylinder, which are the fundamental cause of load change. In this regard, particle image velocimetry (PIV) is a very useful method for measuring the flow field around a cylinder. Due to a lack of related studies at $Re \approx 10^5$, research on PIV measurement techniques is required for the accurate measurement of flow fields in cylinder wakes.

In this study, we focused on the PIV technique and visualization to accurately measure the flow fields in cylinder wakes prior to constructing the flow field DB at a Reynolds number of 10^5. The flow field measurement characteristics were evaluated in great detail according to the measurement times of particle images (which were experiment variables) and the number of instantaneous flow fields used to obtain mean flow fields. This helped to investigate the basic characteristics of the PIV technique for precise flow field measurement. The reliability of the PIV technique established in this study was verified through a comparison with previous studies at the same Reynolds number.

2. Experimental Setup and Method

Fig. 1 shows the experimental setup of the cavitation tunnel in the Korea Research Institute of Ships & Ocean Engineering (KRISO). The test section of the tunnel had a size of 0.6^{W} m × 0.6^{H} m × 2.6^{L} m. The maximum flow velocity in the section was 12 m/s, and the static pressure in the section was varied from 10.1 kPa to 202 kPa. The uniformity of the free flow introduced into the test section had an error rate less than 1%.

The cylinder diameter (D) was 36 mm and the aspect ratio (L/D; L is the cylinder span length) was 16.7. The blockage ratio (D/H), which is the ratio of the diameter of the horizontally placed circular cylinder to the height of the tunnel test section (H), was 6.0%. First, we identified the pulse time ($\triangle t$) and number of instantaneous flow fields suitable to measure the characteristics of flow fields around the cylinder in order to investigate the basic characteristics of the PIV technique and obtain the mean velocity fields. Table 1 summarizes the experimental conditions to examine the basic characteristics of the PIV technique.

In PIV, the velocity vector is obtained by calculating the pulse time ($\triangle t$) of two particle images and the distance traveled by a scattering particle. The change in $\triangle t$ is strongly related to the accuracy of calculation of the particle velocity vector according to the length and time scale of rapidly moving turbulence. In general, a pulse time that corresponds to less than one-tenth of the time required for a scattering particle to pass through the measurement area is adopted. The selection of scattering particles in the measurement area of the cylinder wake (according to the research objective) affects the measurement of flow fields (Park and Kwak, 2004; Paik et al., 2007; Paik et al., 2010). Fig. 2 shows a schematic on the generation of velocity vectors according to the pulse time. In the figure, when a fluid particle is assumed to flow from point 1 to point 4, it is possible to identify its movement path and obtain accurate velocity vectors according to the pulse time. In this study, we selected scattering particles in the wake area, where the velocity was decreased by the generation of Kármán vortex street. The pulse time corresponding to a scattering particle traveling one-tenth (three to four pixels) of the interrogation window was applied, and its value was 45.0 μs. In addition, pulse times that were 0.25 and 4 times of the pulse time of 45.0 μs (11.25 and 180.0 μs) were considered to examine the dependency of flow field measurement on the pulse time at $Re = 1.4 \times 10^5$.

Fig. 3 shows the PIV system installed to measure the flow in the cylinder wakes. The two-dimensional (2D) PIV system for velocity field measurement consisted of Dantec's dual-pulsed Nd:Yag laser (200 mJ/pulse), a high-resolution charge-coupled device (CCD) camera with 2048 × 2048 pixels, a camera transport system, an image processing system, and computers for control and computation. Titanium dioxide (TiO_2) scattering particles were used. A laser light sheet was irradiated from the bottom of the cavitation tunnel and the camera was placed on the left side of the tunnel to capture particle images in the measurement area of 140 × 140 mm^2 (Fig. 3); 16,129 velocity vectors were obtained from the velocity fields calculated using a PIV algorithm (adaptive correlation). The size of the interrogation window was 32 × 32 pixels, and the spatial resolution of the velocity fields was increased using the 50% overlapping technique. The effective spatial resolution was 0.907 mm, which represents the distance between velocity vectors. During PIV postprocessing, the error vector was treated using the dynamic mean value operator, a representative algorithm (Lee, 1999). As shown in Fig. 3, a laser light sheet was irradiated from the bottom of the test section. Thus, it was deemed difficult to accurately calculate the velocity vector in a few areas at the top of the cylinder because the light sheet was not formed. Therefore, a flat mirror was installed on the upper plate window of the test section to induce reflection of the laser light sheet and form the light sheet in the upper part of the cylinder. This made it possible to calculate the velocity vector in the upper part. In this study, the Reynolds number was fixed at 1.4×10^5 for comparison with previous studies. To implement the corresponding flow conditions, a flow velocity of 4.5 m/s was considered in the tunnel.

Fig. 1 Schematic diagram of the cavitation tunnel.

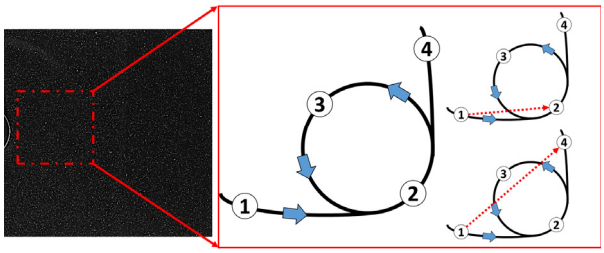

Fig. 2 Schematic of particle paths according to pulse time.

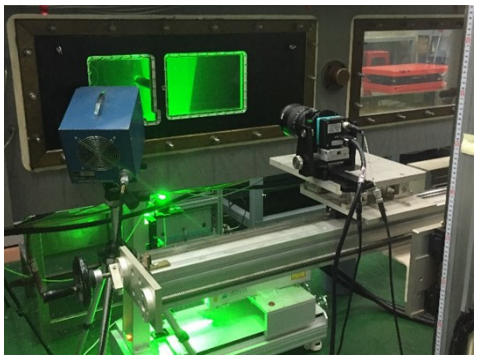

Fig. 3 Experimental setup of the PIV system.

Table 1 Test cases regarding the experiment parameters.

Test No.	$\triangle t$ (μs)	Number of velocity fields	Trigger rate (Hz)
1	11.25	3000	7
2	45.0	3000	
3	180.0	3000	
4	45.0	100	
5	45.0	500	
6	45.0	1000	

3. Experimental Results

To examine the effects of change in pulse time ($\triangle t$) on the measurement of mean streamlines, streamwise velocity, crosswise velocity, $u'v'$ Reynolds shear stress, and the turbulent kinetic energy distribution field, the measurement results according to the pulse time are shown in Fig. 4. The aforementioned physical quantities were obtained using 3,000 instantaneous velocity fields and the Reynolds number was 1.4 × 10^5. The observation of the mean streamlines is shown in Fig. 4(a). The recirculation length, l_C, is approximately 1.3D ± 0.05D regardless of the change in pulse time, but the central positions of the upper and lower vortices of the separation bubble differ depending on the pulse time. In particular, the central positions of the upper and lower vortices are asymmetric when $\triangle t$ is 11.25 μs and 180 μs, but the difference decreases and a symmetric tendency is observed at a pulse time of 45.0 μs. As no particular trend is observed according to the increase in pulse time, it is necessary to further examine the relationships among the spatial distribution of the flow velocity in the test section, the formation of the light sheet in the upper part of the cylinder due to the installation of the mirror, and the pulse time in order to analyze the cause of the results. In addition, from Figs. 4(b) and 4(c), it is evident that the pulse time ($\triangle t$) also affects the mean streamwise velocity and mean crosswise velocity distribution characteristics. Due to the formation of the separation bubble, negative and positive velocity changes are observed in the streamwise direction. For pulse times of 11.25 μs and 45.0 μs, a negative velocity that corresponds to 25% of the free flow velocity is measured inside the separation bubble, which is in agreement with the result of a previous study by Braza et al. (2006). However, at 180 μs, a negative velocity that corresponds to approximately 10% of the free flow velocity is measured. This indicates that the velocity change in the separation bubble as a result of the time average of the Kármán vortex street could not be properly measured at the pulse time of 180 μs. From Fig. 4(c), it is also evident that the rapid crosswise velocity change in the range -0.25 ≤ v/U ≤ 0.25 could not be correctly measured at a pulse time of 180 μs compared to the results of the other pulse times.

Unlike the streamwise and crosswise velocity distributions for

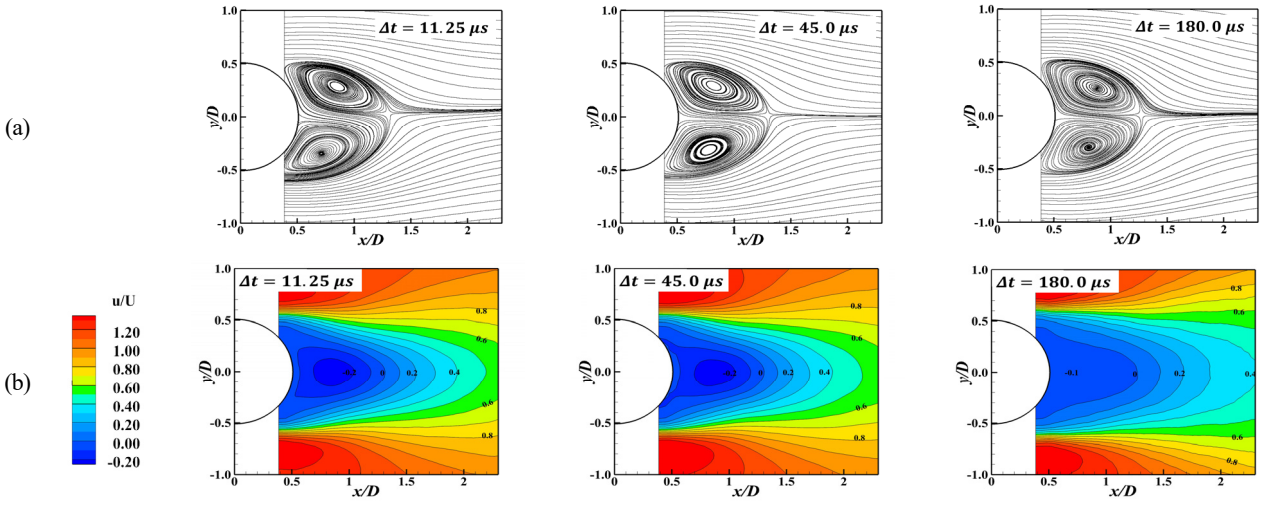

Fig. 4 Comparison of flow fields for different pulse times: (a) mean streamlines, (b) mean streamwise velocity, (c) mean crosswise velocity, (d) $u'v'$ Reynolds shear stress, and (e) turbulent kinetic energy.

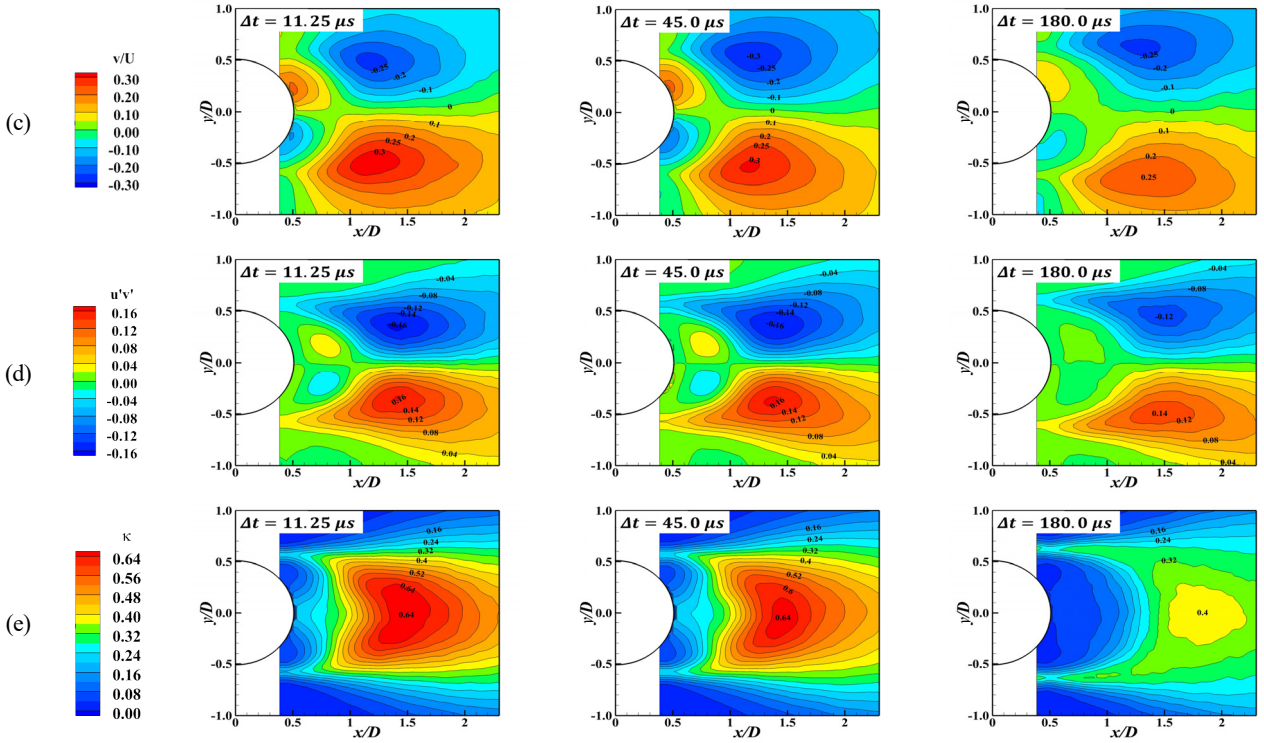

Fig. 4 Comparison of flow fields for different pulse times: (a) mean streamlines, (b) mean streamwise velocity, (c) mean crosswise velocity, (d) $u'v'$ Reynolds shear stress, and (e) turbulent kinetic energy. (Continuation)

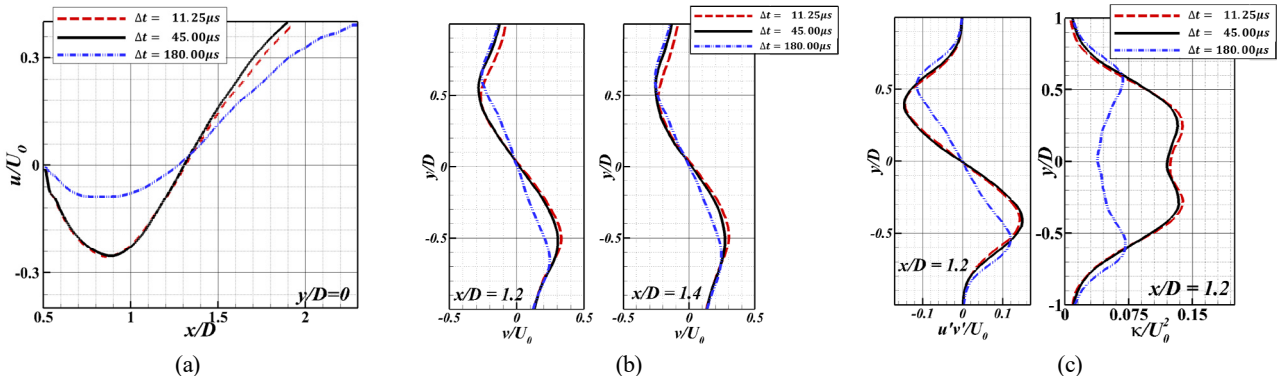

Fig. 5 Comparison of physical quantities for different pulse times: (a) mean streamwise velocity, (b) mean crosswise velocity, (c) $u'v'$ Reynolds shear stress, and (d) turbulent kinetic energy

which the time average values are important, the $u'v'$ Reynolds shear stress and turbulent kinetic energy depend on the perturbation of the turbulent velocity. As shown in Figs. 4(d) and 4(e), the pulse time affects the mean flow fields to which the velocity perturbation information is reflected. The occurrence of the Kármán vortex street with turbulent characteristics complicates the movement paths of the scattering particles by causing interactions of time-dependent multi-scale vortices. In such instances, an increase in the pulse time leads to an increase in the calculation error of the velocity vector and hence, failure to accurately capture the velocity perturbation change within a short period of time. In particular, the pulse time of 180.0 μs, which is approximately 16 times and 4 times larger than 11.25 μs and 45.0 μs, makes it difficult to accurately measure flow fields in the Kármán vortex street area where anisotropic vortices are generated and strong momentum exchange occurs. This causes positive and negative mean velocities. The turbulent kinetic energy is measured lower than the actual value and the $u'v'$ Reynolds shear stress distribution is longer in the downstream direction in the flow field results obtained through the average of 3,000 instantaneous flow fields.

Fig. 5 shows the streamwise and crosswise velocity, Reynolds shear stress, and turbulent kinetic energy distributions in the centerline of the cylinder according to the pulse time for a quantitative comparison. Here, for x/D, which corresponds to the boundary of the separation bubble, changes in physical quantities are considered at 1.2 and 1.4 according to y/D. Interestingly, from Fig. 5, it is evident that convergence is achieved at 45 μs for all the physical quantities. This indicates that an appropriate pulse time in consideration of the flow characteristics is required in PIV measurement. Fig. 5(a) shows the

streamwise velocity distribution. The recirculation length, which is the distance between the center of the cylinder and the position where the velocity changes to zero, is consistent regardless of the pulse time, $\triangle t$, but there is a significant difference in the velocity distribution. In particular, when the pulse time is lower than the time of approximately one-tenth of the interrogation window, the dimensionless negative velocity in the recirculation area increases to 0.25 and rapidly recovers positive velocity at $x = 1.3D$ or higher, which exceeds the recirculation area. However, at a pulse time of 180 μs, relatively small negative and positive velocity distribution is observed in Fig. 5(a), confirming that the correct velocity distribution could not be measured. For the other physical quantities, the least favorable results are observed for a pulse time of 180 μs. In particular, there are significant differences in the turbulent kinetic energy distribution compared to the results for other pulse times. For a pulse time of 45.0 μs, the movement speed of scattering particles corresponds to one-tenth of the interrogation window (three to four pixels). Consequently, a particle moving distance of three to four pixels, which was proposed in previous studies (Park and Kwak, 2004; Paik et al., 2007; Paik et al., 2010), is adhered to in this study.

After fixing the pulse time at 45.0 μs, the flow field measurement characteristics were compared by additionally considering 500, 1,000, and 2,000 instantaneous velocity field samples for the time average. First, for a qualitative comparison, similar to the comparison of physical quantities in Fig. 4, the mean streamlines, streamwise and crosswise velocity distributions, $u'v'$ Reynolds stress distributions, and

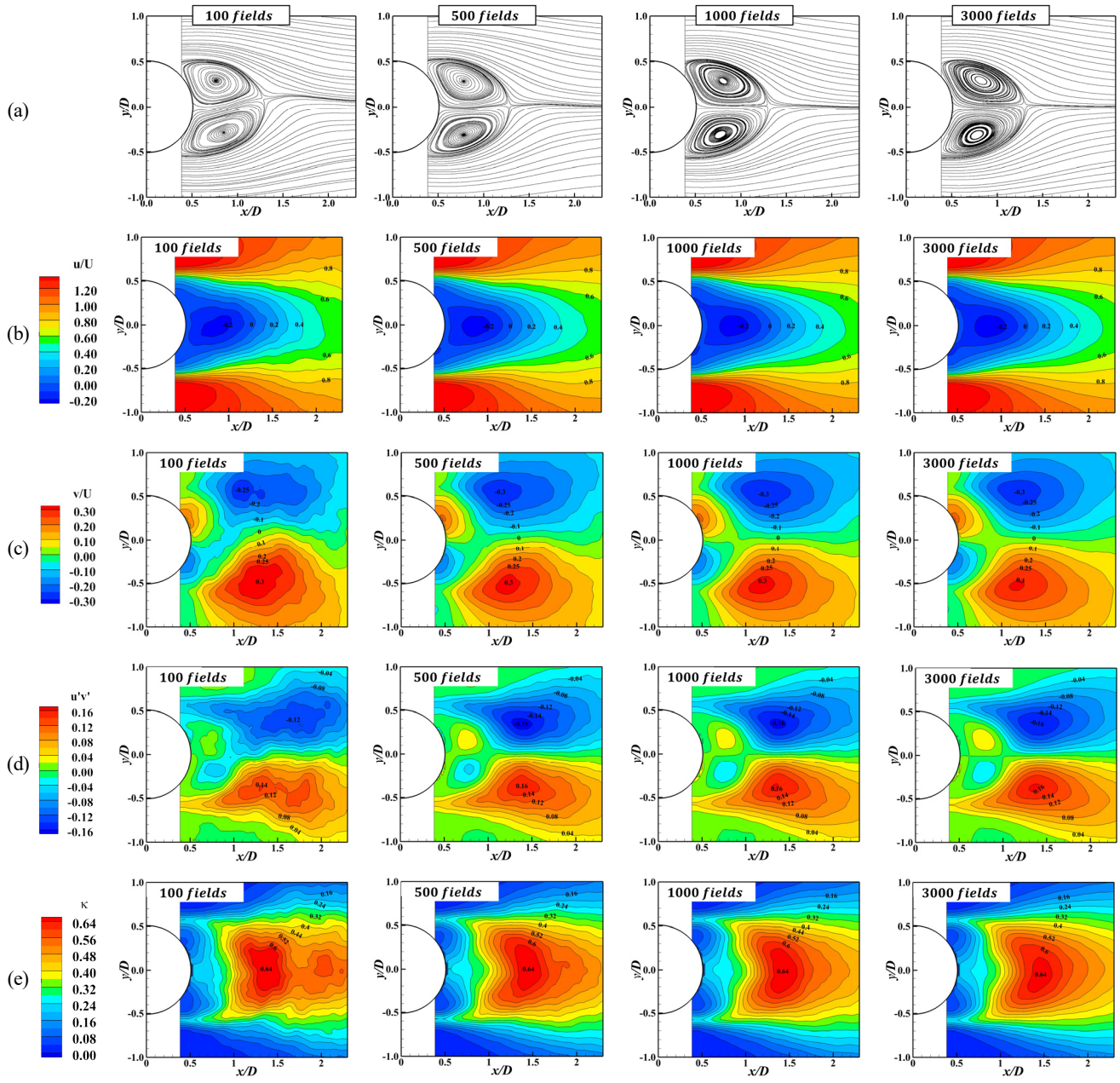

Fig. 6 Comparison of flow fields for different averaging fields: (a) mean streamlines, (b) mean streamwise velocity, (c) mean crosswise velocity, (d) $u'v'$ Reynolds shear stress, and (e) turbulent kinetic energy.

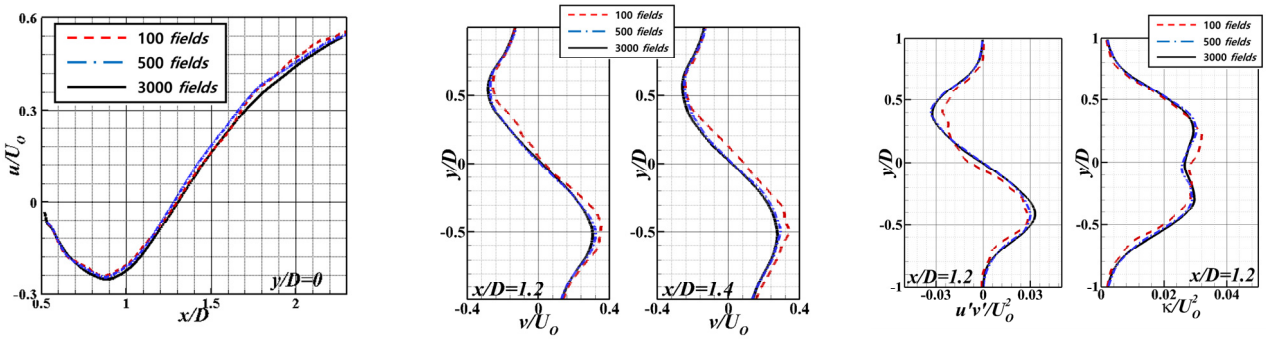

Fig. 7 Comparison of physical quantities for different averaging fields: (a) mean streamwise velocity, (b) mean crosswise velocity, (c) $u'v'$ Reynolds shear stress, and (d) turbulent kinetic energy.

turbulent kinetic energy were compared according to the number of samples as shown in in Fig. 6. When the number of samples is 100, the spatial distributions of all measured physical quantities are asymmetric and uneven with respect to $y/D = 0$, indicating that more samples are required to accurately estimate the mean flow fields. When the number of samples increases from 500 to 1,000, the spatial distributions improve. In particular, the results of the streamwise and crosswise velocity fields converge more rapidly than those of the Reynolds shear stress and turbulent kinetic energy. When the number of samples is 3,000 or larger, there is no difference in results depending on the number of samples for all physical quantities as shown in Fig. 6. For a quantitative comparison, each physical quantity was compared according to the change in y/D at $x = 1.2D$. The physical trends observed in Fig. 6 can be clearly confirmed in Fig. 7. In other words, as the number of samples increases, convergence is observed for 3,000 samples. The streamwise and crosswise velocity fields converge when the number of samples is at least 1,000, but the Reynolds stress and turbulent kinetic energy distributions, which are related to turbulent fluctuations, converge for 3,000 samples. Thus, the optimum number of samples to obtain mean flow fields is 3,000, which leads to consistent results.

To verify the experimental technique developed in this study, the results of this study were compared with the results of Braza et al. (2006). The experimental conditions of the two studies are listed in Table 2. The mean flow fields were acquired using approximately 4,600 and 3,000 instantaneous velocity vector fields in Braza et al. (2006) and the present study, respectively.

Table 2 Experimental conditions of the present study and Braza et al. (2006).

	Present study	Braza et al. (2006)
Type of tunnel	Water tunnel	Wind tunnel
Reynolds number	1.41×10^5	1.41×10^5
D (mm)	36	140
L (mm)	600	670
H (mm)	600	670
Turbulence intensity (%)	1.0	1.5
Blockage ratio (%)	6.0	20.8
Aspect ratio	16.7	4.8

Fig. 8(a) compares the mean streamline distributions. Based on $y/D = 0$, the upper and lower parts represent the results of Braza et al. (2006) and the present study, respectively. The results of the two studies are generally consistent for the size and geometry of the separation bubble. For a quantitative comparison, the recirculation length (l_C) is compared, and there is no significant difference ($1.28D \pm 0.03D$ in Braza et al. (2006) and $1.29D \pm 0.005D$ in the present study). Fig. 8(b) and Fig. 8(c) compare the streamwise and crosswise velocity distributions, respectively. When the periodic occurrence of the Kármán vortex street in the sub-critical regime is averaged over time, the commonly observed velocity distributions are identical in the results of the two studies. The negative and positive switching positions of the streamwise velocity caused by the separation bubble and the maximum value position of the vertical velocity ($x/D = 1.2$) also show good agreement. Fig. 8(d) and Fig. 8(e) show the $u'v'$ Reynolds shear stress distributions and turbulent kinetic energy. First, a slight difference in the y/D position is observed for the position at which the maximum Reynolds shear stress is caused by the release of the Kármán vortex street ($x/D = 1.4$ and $y/D = \pm 0.3$ in Braza et al. (2006) and $x/D = 1.388$ and $y/D = \pm 0.367$ in the present study). The measurements of the present study differ from those of Braza et al. (2006) by approximately 11%. The turbulent kinetic energy is maximum at $x/D = 1.25$ in Braza et al. (2006) and at $x/D = 1.41$ in the present study. The qualitative distributions of both physical quantities are in good agreement in the results of both studies, but there is a slight difference in the quantitative size compared to the mean velocity distribution. This appears to be due to the different turbulence intensities as well as difference in aspect ratio. Regarding previous studies on turbulence intensity, Blackburn and Melbourne (1996) observed the characteristics of the lift force acting on the cross section of a cylinder according to the turbulence intensity in the Reynolds number range of 1×10^5 to 5×10^5. They found that the standard deviation of the lift coefficient was dependent on the Reynolds number at the turbulence intensities of 0.6% and 4.2%, and increased as the turbulence intensity decreased. Cheung and Melbourne (1980) examined the characteristics of the drag coefficient when the

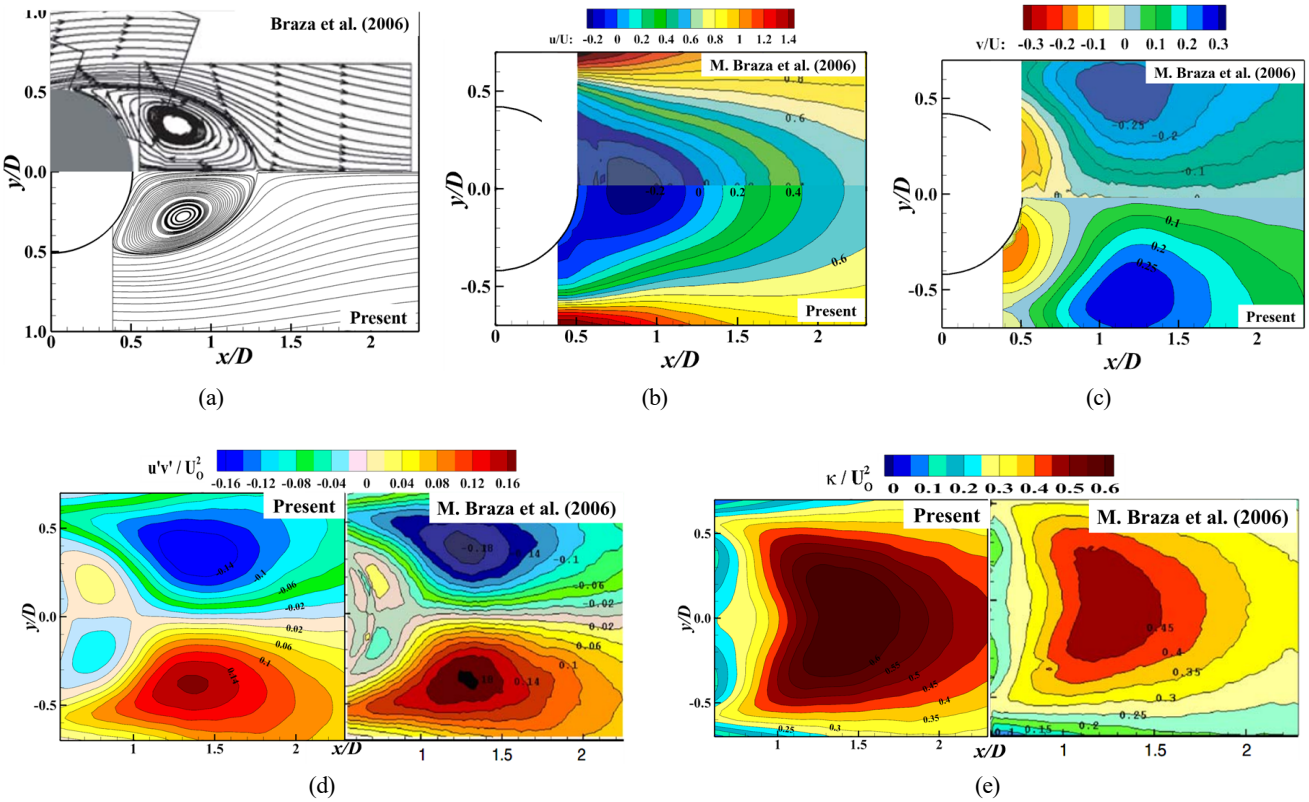

Fig. 8 Comparison of flow fields between the present study and Braza et al. (2006): (a) mean streamwise velocity, (b) mean crosswise velocity, (c) Reynolds shear stress, and (d) turbulent kinetic energy.

turbulence intensity varied from 0.4% to 9.1% for Reynolds number between 7×10^4 and 6×10^5. The drag coefficient decreased with increase in the turbulence intensity before the Reynolds number reached the critical regime. Regarding the effect of aspect ratio, Achenbach and Heinecke (1981) identified vortex shedding at an aspect ratio of 6.75, but not at 3.38. Blackburn and Melbourne (1996) reported that vortex shedding with a period did not occur when the aspect ratio was 4.5. To summarize, the aspect ratio and turbulence intensity affect the lift and drag coefficients, which are closely related to the characteristics of flow fields. Table 2 shows the experimental values of the blockage ratio and aspect ratio considered by Braza et al. (2006) and in the present study. A relatively low blockage ratio and high aspect ratio are considered in the present study. In addition, although the turbulence intensity considered in the present study is only 0.5% lower than that in Braza et al. (2006), the difference in tunnel environment and geometric conditions leads to a difference in the measurement results between the two studies. The test conditions of the present study are more favorable for observing flow around a cylinder than those of Braza et al. (2006).

4. Conclusions

Cylindrical geometry is common in marine structures, and hence, it is important to investigate the flow characteristics of full-scale cylinders. For full scale flow, it is important to utilize accurate flow visualization techniques to identify the flow characteristics up to the critical regime of high Reynolds numbers. Hence, in this study, we identified the basic characteristics of particle image velocimetry (PIV) and compared the results with those of previous studies. The visualization study of the flow past cylinder performed using the cavitation tunnel and PIV system of the Korea Research Institute of Ships & Ocean Engineering (KRISO). Due to the nature of PIV in which velocity vectors are calculated by acquiring particle images, the time interval of two particle images and the number of instantaneous flow fields are important parameters.

First, regarding the effect of the time interval, the pulse time of the laser was adjusted and a particle moving time of three to four pixels in two particle images was adopted because the flow velocity of particles is known to decrease in cylinder wakes. When the pulse time was long, vortices in the wake area could not be properly measured and the velocity vector size was exaggerated in the flow direction.

Next, we evaluated the effect of number of instantaneous flow fields on the measurement of mean velocities. To obtain more accurate results of mean flow fields, at least 1,000 instantaneous flow fields must be used to measure the mean velocities and at least 3,000 instantaneous flow fields are required to measure the Reynolds shear stress and turbulent kinetic energy distributions.

Consequently, it is necessary to select the pulse time of the laser according to the flow characteristics that correspond to experimental conditions, and good results can be achieved by adopting a pulse time that allows particles to have a distance of three to four pixels. It is also observed that turbulence properties have constant values when at least

3,000 instantaneous velocity fields are acquired and averaged.

Hence, based on the established PIV technique, satisfactory results are confirmed through a comparison with previous studies, but there are quantitative differences. This appears to be due to the difference in experimental environment, such as the tunnel shape, blockage ratio, and aspect ratio. Finally, the flow fields around a circular cylinder were analyzed according to the Reynolds number. Further research is required to observe changes in flow in the critical regime more closely.

Conflict of Interest

We declare no potential conflict of interests relevant to this article.

Funding

This work was supported by the Korea Research Institute of Ships & Ocean Engineering Project ("Development of CFD Technology for Global Performance Analysis of Offshore Structure") funded by the Ministry of Oceans and Fisheries (PES4780).

References

Achenbach, E., & Heinecke, E. (1981). On vortex shedding from smooth and rough cylinders in the range of Reynolds numbers 6×10^3 to 5×10^6. *Journal of Fluid Mechanics*, 109, 239–251. https://doi.org/10.1017/S002211208100102X

Blackburn, H. M., & Melbourne, W. H. (1996). The effect of free-stream turbulence on sectional lift forces on a circular cylinder. *Journal of Fluid Mechanics*, 306, 267–292. https://doi.org/10.1017/S0022112096001309

Blevins, R. D. (1977). *Flow-Induced Vibration*. Van Nostrand Reinhold Company.

Braza, M., Perrin, R., & Hoarau, Y. (2006). Turbulence properties in the cylinder wake at high Reynolds numbers. *Journal of Fluids and Structures, 22*(6–7), 757–771. https://doi.org/10.1016/j.jfluidstructs.2006.04.021

Chen, W., Wang, S., Shi, X., Rheem, C. K., Lin, Y., & Liu, E. (2022). Numerical simulation of surface roughness effects on the vortex-induced vibration of a circular cylinder at a subcritical Reynolds number. *International Journal of Naval Architecture and Ocean Engineering, 14*, 100430. https://doi.org/10.1016/j.ijnaoe.2021.100430

Cheung, C. K., & Melbourne, W.H. (1980). Wind tunnel blockage effect on a circular cylinder in turbulent flows. *In Proceedings of the 7th Australasian Hydraulics and Fluid Mechanics Conference, Brisbane, Australia,* 127–130. https://search.informit.org/doi/10.3316/informit.558932646045391

James, W. D., Paris, S. W., & Malcolm, G. N. (1980). Study of viscous crossflow effects on circular cylinders at high reynolds numbers. *AIAA paper, 18*(9), 1066. https://doi.org/10.2514/3.50855

Lee, S. J. (1999). *PIV velocity field measurement*. POSTECH, 11–231.

Lee, J. H., Paik, B. G., Kim, K. Y., Jung, J. H., Cho, S.K., & Sung, H. G. (2018). A study on visualization wake of circular cylinder wake using PIV method. *Proceedings of 2018 Fall Conference of The Korean Society of Visualization*, Pusan, Korea, 69-70.

Paik, B. G., Kim, K. Y., Cho, S. R., & Ahn, J. W. (2007). Study on quantitative visualization using bubble tracer in a cavitation tunnel. *Journal of the Korean Society of Visualization, 5*(1), 19–26.

Paik, B. G., Kim, K. Y., Kim, K. S., Lee, J. Y., & Lee, S.J. (2010). Analysis of the unstable propeller wake using POD method. *Journal of the Society of Naval Architects of Korea, 47*(1), 20–29. https://doi.org/10.3744/SNAK.2010.47.1.020

Park, G. S., & Kwak, Y. K. (2004). Flow survey around two-dimensional circular cylinder using PIV technique. *Journal of Ocean Engineering and Technology, 18*(3), 1–7.

Roshko, A. (1961). Experiments on the flow past a circular cylinder at very high Reynolds number. *Journal of Fluid Mechanics, 10*(3), 345–356. https://doi.org/10.1017/S0022112061000950

Schewe, G. (1983). On the force fluctuations acting on a circular cylinder in crossflow from subcritical up to transcritical Reynolds number. *Journal of Fluid Mechanics, 133*, 265–285. https://doi.org/10.1017/S0022112083001913

van Hinsberg, N. P. (2015). The Reynolds number dependency of the steady and unsteady loading on a slightly rough circular cylinder: From subcritical up to high transcritical flow state. *Journal of Fluids and Structures, 55*, 526–539. https://doi.org/10.1016/j.jfluidstructs.2015.04.002

van Hinsberg, N. P., Schewe, G., & Jacobs, M. (2018). Experimental investigation on the combined effects of surface roughness and corner radius for square cylinders at high Reynolds numbers up to 10^7. *Journal of Wind Engineering and Industrial Aerodynamics, 173*, 14–27. https://doi.org/10.1016/j.jweia.2017.12.003

Williamson, C. H. K. (1996). Vortex dynamics in the cylinder wake. *Annual Review of Fluid Mechanics, 28*, 477–539.

Zdravkovich, M. M. (1997). *Flow around circular cylinders. Volume I: Fundamentals*. Oxford Science Publications.

Author ORCIDs

Author name	ORCID
Lee, Jun-Hee	0000-0002-0618-3739
Paik, Bu-Geun	0000-0002-1311-4854
Cho, Seok-Kyu	0000-0002-7821-4848
Jung, Jae-Hwan	0000-0001-9384-5720

KSOE

Journal of Ocean Engineering and Technology 37(4), 145-157, August, 2023
https://doi.org/10.26748/KSOE.2023.018

pISSN 1225-0767
eISSN 2287-6715

Original Research Article

Validation of OpenDrift-Based Drifter Trajectory Prediction Technique for Maritime Search and Rescue

Ji-Chang Kim[1,2], Dae Hun Yu[1], Jung-eun Sim[1], Young-Tae Son[3], Ki-Young Bang[3] and Sungwon Shin[4]

[1]*Engineer, Geosystem Research Corporation, Gunpo, Korea*
[2]*Master Course, Department of Marine Science and Convergent Technology, Hanyang University ERICA, Ansan, Korea*
[3]*Principal Engineer, Geosystem Research Corporation, Gunpo, Korea*
[4]*Professor, Department of Marine Science and Convergent Technology, Hanyang University ERICA, Ansan, Korea*

KEYWORDS: Maritime distress, Search and Rescue, Drifter, Leeway, OpenDrift

ABSTRACT: *Due to a recent increase in maritime activities in South Korea, the frequency of maritime distress is escalating and poses a significant threat to lives and property. The aim of this study was to validate a drift trajectory prediction technique to help mitigate the damages caused by maritime distress incidents. In this study, OpenDrift was verified using satellite drifter data from the Korea Hydrographic and Oceanographic Agency. OpenDrift is a Monte-Carlo-based Lagrangian trajectory modeling framework that allows for considering leeway, an important factor in predicting the movement of floating marine objects. The simulation results showed no significant differences in the performance of drift trajectory prediction when considering leeway using four evaluation methods (normalized cumulative Lagrangian separation, root mean squared error, mean absolute error, and Euclidean distance). However, leeway improved the performance in an analysis of location prediction conformance for maritime search and rescue operations. Therefore, the findings of this study suggest that it is important to consider leeway in drift trajectory prediction for effective maritime search and rescue operations. The results could help with future research on drift trajectory prediction of various floating objects, including marine debris, satellite drifters, and sea ice.*

1. Introduction

Marine leisure activities have recently increased, resulting in an increase in maritime distress, which poses a threat to lives and property. The Korea Coast Guard (KCG) provides statistics on accidents that occur in different maritime police jurisdictions. From 2017 to 2021, maritime distress accidents in South Korea have been continuously increasing, and in about 31% of maritime accidents, it has been difficult to locate missing people. Accidents caused by a loss of vessel power, capsizing, sinking, and grounding account for about 28.3% of all accidents, while about 29.5% are caused by flooding, fire, and collision, which have various possibilities depending on the response after the accident. About 67.5% of all accidents occur in good weather conditions, and the remaining 32.5% occur in poor weather conditions such as storm warnings, rough weather, and low visibility. Fishing vessels accounted for the majority of vessel types and were involved in 78.9% of all accidents (KCG, 2022b).

According to Article 2 of the "Act on the Search and Rescue in Waters", maritime distress is defined as situations where human life, physical safety, or the safety of vessels are at risk on the water. Vessels, lifeboats, people, and other objects involved in maritime distress tend to drift due to various external forces such as wind, tidal currents, ocean currents, and waves. As time passes, they move increasingly further away from the point of an accident. This characteristic leads to a high mortality rate and makes search and rescue (SAR) operations difficult, incurring significant costs. Therefore, in order to reduce casualties in events of maritime distress, it is important to quickly and accurately estimate the location of distressed objects and determine the search area (Kang, 1998).

To estimate the location of drifting objects, the total vector is calculated while considering various oceanic external forces from the starting point of the distress occurrence or the last reported accident location, which allows for an estimation of the hourly position of drifting objects (Yun et al., 2001). The initial location and time of the

Received 14 June 2023, revised 19 June 2023, accepted 27 June 2023
Corresponding author Sungwon Shin: +82-31-400-5533, sungwshin@hanyang.ac.kr

occurrence of maritime distress depend on reports from individuals or entities involved in the accident or surrounding vessels, so they contain some margin of error. Depending on the navigational device used for the initial position measurement, the error may range from meters to hundreds of meters, and the time of distress may vary from minutes to several hours (Lee et al., 1999). According to Tipton et al. (2022), the major factors determining the survival rate of individuals immersed in water include water temperature, accident area, age of the survivor, clothing, and whether a life jacket was worn. Generally, the survival rate remains relatively high at around 80% for about 4–5 h after the onset of drifting. However, survival rates drastically drop to about 40% after this period, and by 14 h, the survival rate reaches 0%.

In South Korea, a law was enacted in 1961 for the handling of rescue operations involving distressed vessels and individuals and the preservation of life and property. Legal amendments were made in 1994 and 1996 to facilitate South Korea's accession to and compliance with the International SAR Convention. In 2012, the law was revised to reflect changes due to the increase in marine leisure. The law was renamed the "Act on the Search and Rescue in Waters," which stipulates the authority of the chief of rescue and the duty of the captain and crew of distressed vessels to participate in rescue operations. In 2021, an amendment was made to promote the participation of private maritime rescue team members. Now, the act is the law that protects the lives and property of citizens in the event of maritime distress and supports private maritime rescue activities (KCG, 2022a).

The Korea Hydrographic and Oceanographic Agency (KHOA) has established and operates an ocean current prediction system to provide consistent support for SAR operations by relevant agencies in the event of maritime distress. The KHOA is improving techniques to predict drift trajectories for maritime SAR activities by conducting drift prediction experiments using satellite drifters to improve accuracy (KHOA, 2022). Previous research predicted the trajectory of satellite drifters using machine learning and the features of ocean currents and wind, such as their strength and direction (Lee et al., 2017; Kim and Kim., 2018; Seo, 2021; Ha et al., 2022). Lee et al. (2017) used machine learning techniques to improve the "Modelo Hidrodinamico" (MOHID) numerical model and develop a model for predicting the trajectories of satellite drifters. Kim and Kim (2018) proposed a data correction model using recurrent neural networks and autoencoders to address possible errors or missing data observed using satellite drifters. Seo (2021) conducted a study on a new feature generation method for predicting the trajectories of satellite drifters using the support vector machine (SVM), k-nearest neighbor (k-NN), and random forest methods based on observational data from satellite drifters. Ha et al. (2022) compared and analyzed a particle-tracking model based on a numerical ocean model with a model based on observation data.

According to the International Maritime Organization (IMO), SAR refers to the operations conducted using aircraft, vessels, submarines, and special equipment to find distressed persons. The IMO adopted the International Convention on Maritime SAR in 1979, establishing an international SAR system. There are over 80 SAR Convention countries, including the United States, Japan, China, Russia, and Korea, and these countries have a duty to establish SAR organizations and support the SAR operations of neighboring countries when necessary (Park et al., 1989).

In 1999, the IMO and the International Civil Aviation Organization (ICAO) jointly developed the International Aeronautical and Maritime SAR manual (IAMSAR) for use as national SAR guidelines in all SAR Convention signatory countries. The IAMSAR manual reflects the reality of maritime distress, which is highly uncertain, and supports the decision-making of SAR personnel. However, given the nature of the manual, all data must be manually entered to derive results, which makes rapid response difficult in the event of maritime distress. As a result, leading maritime nations like the United States and Canada are investing heavily in field experiments for distressed objects and the development of ocean current measurement buoys to accurately track the location of distressed vessels (Yun, 2005). They have also developed and are operating SAR planning programs like the SAR optimal planning system (SAROPS) and SARMAP (Fig. 1).

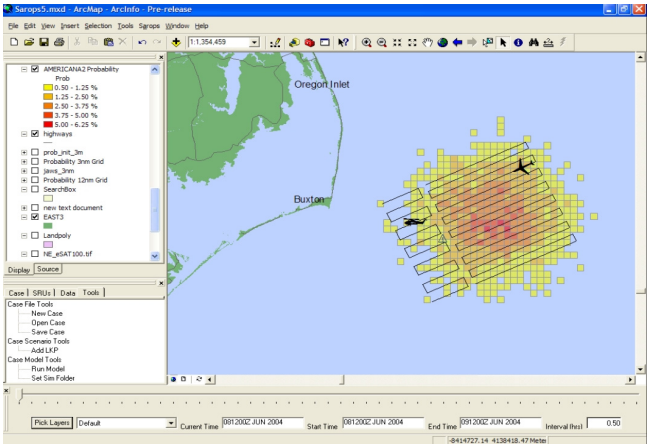

(a)

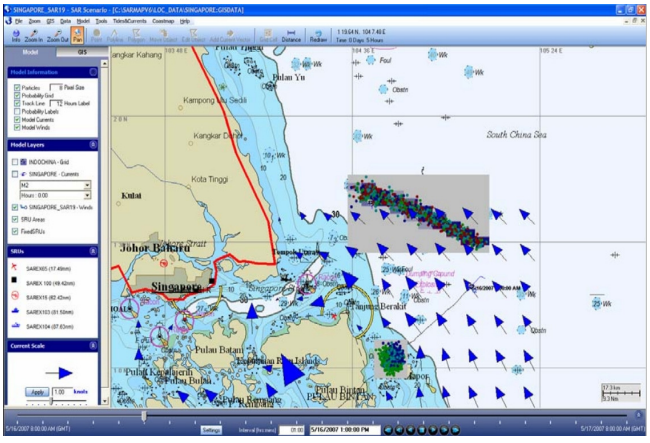

(b)

Fig. 1 Search and rescue plan generation program operated internationally: (a) SAROPS (U.S. Coast Guard); (b) SARMAP (RPS Group)

Leading maritime nations have implemented an integrated system that incorporates the prediction of a drifter's locations to calculate the probability of containment (POC), probability of detection (POD), and ultimately the probability of success (POS), which are utilized in search planning. In South Korea, the KCG is the agency responsible for maritime SAR and utilizes the Ocean Current Prediction System developed by the KHOA for estimating the locations of drifters. The ocean current prediction system analyzes marine meteorological data such as ocean currents and winds to predict the trajectory of drifters and track the trajectories of vessels or missing individuals. Currently, there is no equivalent search evaluation system to that in other countries (Yun, 2020).

According to Breivik and Allen (2008), there is a need for probabilistic representation to calculate the uncertain movement of drifting maritime objects. Instead of predicting the exact trajectory of the object, they found the area where the drifting object is most likely to be located by altering various parameters that influence the movement of the object using the Monte Carlo technique and calculating a search area. Given that South Korea has a complex coastline and significant differences in the local characteristics of the ocean, continued efforts are being made to develop high-resolution numerical models and carry out various verifications to simulate ocean currents accurately. However, due to the high degree of uncertainty in the movement of maritime drifting objects, it is essential to consider unpredictable factors related to environmental forces in predictions. But most studies conducted in South Korea have been limited to evaluating the accuracy of models by analyzing the performance of ocean numerical models and machine learning-based prediction of maritime drifting object trajectories, making it difficult to consider the uncertain factors in the marine environment. Furthermore, although there have been field studies to derive the leeway parameters, there have not been many experiments on predicting the probabilistic trajectory of drifting objects using them.

Therefore, in this study, simulations were performed using OpenDrift, which allows Monte-Carlo-based random particle trajectory predictions to consider uncertain factors in drift movement represented by leeway. The aim of this study was to confirm the performance of OpenDrift simulations through an evaluation method proposed in previous research. An analysis method and prediction results are presented for evaluating the applicability to maritime SAR to help reduce the damage from maritime distress.

2. Drifter Trajectory Prediction

2.1 Leeway

Among the external forces acting on maritime objects, the ocean current and wind are considered the most significant. Leeway refers to the amount of movement of a drifting object caused by the wind acting on the exposed surface of the drifter and is typically calculated using information observed from maritime drifter experiments regarding ocean current, wind, and drifter location (Yun et al., 2001). The way of expressing the leeway formula varies slightly depending on the researcher. Notably, early research such as that by Hufford and Broida (1974) represented leeway as the leeway speed and divergence angle, while Allen and Plourde (1999) represented leeway as a downwind leeway component (DWL), a component parallel to the wind, and a crosswind leeway component (CWL) that is perpendicular to the wind. CWL is a positive (+) value when the direction of the leeway is to the right and a negative (-) value when it is to the left (Fig. 2).

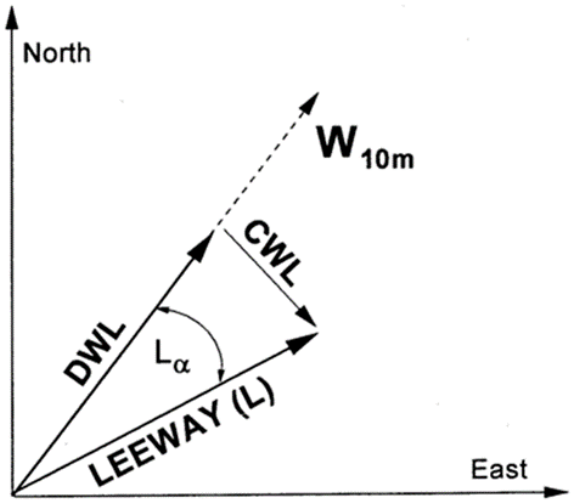

$\boldsymbol{W_{10m}}$ = Wind velocity vector adjusted to 10 m height

$\boldsymbol{L}$ = Leeway vector

$\boldsymbol{L\alpha}$ = Leeway angle

$\frac{|\boldsymbol{L}|}{|\boldsymbol{W_{10m}}|}$ = Leeway rate

$\boldsymbol{DWL} = |L|\sin(90° - L\alpha)$ = Downwind Leeway component

$\boldsymbol{CWL} = |L|\cos(90° - L\alpha)$ = Crosswind Leeway component

Fig. 2 Relationship between the leeway speed, downwind, and crosswind components of leeway (Allen and Plourde, 1999)

Several SAR models have been developed internationally to reflect the effects of leeway (Fig. 3). The geographic display operations computer automated manual method (GDOC AMM) is a computerized program that uses the method in the national SAR manual (NATSAR) issued by the United States Coast Guard (USCG). It always applies 100% ocean surface current when calculating drift distance and determines the search area based on leeway speed and divergence angle. The computer-aided search planning (CASP) model assumes that basic variables such as time, location, current, and wind have a probability distribution through Monte Carlo simulation. It applies an uncertainty coefficient of 0.33 to the leeway rate to repeatedly calculate the drift location. The AP98 model developed by Allen and Plourde uses the slope and y-intercept of the leeway equation. The location of a drifting object is probabilistically calculated by randomly altering the slope and y-intercept, assuming a normal distribution with a standard deviation of $S_{y/x}$ (Allen and Plourde, 1999).

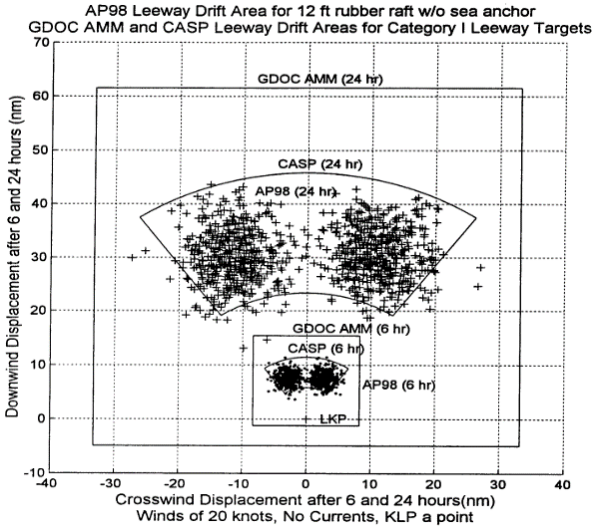

Fig. 3 The leeway drift area of a leeway distribution model (Allen and Plourde, 1999)

2.2 Drifter

The KHOA is conducting experiments using satellite-tracked drifters to improve the accuracy of ocean current predictions. They provide data through the "Badanuri Marine Information Service." Since 2016, the surface velocity program (SVP) has been providing data, and since 2019, data from SVP and surface satellite-tracked drifters have been available. The SVP uses a drogue installed below a buoy with a diameter of less than 40 cm (Fig. 4), while the surface satellite-tracked drifters are small cylindrical buoys with a diameter of 10 cm and a length of 30 cm.

The leeway effect caused by wind is important in predicting the movement of maritime drifters. However, the surface satellite-tracked drifters are not suitable for considering the leeway effect due to their small exposed area on the water surface. The SVP is an international research program that is widely used in oceanography, climatology, weather forecasting, and other marine-related research fields. It focuses on measuring speeds at the ocean surface and significantly

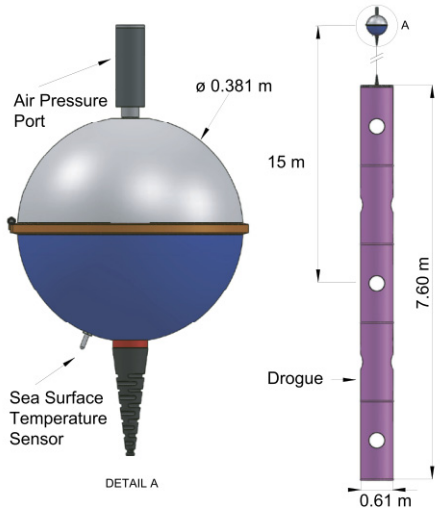

Fig. 4 Specifications of KHOA SVP (Centurioni et al., 2017)

Table 1 Leeway coefficients of buoy C (Cho et al., 2014)

Components	*Slope* (% wind)	$S_{y/x}$ (cm/s)
DWL	2.23	3.0
CWL (Left)	-0.91	1.9
CWL (Right)	0.91	2.1

contributes to enhancing understanding of various marine environmental variables such as ocean circulation, sea surface temperature, and wind patterns (Lumpkin and Pazos, 2007). In this study, data from the KHOA SVP were used to consider the leeway effect on satellite-tracked drifters.

Cho et al. (2014) conducted field experiments on buoy C, which is a cylindrical buoy with a diameter of 50 cm and a height of 30 cm and has a drogue installed. Their leeway parameters for buoy C are provided in Table 1. Buoy C is similar to the KHOA SVP, and in this study, the values from buoy C were used as the leeway parameters for the drifters. Experiments were conducted using the location data of an SVP satellite-tracked drifter (ID: 300434063234840), which was deployed in the Jeju Strait in July 2019. The data were acquired from the KHOA's Badanuri Marine Information Service.

2.3 OpenDrift

OpenDrift is a software package developed by the Norwegian Meteorological Institute (NMI) for simulating the trajectories and endpoints of maritime drifters. It is implemented as a Python-based open-source framework for Lagrangian particle modeling. OpenDrift is designed to be fast and easy to use and supports various operating systems such as Linux, Mac, and Windows. It offers the advantage of providing different libraries, allowing researchers to choose modules that suit their specific purposes. While the detailed workflow may vary depending on the selected modules, the general process follows the framework illustrated in Fig. 5.

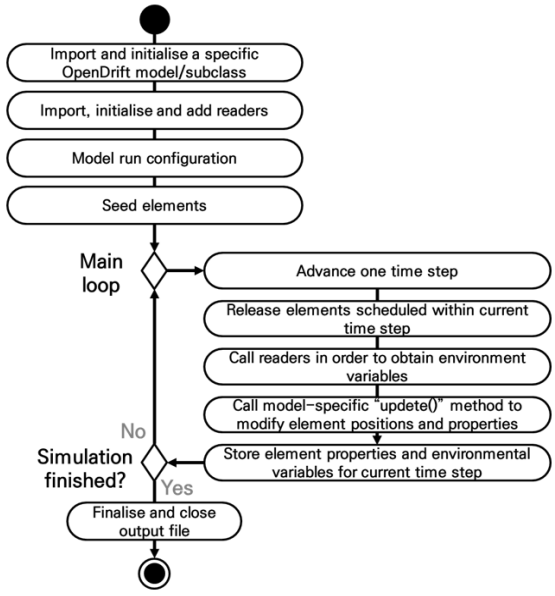

Fig. 5 Flowchart of an OpenDrift simulation (Dagestad et al., 2018)

OpenDrift's key components are the reader and basemodel classes in the module execution. The reader class reads external forcing data such as wind, wave, and ocean current data from numerical model data following the climate and forecast (CF) naming convention. It inputs the time series values of each grid into the OpenDrift module. The basemodel class provides common functionalities that are applicable to all drift prediction models for calculating the new positions of each particle based on the module execution (Dagestad et al., 2018).

Among the libraries in OpenDrift, the oceandrift module is the most basic module for predicting particle movement based on numerical models of ocean currents. Factors affecting particle movement include advection, wind drag, Stokes drift, turbulent mixing, vertical advection, and machine learning. The module allows for consideration of horizontal diffusion and the influence of wind speed through the wind drift factor. The leeway module predicts particle movement based on numerical models of ocean currents and winds. It incorporates leeway parameters using the AP98 model representation, as specified by Allen and Plourde (1999) and Breivik and Allen (2008), and there are 85 types of drifters in total. The leeway parameters are internally embedded and are used when calculating the linear regression relationship between leeway speed and wind speed using the least square method. The calculations are done using Eqs. (1)–(3).

$$W_{10} = \sqrt{U_{wind}^2 + V_{wind}^2} \tag{1}$$

$$a_n = Slope + \frac{\epsilon_n}{20},\ b_n = Offset + \frac{\epsilon_n}{2} \tag{2}$$

$$L = a_n \times W_{10} + b_n \tag{3}$$

In these equations, U_{wind} and V_{wind} represent the magnitude of the x-direction and y-direction winds from the input numerical model data. *Slope* and *Offset* refer to the slope and y-intercept of the leeway equation, respectively. ϵ_n is a value obtained by applying a random number from a normal distribution to the leeway's standard deviation, while a_n and b_n are values that reflect randomness in the *Slope* and *Offset*. Each particle in OpenDrift is determined to move to the next location based on the vector sum of the calculated ocean current and leeway (Dagestad et al., 2018).

2.4 Simulation Setup

To run OpenDrift, numerical model data for oceanic forcing are required. The oceandrift module requires numerical models of ocean currents, while the leeway module requires numerical models of both ocean currents and winds. In this study, the hybrid coordinate ocean model (HYCOM) and korea local analysis and prediction system (KLAPS) were used for numerical model data for oceanic forcing. Detailed information about the numerical models is provided in Table 2.

Table 2 Numerical model information used as input data for OpenDrift

Category	HYCOM	KLAPS
Variable value	Sea water velocity	Wind velocity
Grid size	1/12 degree	5 km
Time interval	1 h	1 h
Reference	HYCOM consortium	KMA

In a previous study, simulations were performed to evaluate the performance of trajectory prediction using forecast data (Liu and Weisberg, 2011). In these simulations, initial locations were released at regular time intervals along the drifter trajectories. The findings confirmed that the release interval time had minimal impact on the skill score. Additionally, if the simulation time is too short, the cumulative distance of the observations can be small, leading to increased uncertainty. Therefore, the simulation time was set to 72 h.

Based on the study by Liu and Weisberg (2011), particles were released at regular intervals along drifter trajectories to perform simulations. However, compared to the previous study, the simulation period in this research was very short, ranging from July 25, 2019, 0:00, to July 28, 2019, 23:00 (KST). If the release interval time for initializing the locations is set too long, the experiment data would be limited, making it difficult to ensure statistical reliability. Therefore, before conducting the experiments, a preliminary experiment was carried out by gradually increasing the interval for initializing the locations from 1 hour to 24 h with intervals of 1 h.

The aim of the preliminary experiment was to examine whether there would be significant changes in the skill score with different intervals for initializing the locations. The results of the preliminary experiment showed that even with a release interval time shorter than 24 h, there were no significant changes in the skill score (Fig. 6). Based on these preliminary results, the interval for releasing the initial locations was set to 1 hour to enhance the statistical reliability of the simulation results, resulting in a total of 96 cases of simulation data.

To understand the impact of the leeway on the trajectory prediction results, both the leeway module and the oceandrift module were applied under the same conditions. The particle stranding option was set to "off" in both the leeway module and the oceandrift module,

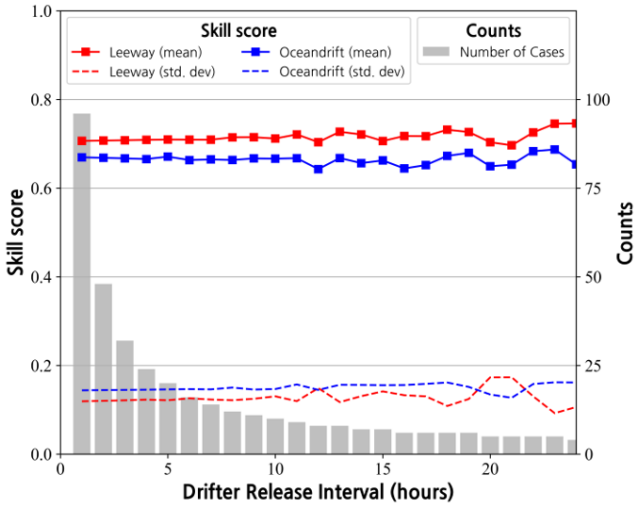

Fig. 6 Sensitivity of the skill scores to the drifter release interval

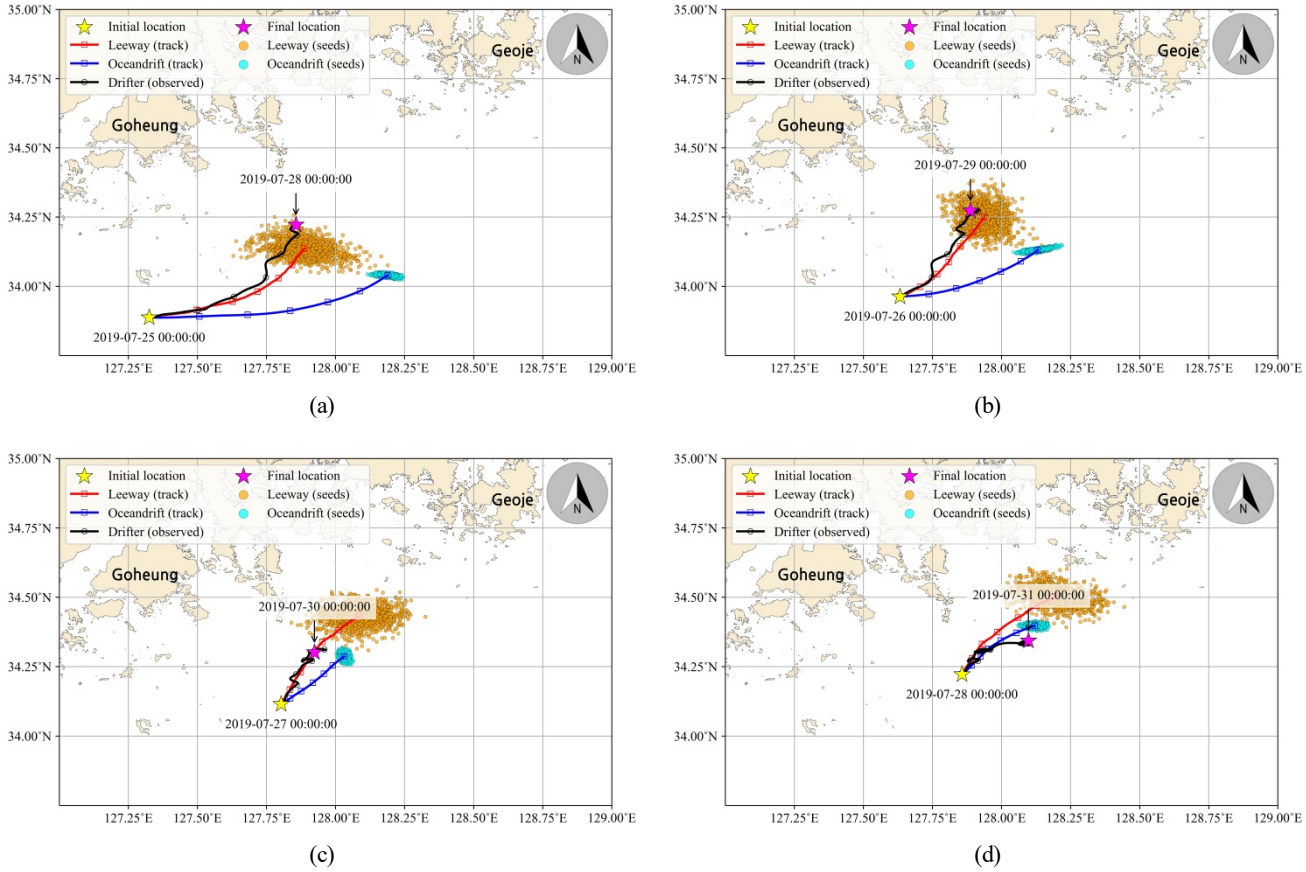

Fig. 7 Simulation results of OpenDrift during 72 h. The black solid line represents a satellite drifter (observed). The blue solid line represents the oceandrift module's results showing the average particle location at each time step. The red solid line represents the leeway module's results showing the average particle location at each time step. The light blue circle represents the particle distribution after 72 h of oceandrift module operation. The orange circle represents the particle distribution after 72 h of leeway module execution. Simulation results of OpenDrift at 0 h KST on (a) July 25th, (b) July 26th, (c) July 27th, and (d) July 28th.

while the remaining parameters such as the wind drift factor and current drift factor were set to their default values. Based on previous studies, each simulation was set to run for 72 h. In order to obtain statistically significant results, 1000 particles were randomly seeded within a 1-km radius, which followed a normal distribution (Fig. 7).

3. Validation of Simulation Results

3.1 Comparison Method of Predicted Drifter Trajectories

To validate the drifters trajectory prediction performance of OpenDrift, various evaluation methods were applied: the normalized cumulative Lagrangian separation (NCLS) evaluation proposed by Liu and Weisberg (2011), the root mean squared error (RMSE) evaluation considered by Dominicis et al. (2013), and the mean absolute error (MAE) and Euclidean distance (Euclid) evaluations used by Nam and Kim (2018). The NCLS calculates the separation distance based on the difference between observations and numerical solutions, and a skill score close to 1 indicates a perfect simulation (Fig. 8). The RMSE quantitatively represents the difference between observations and numerical solutions, and the larger the deviations, the higher the values

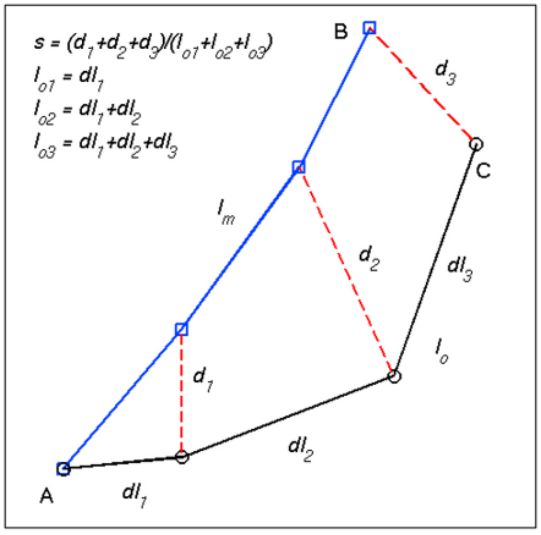

Fig. 8 A diagram illustrating the calculation method of NCLS (Liu and Weisberg, 2011)

of the RMSE are. While it provides a numerical representation of the errors, it is challenging to interpret the extent of the errors (Kim and

Yoon, 2011). The MAE represents the mean error value quantitatively, and the Euclidean distance represents the average distance between particles. Lower values in both evaluations indicate better prediction performance (Nam and Kim, 2018).

$$s = \sum_{i=1}^{N} d_i \,/\, \sum_{i=1}^{N} l_{oi} \tag{4}$$

$$NCLS(ss) = \begin{cases} 1 - \frac{s}{n} & (s \le n) \\ 0 & (s > n) \end{cases} \tag{5}$$

In Eqs. (4)–(5), d_i represents the separation distance between observations and the simulation result, l_{oi} represents the cumulative sum of the observed displacement distances, and N represents the total number of data points. s denotes the normalized cumulative separation, and n is a dimensionless value representing the allowed threshold. A smaller value of n indicates a stricter criterion for the simulation. In this study, a value of n = 1 was adopted, which was used by Nam and Kim (2018) and Ha et al. (2022).

$$RMSE = \sqrt{\frac{\Sigma_{i=1}^{N} (S_i, O_i)^2}{N}} \tag{6}$$

In Eq. (6), d represents the separation distance between the i-th model position (S_i) and the i-th observed position (O_i), while N denotes the total number of observations.

$$MAE = \frac{1}{N} \sum_{i=1}^{N} (|Lat(M)_i - Lat(O)_i| + |Lon(M)_i - Lon(O)_i| \tag{7}$$

$$Euclid = \frac{1}{N} \sum_{i=1}^{N} \left(\sqrt{(Lat(M)_i - Lat(O)_i)^2 + (Lon(M)_i - Lon(O)_i)^2} \right) \tag{8}$$

In Eqs. (7)–(8), *Lat(M)* and *Lon(M)* represent the latitude and longitude of the predicted model, respectively, while *Lat(O)* and *Lon(O)* represent the latitude and longitude of the observations. N represents the total number of observations.

3.2 Method for Evaluating Applicability in Maritime SAR

SAROPS, SARMAP, and other SAR support programs utilize random particle-based Monte Carlo simulations to account for the uncertainties in drifter movement. Based on the simulation results, search areas are established. Therefore, for an accurate simulation, it is necessary for the actual drifters to be located within the predicted area. To assess the effectiveness of the OpenDrift results for maritime SAR operations, the presence or absence of actual drifters within the predicted area was determined at each specific time. This concept is defined as location prediction conformance (LPC) in this study.

$$C = \begin{cases} 1 & (Include) \\ 0 & (Exclude) \end{cases} \tag{9}$$

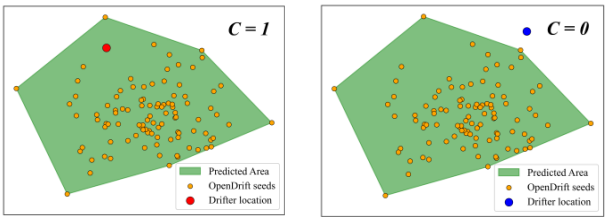

(a) (b)

Fig. 9 Method for determining the presence of observed drifters within a predicted model area. (a) Satellite drifter included within the prediction area (red circle) and (b) Satellite drifter not included within the prediction area (blue circle)

$$LPC(\%) = \frac{100}{N} \sum_{i=1}^{N} (C_i) \tag{10}$$

In Eq. (9), C represents whether an actual drifter is included within the predicted area. Its value is 1 if the drifter is within the area, as shown in Fig. 9(a), while it is 0 if the drifter is outside the area, as in Fig. 9(b). N in Eq. (10) is the total number of data and represents the probability of the drifter's location over the entire period, which is assessed by determining the presence at each time from the simulation results. The criterion for the predicted area is based on representing the Monte-Carlo-based simulation results of Breivik and Allen (2008) as polygonal areas (convex hulls) and it is set as a polygonal area connecting the outermost area of the particles simulated by OpenDrift.

4. Analysis Results

4.1 Assessment of Predictive Performance Over Simulation Elapsed Time

The results of the performance analysis with different simulation durations are shown in Fig. 10. The RMSE, MAE, and Euclid scores tended to increase as the simulation time elapsed, while the NCLS score tended to decrease. Lower RMSE, MAE, and Euclid values and higher NCLS values indicate higher prediction accuracy, which means that the overall prediction accuracy decreases with the passage of simulation time (Fig. 10). However, NCLS showed a sharp decrease for both leeway and oceandrift modules at up to 3 h into the simulation and showed a slight increase after 5–6 h of simulation (Table 3). The reason for the lowest skill score occurring at 5–6 h is thought to be the increased uncertainty of the drifter movement distance when the simulation's elapsed time was too short, as suggested in previous research (Liu and Weisberg, 2011). The calculated results after 72 h of simulation for each evaluation method are presented in Table 4.

In summary, the leeway module results showed better average predictive performance than the oceandrift module results. However, when considering the error range, there was no significant difference. This suggests that it can be difficult to evaluate the performance of the leeway module using conventional methods of assessing prediction accuracy.

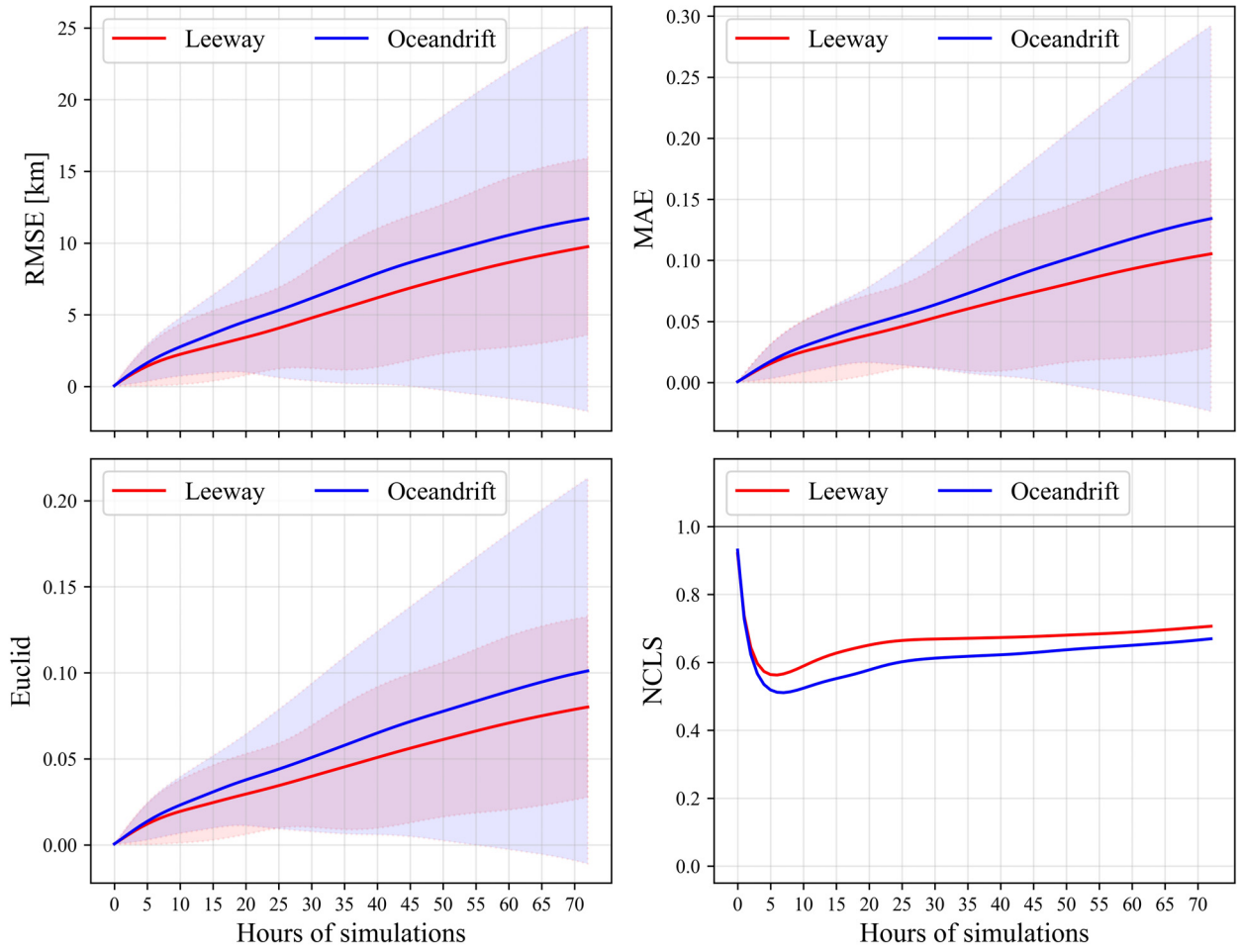

Fig. 10 Analysis results of RMSE, MAE, Euclid, and NCLS Skill scores based on the elapsed time of the simulation. The solid lines represent the skill scores for leeway (red) and oceandrift (blue), while the shaded areas indicate their respective 95% confidence intervals.

Table 3 NCLS skill scores based on the simulated elapsed time

Time (h)	Modules			
	Leeway		Oceandrift	
	mean	std. dev.	mean	std. dev.
1	0.7272	0.2060	0.7289	0.1545
2	0.6446	0.2711	0.6238	0.2064
3	0.5969	0.3004	0.5667	0.2281
4	0.5735	0.3152	0.5352	0.2370
5	0.5641	0.3220	0.5191	0.2392
6	0.5628	0.3237	0.5120	0.2376
7	0.5662	0.3217	0.5109	0.2339
8	0.5724	0.3169	0.5134	0.2283
9	0.5803	0.3098	0.5181	0.2213
10	0.5891	0.3009	0.5240	0.2128
...				
72	0.7065	0.1191	0.6696	0.1440
Mean	0.6648	0.1842	0.6149	0.1447

Table 4 Results of skill score analysis

Skills	Modules			
	Leeway		Oceandrift	
	mean	std. dev.	mean	std. dev.
NCLS	0.7065	0.1191	0.6696	0.1440
MAE	0.1053	0.0392	0.1342	0.0806
Euclid	0.0801	0.0268	0.1011	0.0572
RMSE (km)	9.7456	3.1448	11.7062	6.8630

* Results after 72 h of model execution

4.2 Analysis of NCLS by Simulated Initial Locations

The results of the NCLS analysis according to the elapsed simulation time (24, 48, and 72 h) for each simulated initial location showed a tendency for increased separation distance (d) between the prediction results and the observations as the simulation time elapsed. The mean value of d was calculated as 6.04 km for the leeway module and 7.81 km for the oceandrift module after 24 h. After 48 h, it was 11.36 km for the leeway module and 13.65 km for the oceandrift module, and after 72 h, it was 13.68 km for the leeway module and 15.80 km for the oceandrift module (Fig. 11(a)). The average

cumulative trajectory length (l_o) of the drifter was 20.74 km after 24 h, 38.94 km after 48 h, and 57.52 km after 72 h (Fig. 11(b)). The average cumulative trajectory length (l_m) of the OpenDrift simulation results was 17.10 km for the leeway module and 15.09 km for the oceandrift module after 24 h, 32.64 km for the leeway module and 25.06 km for the oceandrift module after 48 h, and 46.64 km for the leeway module and 42.46 km for the oceandrift module after 72 h (Fig. 11(c)).

The results of the NCLS analysis based on the start time of the

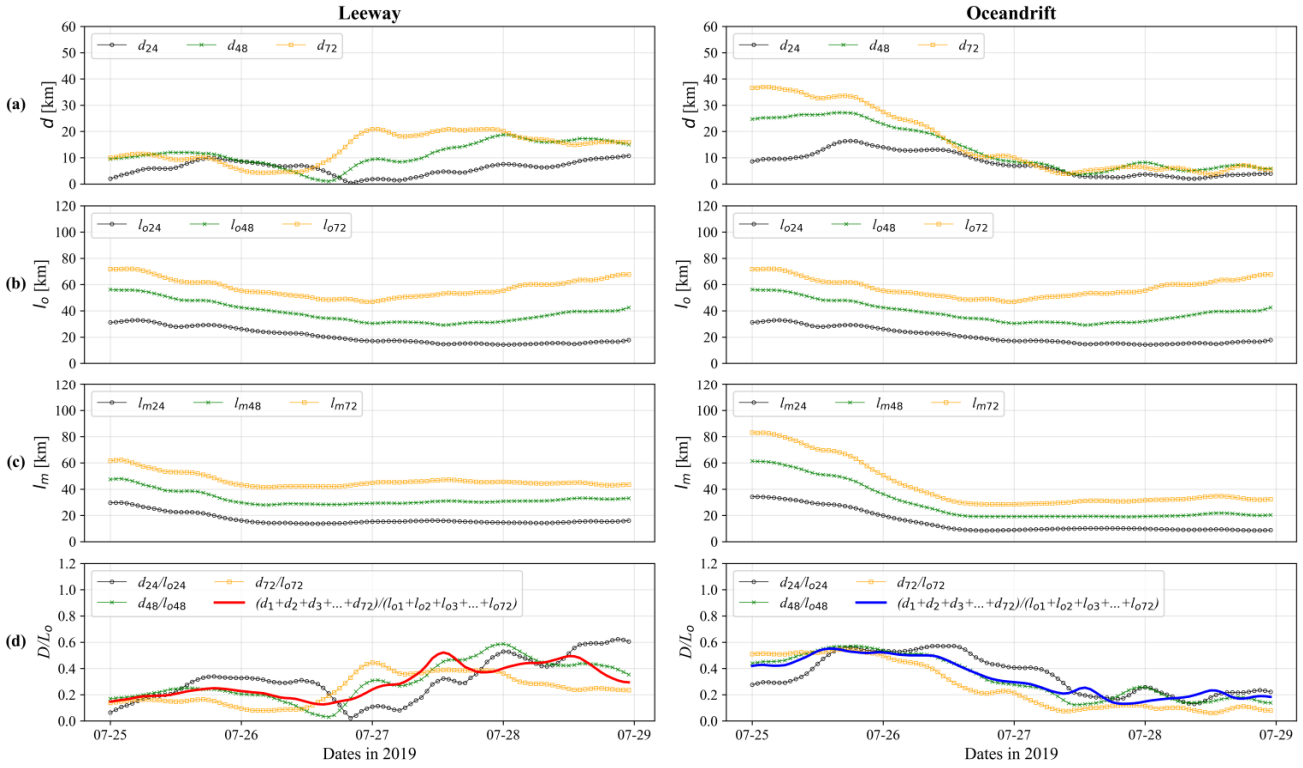

Fig. 11 Results of the NCLS analysis using OpenDrift. The left panel displays the analysis results from the leeway module, while the right panel shows those from the oceandrift module. The x-axis signifies the start time of the simulation. The black solid lines represent the calculated position 24 h after the start of the simulation, the green solid lines indicate the position 48 h after the start of the simulation, and the yellow solid lines show the position 72 h after the start of the simulation: (a) Distance discrepancy between the model and observations at each simulated time point; (b) Cumulative sum of the drifter's travel distance (observation); (c) Accumulated total travel distance for each respective module; (d) Result of s calculation based on Eq. (4).

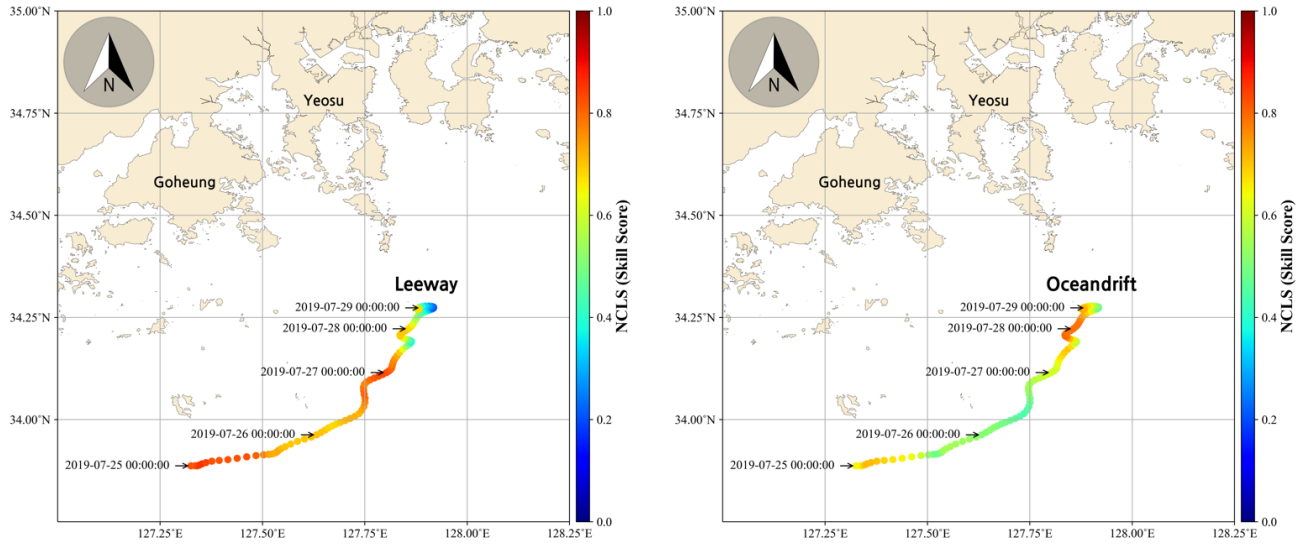

Fig. 12 Spatial distribution of NCLS skill scores based on the simulation execution locations (72 h after results): (a) leeway and (b) oceandrift

OpenDrift simulation showed that the leeway module demonstrated a high value of 0.8091 on average from the initial simulation start time of 0:00 on July 25 to 23:00 on July 26. It then showed a low value of 0.6040 on average from 0:00 on July 27 to 23:00 on July 28. The oceandrift module showed a low value of 0.5392 from 0:00 on July 25 to 23:00 on July 26 and a high value of 0.8000 on average from 0:00 on July 27 to 23:00 on July 28. Fig. 12 shows the spatial distribution of NCLS skill scores by location depending on the start time of the simulation. It shows that the predictive performance of the leeway module decreases when it is closer to land, while the oceandrift module's predictive performance increases when it is closer to land. These results are attributed to changes in the regional characteristics of external forces acting on the drifting bodies (such as ocean currents and wind) as the drifter moves north and approaches the land, as well as the limitations of numerical model resolution, which pose challenges in accurately representing the intricate coastline of the southern coast of South Korea.

4.3 Analysis of Usability in Maritime SAR

A polygonal area was generated by connecting the outermost points of the particles distributed every hour by OpenDrift, and the presence of drifters in this area was calculated for each simulation to compute the LPC. Fig. 13 shows the process of calculating LPC for the leeway module and the oceandrift module when the simulation starts at 0:00 on July 25, 2019. In Fig. 13(a), the drifter is included in the leeway module's predicted area while it is moving in the ENE direction, and it

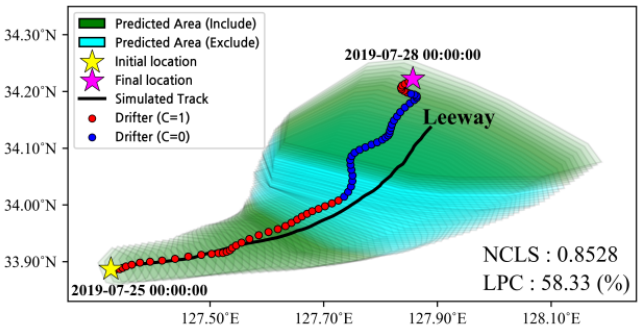

(a)

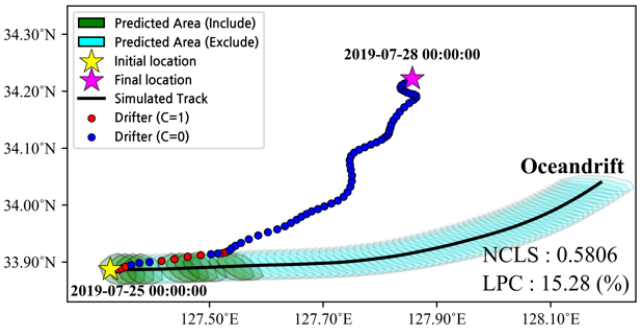

(b)

Fig. 13 Results of LPC calculations based on the simulation elapsed time: (a) leeway and (b) oceandrift

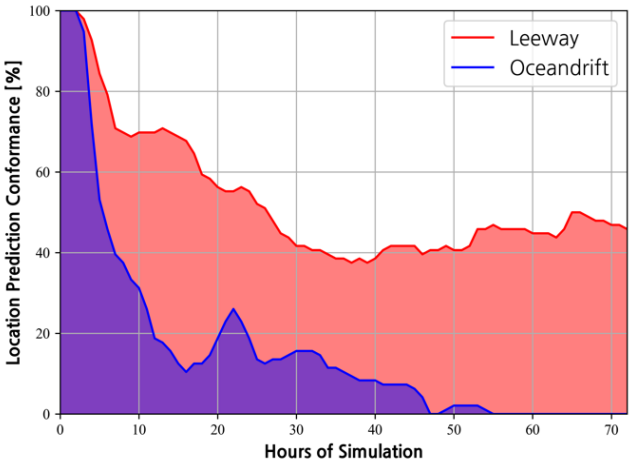

Fig. 14 Results of LPC calculations based on the simulation elapsed time (average across all simulations)

moves out of the predicted area as it moves north. It then reenters the area as it rotates near its final location. In Fig. 13(b), the drifter is included in the oceandrift prediction area in the initial few hours, but it deviates significantly from the prediction area afterward.

The average LPC over the elapsed time was 100% for up to 2 h into all simulations and then decreased as more time elapsed. Notably, the LPC of the oceandrift module decreased sharply as more simulation time elapsed, ultimately reaching 0%. However, the leeway module's LPC decreased as more simulation time elapsed and then maintained a certain level without a further decrease (Fig. 14). The average value for the entire elapsed simulation time was 53.51% for the leeway module and 16.50% for the Oceandrift module, indicating that the leeway

Table 5 Results of LPC based on the simulated elapsed time (1–14 h)

Time (h)	Modules		
	Leeway (%)	Oceandrift (%)	Difference (%)
1	100.00	100.00	0.00
2	100.00	100.00	0.00
3	97.92	94.79	3.12
4	92.71	71.88	20.83
5	84.38	53.12	31.25
6	79.17	45.83	33.33
7	70.83	39.58	31.25
8	69.79	37.50	32.29
9	68.75	33.33	35.42
10	69.79	31.25	38.54
11	69.79	26.04	43.75
12	69.79	18.75	51.04
13	70.83	17.71	53.12
14	69.79	15.62	54.17
Mean	79.54	48.96	30.58

module exhibited approximately 324% higher predictive performance than the oceandrift module.

According to Tipton et al. (2022), considering a typical scenario where a person in the water can survive for 14 h, the average performance during a 14-hour simulation period was found to be 79.54% for the leeway module and 48.96% for the oceandrift module. The leeway module exhibited approximately 162% higher prediction performance compared to the oceandrift module. Furthermore, the results at the 14-hour mark showed that the LPC was 69.79% for the leeway module and 15.63% for the oceandrift module. In this case, the leeway module demonstrated approximately 447% higher prediction performance compared to the oceandrift module (Table 5). The LPC score represents the probability of drifters being located within the predicted area of OpenDrift and consistently showed higher performance for the leeway module compared to the oceandrift module. Based on these findings, it is suggested that considering the leeway module is important when determining areas with a higher likelihood of maritime objects being present.

5. Conclusions

Unlike terrestrial distress, maritime distress necessitates swift and accurate location estimation as drifting objects gradually move away from the incident site. Taking into account the distinctive characteristics of maritime emergencies, which is characterized by significant uncertainties and potential human and property losses, this study employed OpenDrift to conduct drift trajectory prediction experiments. Specifically, the leeway module of OpenDrift, which accounts for the crucial leeway effect in maritime SAR operations, was utilized. A comparative analysis of the leeway module and the oceandrift module, which solely relies on ocean current information without considering the leeway effect, was performed. To assess the performance of OpenDrift, four evaluation methods, namely NCLS, RMSE, MAE, and Euclid, were employed to gauge the congruence between the actual drift trajectories and the simulation results. Furthermore, an LPC analysis was conducted to evaluate the practicality of OpenDrift in maritime SAR scenarios. The key findings derived from this study can be summarized as follows:

(1) The evaluation of drift trajectory prediction performance in OpenDrift simulations revealed that both the leeway module and the oceandrift module exhibited decreasing prediction performance with elapsed simulation time. After 72 h of simulation, the results of the leeway module showed higher scores in all evaluation metrics on average. However, when considering the error range, no significant difference was observed. Therefore, it can be concluded that there are limitations to assessing the prediction performance of simulations including leeway using this approach.

(2) The NCLS analysis results based on the simulated locations in OpenDrift showed variations in prediction performance depending on the initial locations. The leeway module yielded a high average value of 0.8091 when the simulation started from July 25th at 0:00 to July 26th at 23:00. However, when the simulation started from July 27th at 0:00 to July 28th at 23:00, the average value dropped to 0.6040. However, the oceandrift module exhibited a low average value of 0.5392 when the simulation started from July 25th at 0:00 to July 26th at 23:00 and a relatively high average value of 0.8000 when the simulation started from July 27th at 0:00 to July 28th at 23:00. This can be attributed to the changing regional characteristics of external forces acting on the drifting objects, such as ocean currents and wind, as the drifter moves northward and closer to the land. Additionally, it is considered that the limitations of the numerical model resolution used in OpenDrift simulations in accurately representing the complex coastline of the southern coast of South Korea contributed to these results.

(3) Finally, in the LPC analysis, which evaluated the usability of the OpenDrift simulation results for maritime SAR, the leeway module showed average prediction performance that was approximately 324% higher than that of the Oceandrift module. Furthermore, when considering the maximum survivable time for a person in the water in general situations, which is 14 h, the leeway module exhibited approximately 447% higher prediction performance compared to the oceandrift module. Therefore, this study suggests that considering the leeway effect in drift trajectory prediction experiments can lead to higher probabilities of drifters being present within a predicted area, thereby enhancing the applicability of such predictions in maritime SAR operations.

This study confirmed that considering the leeway effect can be helpful in predicting areas with a higher likelihood of containing the actual locations of maritime drifting objects during drift trajectory prediction. The results of this study were quantitatively presented. Therefore, these findings can be utilized in evaluating and improving drift trajectory prediction techniques employed by maritime SAR organizations such as the KCG and KHOA. Additionally, these results are expected to have applicability beyond maritime disasters and can be extended to the prediction of drift trajectories for other floating objects, including marine debris, satellite buoys, and sea ice.

In future research, it will be necessary to use numerical model data with higher resolution to accurately simulate the intricate coastline of South Korea. Additionally, conducting field experiments to more accurately simulate the leeway effect on the target drifters would further enhance the usability of research results. However, it should be noted that this study was limited to the Korea Strait. By conducting OpenDrift research considering the characteristics of various maritime areas in South Korea, which is surrounded by sea on three sides, and validating them based on real maritime distress cases, it is believed that it can greatly contribute to future maritime SAR operations.

Conflict of Interest

Sungwon Shin serves as an editorial board member of the Journal of Ocean Engineering and Technology, but he had no role in the decision to publish this article. No potential conflict of interest relevant to this article is reported.

Funding

This research was partially supported by the Korea Institute of Marine Science & Technology Promotion (KIMST), which is funded by the Korea Coast Guard (20220463), and by the Korea Evaluation Institute of Industrial Technology (KEIT) grant, which is funded by the Korean government (KCG, MOIS, NFA) [RS-2022-001549812, Development of technology to respond to marine fires and chemical accidents using wearable devices].

References

Allen, A., & Plourde, J. V. (1999). *Review of leeway: Field experiments and implementation* (Report No. CG-D-08-99). U.S. Coast Guard Research and Development Center. https://apps.dtic.mil/sti/pdfs/ADA366414.pdf

Breivik, Ø., & Allen, A. A. (2008). An operational search and rescue model for the Norwegian Sea and the North Sea. *Journal of Marine Systems, 69*(1−2), 99−113. https://doi.org/10.1016/j.jmarsys.2007.02.010

Centurioni, L., Horányi, A., Cardinali, C., Charpentier, E., & Lumpkin, R. (2017). A global ocean observing system for measuring sea level atmospheric pressure: Effects and impacts on numerical weather prediction. *Bulletin of the American Meteorological Society, 98*(2), 231−238. https://doi.org/10.1175/BAMS-D-15-00080.1

Cho, K. -H., Li, Y., Wang, H., Park, K. -S., Choi, J. -Y., Shin, K. -I., & Kwon, J. -I. (2014). Development and validation of an operational search and rescue modeling system for the Yellow Sea and the East and South China Seas. *Journal of Atmospheric and Oceanic Technology, 31*(1), 197−215. https://doi.org/10.1175/JTECH-D-13-00097.1

Dagestad, K. -F., Röhrs, J., Breivik, Ø., & Ådlandsvik, B. (2018). OpenDrift v1.0: A generic framework for trajectory modelling. *Geoscientific Model Development, 11*(4), 1405−1420. https://doi.org/10.5194/gmd-11-1405-2018

Dominicis, M. D., Pinardi, N., Zodiatis, G., & Archetti, R. (2013). MEDSLIK-II, a Lagrangian marine oil spill model for short-term forecasting - Part 2: Numerical simulations and validations. *Geoscientific Model Development Discussions, 6*, 1999−2043.

Ha, S. Y., Yoon, H.-S., & Kim, Y.-T. (2022). A study on the prediction of the surface drifter trajectories in the Korean Strait. *Journal of Korean Society of Coastal and Ocean Engineers, 34*(1), 11−18. https://doi.org/10.9765/KSCOE.2022.34.1.11

Hufford, G. L., & Broida, S. (1974). *Determination of small craft leeway* (Report No. CGR&DC 39/74). U.S. Coast Guard Research and Development Center.

Kang, S. -Y. (1998). Analysis of drift prediction formula used in the search and rescue mission. *Journal of Korean Port Research, 12*(2), 373−384.

Kim, G. -D., & Kim, Y. -H. (2018). Improved correction of drifter data using deep neural networks. *Journal of Korean Institute of Intelligent Systems, 28*(5), 443−449. https://doi.org/10.5391/JKIIS.2018.28.5.443

Kim, T. -Y., & Yoon, H. -S. (2011). Skill assessments for evaluating the performance of the hydrodynamic model. *Journal of the Korean Society for Marine Environment & Energy, 14*(2), 107−113. https://doi.org/10.7846/JKOSMEE.2011.14.2.107

Korea Coast Guard (KCG). (2022a). *2021 해양경찰 백서* [2021 Coast Guard White Paper]

Korea Coast Guard. (2022b). *2021 해상조난사고 통계연보* [2021 Sstatistical yearbook of maritime distress accidents].

Korea Hydrographic and Oceanographic Agency (KHOA). (2022). *2021 해양조사기술연보* [Yearbook of marine survey].

Lee, C. -J., Kim, G. -D., & Kim, Y. -H. (2017). Performance comparison of machine learning based on neural networks and statistical methods for prediction of drifter movement. *Journal of the Korea Convergence Society, 8*(10), 45−52. https://doi.org/10.15207/JKCS.2017.8.10.045

Lee, M., Gong, I.-Y., & Kang, C.-G. (1999). Tracking model of drifted ships for search and rescue. *Journal of the Korean Society for Marine Environmental Engineering, 2*(2), 78−85.

Liu, Y., & Weisberg, R. H. (2011). Evaluation of trajectory modeling in different dynamic regions using normalized cumulative lagrangian separation. *Journal of Geophysical Research, 116*(C9), C09013. https://doi.org/10.1029/2010JC006837

Lumpkin, R., & Pazos, M. (2007). Measuring surface currents with surface velocity program drifters: the instrument, its data, and some recent results. In A. Griffa, A. D. Kirwan, Jr., A. J. Mariano, T. Özgökmen, & H. T. Rossby (Eds.), *Lagrangian Analysis and Prediction of Coastal and Ocean Dynamics* (1st ed, pp 39−67). Cambridge University Press. https://doi.org/10.1017/CBO9780511535901.003

Nam, Y. -W., & Kim, Y. -H. (2018). Prediction of drifter trajectory using evolutionary computation. *Discrete Dynamics in Nature and Society, 2018*, 1−15. https://doi.org/10.1155/2018/6848745

Park, K. -S., Gang, S. -W., & Gang, S. -K. (1989). *수색구조를 위한 표류치 추정* [Estimation of drift value for search and rescue]. Korea Fisheries Infrastructure Promotion Association, 8, 85−88.

Seo, J. -H. (2021). Prediction of surface drifter trajectory based on feature generation. *Journal of Korean Institute of Intelligent Systems, 31*(4), 299−304. https://doi.org/10.5391/JKIIS.2021.31.4.299

Tipton, M., McCormack, E., Elliott, G., Cisternelli, M., Allen, A., & Turner, A. C. (2022). Survival time and search time in water: Past, present and future. *Journal of Thermal Biology, 110, 103349. https://doi.org*/10.1016/j.jtherbio.2022.103349

Yun, J. -H. (2005). Measures to enhance the Korean marine SAR systems. *Proceedings of the 2015 Fall Conference of the Korean Society of Marine Environment and Safety*, 7−14.

Yun, J.-H. (2020). *해양수색구조(SAR) 관련 기술개발 과제에 대한 고찰* [Reflection on technological development challenges in maritime search and rescue (SAR)]. Korea Institute of Marine Science & Technology Promotion.

Yun, J. -H., Lee, M. -J., Jang, H. -L., & Koh, S. (2001). A study on the improvement of SAR capabilities in Korea-Analysis of marine casualties and leeway field experiment-. *Journal of the Korean Society of Marine Environment and Safety, 7*(2), 13−22.

Author ORCIDs

Author name	ORCID
Kim, Ji-Chang	0000-0002-0150-0184
Yu, Dae Hun	0009-0006-0403-9465
Sim, Jung-eun	0009-0005-5726-5848
Son, Young-Tae	0000-0001-7985-6722
Bang, Ki-Young	0000-0002-5523-5849
Shin, Sungwon	0000-0002-4564-2627

KSOE

Journal of Ocean Engineering and Technology 37(4), 158-163, August, 2023
https://doi.org/10.26748/KSOE.2023.023

pISSN 1225-0767
eISSN 2287-6715

Original Research Article

Location Tracking of Drifting Container by Solitary Wave Load Using a Motion Analysis Program

Taegeon Hwang[1], Jiwon Kim[2], Dong-Ha Lee[3] and Jae-Cheol Lee[4]

[1]*Graduate Student, Department of Ocean Civil Engineering, Gyeongsang National University, Tongyeong, Korea*
[2]*Senior Engineer, Offshore Infrastructure Team, Harbor Department, Yooshin Engineering Corporation, Seoul, Korea*
[3]*Associate Professor, Department of Integrated Energy and Infra System, Kangwon National University, Chuncheon, Korea*
[4]*Graduate Student, Department of Integrated Energy and Infra System, Kangwon National University, Chuncheon, Korea*

KEYWORDS: Location tracking, Drifting objects, Drifting behavior, DIPP-Motion analysis, Solitary waves, Tsunamis

ABSTRACT: *Objects adrift can cause considerable damage to coastal infrastructure and property during tsunami and storm surge events. Despite the potential for harm, the drifting behavior of these objects remains poorly understood, thereby hindering effective prediction and mitigation of collision damage. To address this gap, this study employed a motion analysis program to track a drifting container's location using images from an existing laboratory experiment. The container's trajectory and velocity were calculated based on the positions of five markers strategically placed at its four corners and center. Our findings indicate that the container's maximum drift velocity and distance are directly influenced by the scale of the solitary wave and inversely related to the container's weight. Specifically, heavier containers are less likely to be displaced by solitary waves, while larger waves can damage coastal structures more. This study offers new insights into container drift behavior induced by solitary waves, with implications for enhancing coastal infrastructure design and devising mitigation strategies to minimize the risk of collision damage.*

1. Introduction

A tsunami is a phenomenon triggered by the displacement of the seafloor or the release of energy from an undersea earthquake or volcanic eruption. This event leads to alterations in water levels that propagate over great distances, eventually impacting coastlines with considerable force and causing extensive flooding in coastal areas. As the tsunamis advance, they carry coastal debris, which can collide with structures and inflict substantial damage. Factors such as flow velocity, debris collision, and scour cumulatively affect structures in the tsunami's path (Charvet et al., 2015). Consequently, isolating the damage caused by drifting objects during post-tsunami assessments is challenging. While studies have shown that debris collision can result in structural damage and elevate the risk of building collapse, these collision forces have not been extensively incorporated into structural design considerations (Naito et al., 2014). Moreover, a numerical analysis by Ma et al. (2021) that modeled typical wooden buildings in coastal areas found that including remnants of collapsed structures in their simulations led to a remarkable 150% increase in building failures due to tsunami forces.

Charvet et al. (2015) conducted a vulnerability analysis, concluding that the impact force exerted by floating objects during a tsunami is a crucial determinant of structural collapse risk. Similarly, Palermo et al. (2013) conducted a field investigation of the 2010 Chile Tsunami, finding that impact forces generated by large drifting objects could devastate most structures, especially critical load-bearing components like columns. In the 2011 Tohoku Tsunami, numerous structures succumbed to collision damage from floating debris, including drifting objects (Naito et al., 2014). Furthermore, instances of collision damage involving drifting objects such as storage tanks, trucks, and ships was documented during the 2018 Sunda Strait Tsunami (Stolle et al., 2020).

To understand secondary disaster aspects of tsunamis, such as the collision risks posed by drifting objects, it's essential to first study the behavior of these objects in fluid motion. In this context, Kim et al. (2023) utilized an OpenCV library-based red-green-blue (RGB) analysis approach to track the position of a drifting container affected by a solitary wave cresting over a revetment. This method remains

Received 3 August 2023, revised 13 August 2023, accepted 23 August 2023
Corresponding author Jae Cheol Lee: +82-33-250-6232, essentialee@kangwon.ac.kr

effective even when the drifting objects are overturned as long as the RGB values for the object's side or bottom fall within a predefined range. However, the approach has limitations: it can only track the center of a recognized object, making it less effective at monitoring spinning objects or tracking multiple drifting objects simultaneously.

To overcome these limitations, this study employs the motion analysis program digital image post-processing motion (DIPP-Motion) to track the position of a drifting container affected by solitary waves. We used images from a laboratory experiment conducted by Kim et al. (2023) for this purpose. Five markers were placed on the container: one at each of its four corners and one at the top center. The positions of the drifting objects were then tracked, considering the scale of the solitary wave and the object's weight. This method also allowed for a detailed examination of object behaviors, such as rotation.

2. Method

2.1 Laboratory Experiment

Kim et al. (2023) captured images of containers in motion within a two-dimensional wave tank measuring 37 m in length, 0.6 m in width, 1 m in height, and a water depth (h) of 47 cm. In this experiment, a freeboard (F_b) with a surface height of 5 cm and a total height of 52 cm —constructed from waterproof plywood—is positioned 27.05 m away from the wave paddle, as depicted in Fig. 1. The average roughness of the painted revetment's vertical walls and the land area floor is 0.56 mm. As detailed in Table 1, 1/40-scale container models situated 10 cm from the vertical wall are categorized into two types: half-full (Model-A; $W_{total} = W_0 + W_{\max}/2$) and full models (Model-B; $W_{total} = W_0 + W_{\max}$). These acrylic container models were fabricated according to International Organization for Standardization (ISO) specifications. Table 2 outlines the experimental conditions related to solitary wave heights (A) employed by Kim et al. (2023).

Two cameras were mounted on the revetment to capture a 310-cm section. The images were taken at approximately 0.0167 s intervals, equating to 60 frames per second (fps). Grids were marked on the revetment at 10 cm intervals for drift distance measurement and camera calibration, as shown in Fig. 2.

2.2 DIPP-Motion

In this study, DIPP-Motion (DITECT, 2023), a motion analysis program, was used to assess the drifting behavior of containers affected by solitary waves. The program tracks specified markers by converting the analysis region into grayscale. Using a 10 cm × 10 cm grid scale projected onto the floor of the land area, the distance per pixel can be estimated. Subsequently, a total of five markers are set: one at the center point on the container's upper surface and one at each of its four corners. The program then tracks the container as it drifts due to the solitary wave, as shown in Fig. 2. Velocity and acceleration

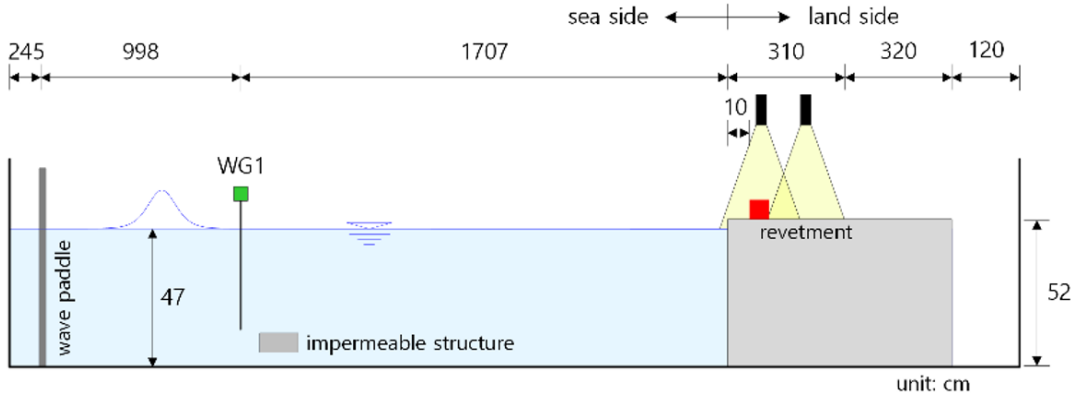

Fig. 1 Conceptual diagram of the wave flume used in the laboratory experiment by Kim et al. (2023).

Table 1 Specifications of a 20 ft container based on ISO standard

20 ft container	Length (mm)	Width (mm)	Height (mm)	Weight W_0 (kg)	Maximum cargo $W_{\max}$ (kg)	Maximum weight W_{total} (kg)
Prototype	6,058	2,438	2,591	2,250	28,230	30,480
Model-A	151	61	65	0.035	0.441	0.256
Model-B						0.476

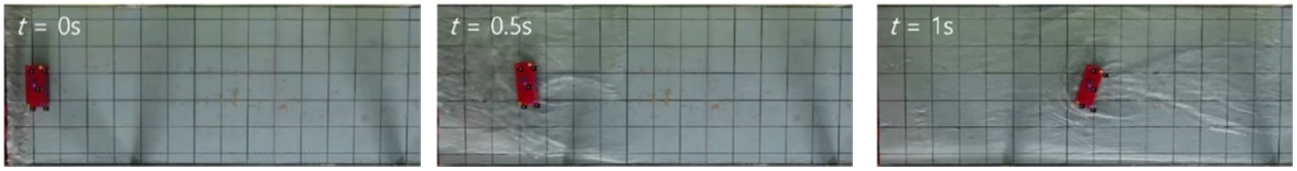

Fig. 2 Tracking process of markers set on the drifting container.

Table 2 Incident wave conditions used in the laboratory experiment

Run	A (cm)	ϵ (A/h)	A/F_b
1	4.4	0.09	0.88
2	5.4	0.12	1.08
3	6.3	0.13	1.26
4	7.2	0.15	1.44
5	8.2	0.18	1.64
6	10	0.21	2
7	12.3	0.26	2.46
8	14.5	0.31	2.9
9	16.5	0.35	3.3
10	18.7	0.4	3.74
11	21.5	0.46	4.3

are calculated based on the markers' initial location and subsequent positions in each frame, factoring in the time interval between the captured image frames.

3. Results

3.1 Effect of Solitary Wave Scale

The scale of the solitary wave is represented by its height. Fig. 3 compares the drift behavior under two different incident solitary wave conditions, specifically $\epsilon = 0.13$ and $\epsilon = 0.18$. Fig. 4 illustrates the spatial distribution of the moving trajectory and velocity of the drifting container under these solitary wave conditions. In Fig. 3, the container model's initial point of drift (t_0) is the reference for the dimensionless time variable, $t^* = (t - t_0)\sqrt{g/h}$, where g is the gravitational acceleration. In Fig. 4, the horizontal distances x and y, as well as the container's moving velocity (V), are non-dimensionalized by dividing them by the sea depth (h) and the solitary wave velocity ($\sqrt{g/h}$), respectively.

The data presented in Fig. 3 demonstrate that the container's moving velocity is higher at $\epsilon = 0.18$ than at $\epsilon = 0.13$, and the drift distance over the same period is also greater when the solitary wave scale is high. According to Lee et al. (2022a), a larger solitary wave scale leads to increased rates of overtopping, and as per Lee et al. (2022b), this results in greater inundation depths in the land area. Consequently, the buoyant force acting on the container increases, reducing floor friction. Furthermore, Fig. 4 reveals that at $\epsilon = 0.18$, the initial acceleration of the drifting container is substantial, the acceleration phase is extended, and the maximum drifting velocity also increases.

Fig. 5 shows the container's maximum drifting velocity (V_{max}) and maximum drifting distance (d_{max}) in dimensionless terms, normalized by the wave speed ($\sqrt{g/h}$) and sea depth (h), respectively. Herein, d_{max} is omitted when it cannot be measured, as it falls outside the 6.3

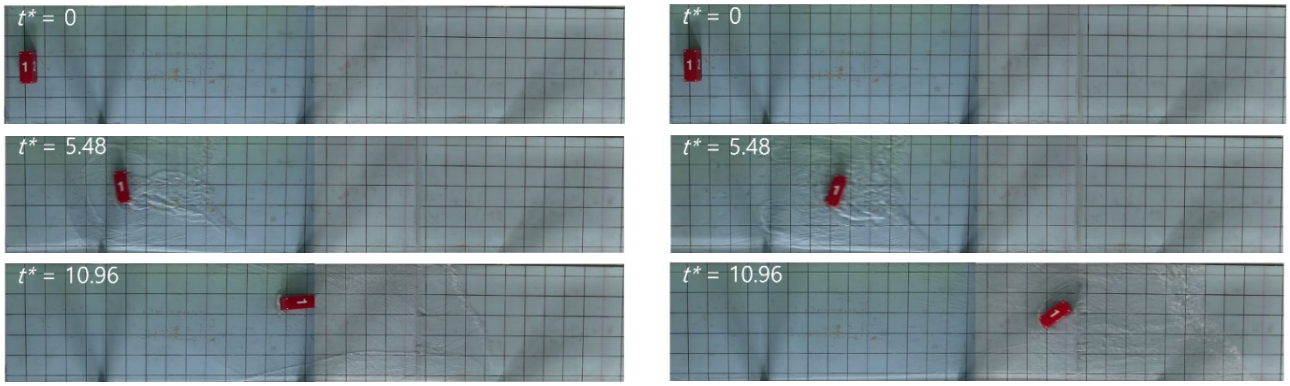

Fig. 3 Container's drifting behavior by solitary wave at $\epsilon = 0.13$ (left) and $\epsilon = 0.18$ (right)

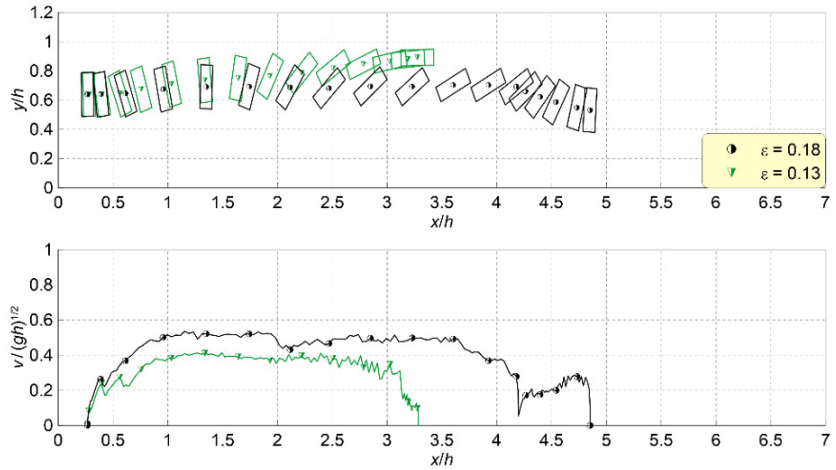

Fig. 4 Spatial distributions of the trajectory (top) and moving velocity (bottom) of the drifting container according to ϵ

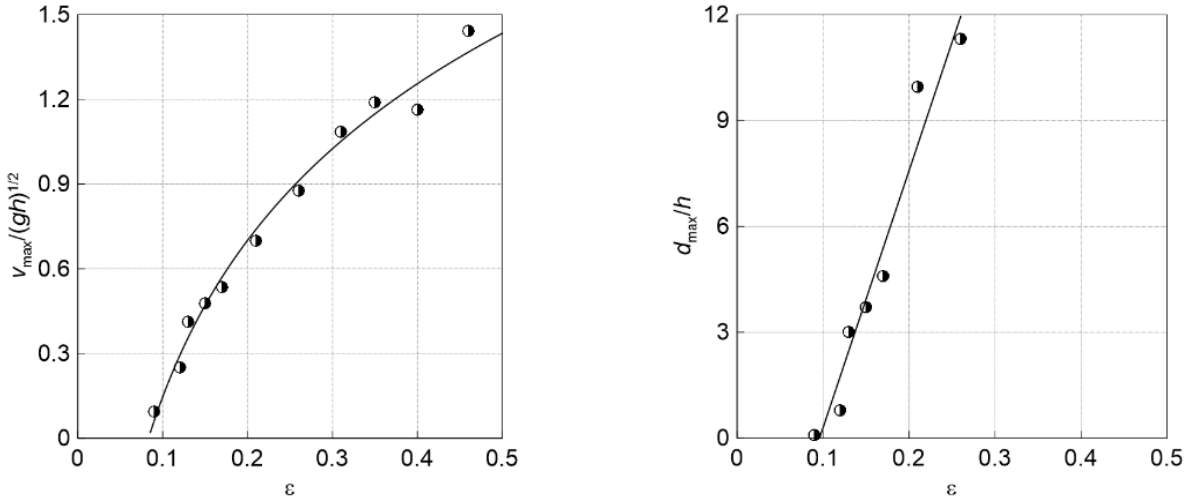

Fig. 5 Maximum drifting velocity (left) and maximum drifting distance (right) of Model-A according to ϵ

m-high land area.

The ratio $V_{\max}/\sqrt{gh}$ increases sharply with the size of the solitary wave. After this rapid increase, the rate of increment starts to taper off. Similarly, $d_{\max}/h$ rises with ϵ. However, a clear trend could not be determined since measurements were not captured for all four incident solitary wave conditions.

3.2 Effect of Container Weigt

Fig. 6 shows the drifting behavior of the container, emphasizing the influence of cargo weight under the solitary wave condition characterized of $\epsilon = 0.18$. Meanwhile, Fig. 7 depicts the movement trajectory and velocity. Models A and B possess weights (W_{total}) of $W_0 + W_{\max}/2$ and $W_0 + W_{\max}$, respectively. Here, W represents the

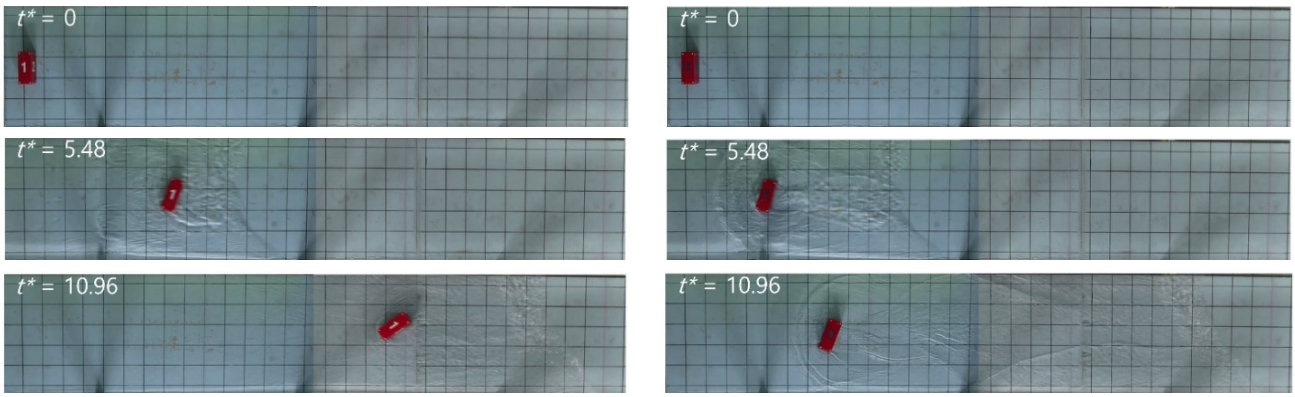

Fig. 6 Drifting behaviors of Container Model-A (left) and Model-B (right) by solitary wave

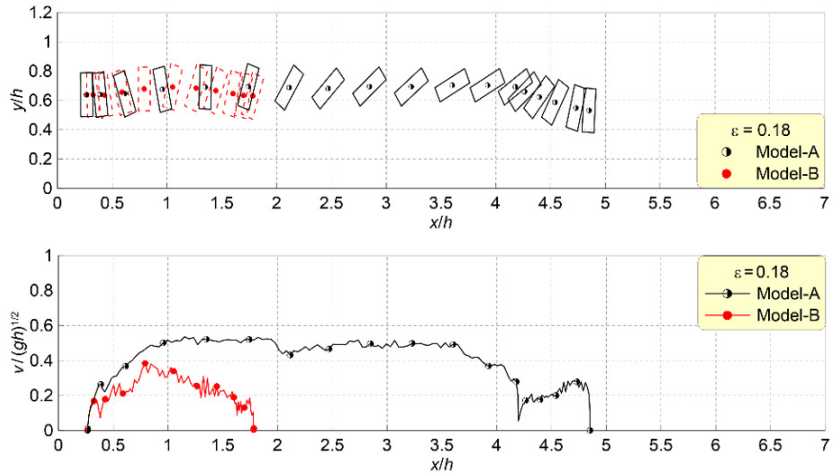

Fig. 7 Spatial distributions of the trajectory (top) and moving velocity (bottom) by solitary wave

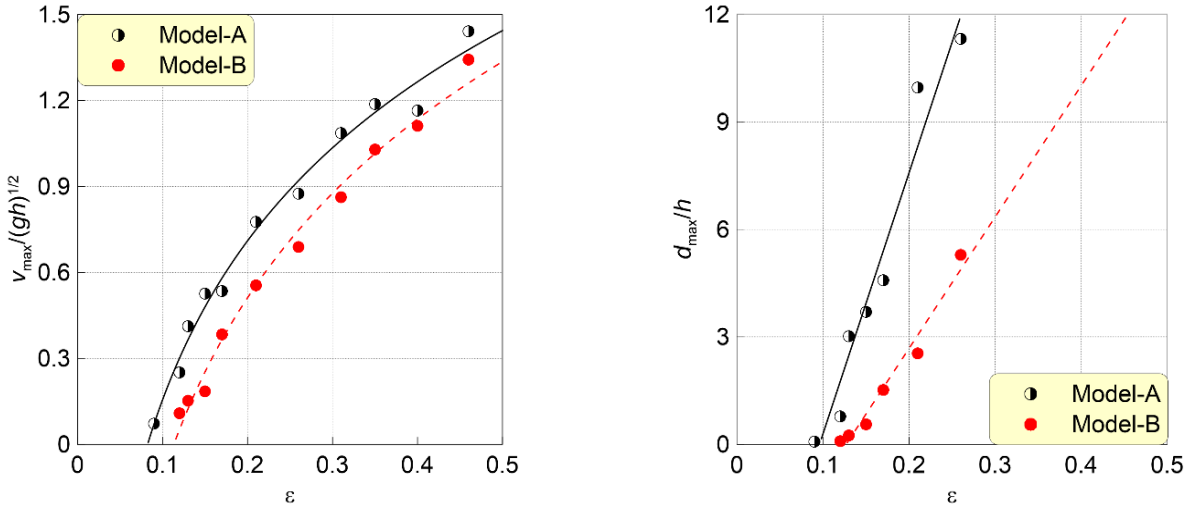

Fig. 8 Distribution of the maximum drifting velocity (left) and maximum drifting distance (right) of the drifting container according to ϵ: comparison according to container weight

combined weight of the empty container and the maximum loaded cargo.

As suggested in Figs. 6 and 7, the difference in the location of the drifting containers, Model-A and Model-B, increases over time under the influence of the solitary wave. Model-B, despite its heavier weight, exhibits lower initial acceleration, moving velocity, and drifting distance compared to Model-A. In the same solitary wave scenario, the buoyant force acts differently based on the container model's weight, leading to this observed trend. Specifically, Model-A, being relatively lighter, experiences better buoyancy at the same depth of immersion, which in turn reduces floor friction. As a result, when comparing $V_{max}/\sqrt{gh}$ and d_{max}/h of the drifting container as influenced by the solitary wave based on container weight in Fig. 8, both $V_{max}/\sqrt{gh}$ and d_{max}/h generally show less dispersion for Model-A due to its lighter weight.

4. Discussion

In this study, the drifting characteristics of containers influenced by solitary waves, as determined through DIPP-Motion, closely align with the findings of Kim et al. (2023), who utilized an OpenCV library-based RGB analysis technique. Nevertheless, the present investigation allowed for discernment of the container's rotation during drifting and pinpointing the final stationary position of the container—observations that were elusive in the study by Kim et al. (2023). Additionally, despite the experiment's two-dimensional cross-sectional nature, the container exhibited a deviation angle relative to the y-direction center. This might be attributed to inconsistent floor friction or the possibility that the solitary wave did not apply a uniformly distributed load on the container. A positioning technology that can integrate real-time geometric information of drifting objects is essential to fully understand and capture this behavior.

When drifting objects become overturned, DIPP-Motion's location tracking struggles to detect predefined markers. However, our approach has an advantage in that it can concurrently monitor the positions of multiple drifting objects, given its capability to handle several markers simultaneously.

5. Conclusions

This study seeks to explore the drifting behavior of containers influenced by solitary waves, utilizing DIPP-Motion as the motion analysis tool. The overarching aim is to understand tsunamis' secondary disaster characteristics better, focusing on collisions involving drifting objects. Through DIPP-Motion analysis, we examined how the behavior of drifting containers varies with the solitary wave's scale and the container's weight.

As the solitary wave scale grows, both the traveling velocity of the wave and the displacement of the drifting container see a corresponding increase. This behavior can be attributed to larger solitary wave heights resulting in increased immersion depths. This increased depth subsequently diminishes bottom friction and amplifies buoyancy effects. Furthermore, the research indicates that lighter containers, while maintaining a consistent submerged depth, drift at faster velocities and traverse greater distances compared to their heavier counterparts, largely owing to decreased floor friction.

The analytical results related to the drifting behavior of containers propelled by solitary waves emphasize that the scope of secondary disaster damage from collisions is likely to increase with larger tsunami or storm surge scales. Lighter drifting objects are prone to higher velocities, which could affect collision dynamics. However, objects with lower weights generally exert weaker collision forces. As a result, the findings from this study alone make it difficult to precisely quantify the degree of collision damage and to fully understand the complex interplay between the movement velocity and weight of drifting objects.

To further investigate this matter, a follow-up study will conduct hydraulic experiments and computational analyses to examine collision forces. These explorations will focus on determining the relationships between the weight of drifting objects and their collision velocities.

Conflict of Interest

No potential conflicts of interest related to this article were reported.

Funding

This work was supported by the National Research Foundation of Korea (NRF) grant funded by the Korea government (MSIT) (No. 2021R1F1A1062767).

References

Charvet, I., Suppasri, A., Kimura, H., Sugawara, D., & Imamura, F. (2015). A multivariate generalized linear tsunami fragility model for Kesennuma City based on maximum flow depths, velocities and debris impact, with evaluation of predictive accuracy. *Journal of Natural Hazards*, 79(3), 2073−2099.

Digital Image Technology Corporation. (DITECT). (2023). *2D/3D motion analysis software [DIPP-Motion V]*. Digital Image Technology Corporation. https://www.ditect.co.jp/en/software/dipp_motionv.html

Kim, T., Hwang, T., Baek, S., Hong, S., Kim, J., & Lee, W.-D. (2023). Experimental investigations using computer vision for debris motion generated by solitary waves. *Journal of Earthquake and Tsunami*, 291, 108434.

Lee, W. -D., Choi, S., Kim, T., & Yeom, G. -S. (2022a). Comparison of solitary wave overtopping characteristics between vertical and wave absorbing revetments. *Ocean Engineering*, 256, 111542.

Lee, W. -D., Hwang, T., & Kim, T. (2022b). Inundation characteristics of solitary waves according to revetment type. *Water*, 14, 3814.

Ma, X., Zhang, W., Li, X. & Ding, Z. (2021). Evaluating tsunami damage of wood residential buildings in a coastal community considering waterborne debris from buildings. *Engineering Structures*, 244, 112761.

Naito, C., Cercone, C., Riggs, H. R., & Cox, D. (2014). Procedure for site assessment of the potential for tsunami debris impact. *Journal of Waterway Port Coastal and Ocean Engineering, 140, 223−232.*

Palermo, D., Nistor, I., Saatcioglu, M., & Ghobarah, A. (2013). Impact and damage to structures during the 27 February 2010 Chile tsunami. *Canadian Journal of Civil Engineering*, 40(8), 750−758.

Stolle, J., Krautwald, C., Robertson, I., Achiari, I., Mikami, T., Nakamura, R., Takabatake, T., Nishida, Y., Shibayama, T., Esteban, M., Nistor, I., & Goseberg. N. (2020). Engineering lessons from the 28 September 2018 Indonesian tsunami: debris loading. *Canadian Journal of Civil Engineering*, 47(1), 1−12.

Author ORCIDs

Author name	ORCID
Hwang, Taegeon	0000-0002-4959-3906
Kim, Jiwon	0009-0009-4959-4827
Lee, Dong-Ha	0000-0002-6934-1247
Lee, Jae-Cheol	0000-0002-0242-4961

KSOE

Journal of Ocean Engineering and Technology 37(4), 164-171, August, 2023
https://doi.org/10.26748/KSOE.2023.012

pISSN 1225-0767
eISSN 2287-6715

Original Research Article

Study on the Vibration Characteristics of Yaw Gear System for Large-Capacity Offshore Wind Turbine

HyoungWoo Lee[1], SeoWon Jang[2] and Seok-Hwan Ahn[3]

[1]*Professor, Department of Unmanned Aero Mechanical Engineering, Jungwon University, Goesan, Korea*
[2]*Graduate Student, Department of Convergence Engineering, Jungwon University, Goesan, Korea*
[3]*Professor, Department of Unmanned Aero Mechanical Engineering, Jungwon University, Goesan, Korea*

KEYWORDS: Yaw gear system, Natural frequency, Critical speed, Campbell diagram, Load duration distribution

ABSTRACT: *Vibration and noise must be considered to maximize the efficiency of a yaw system and reduce the fatigue load acting on a wind turbine. This study investigated a method for analyzing yaw-system vibration based on the change in the load-duration distribution (LDD). A substructure synthesis method was combined with a planetary gear train rotational vibration model and finite element models of the housing and carriers. For the vibration excitation sources, the mass imbalance, gear mesh frequency, and bearing defect frequency were considered, and a critical speed analysis was performed. The analysis results showed that the critical speed did not occur within the operating speed range, but a defect occurred in the bearing of the first-stage planetary gear system. It was found that the bearing stiffness and first natural frequency increased with the LDD load. In addition, no vibration occurred in the operating speed range under any of the LDD loads. Because the rolling bearing stiffness changed with the LDD, it was necessary to consider the LDD when analyzing the wind turbine vibration.*

1. Introduction

A wind turbine typically consists of a blade rotor that transfers the received energy to a generator, a power transfer unit, a nacelle in which the generator and various electrical and mechanical devices are installed, and a tower that supports the weight of the nacelle assembly and load delivered through the blade (Hong et al., 2006). Because even a single malfunction of a wind-power generation system can induce significant economic and social losses, only products that can guarantee at least 20 years of service life can enter the commercial market. In addition to the increase in the size of the system, consideration must be given to vibration, noise, and weight reduction when designing a gearbox because a service life of at least 20 years must be guaranteed (Lee and Kang, 2014).

A yaw system maximizes the system efficiency and reduces the fatigue load acting on a wind turbine by positioning the rotor and nacelle so that they face in the direction that the wind is blowing. The vibration and noise of the yaw system must be taken into account because a wind turbine must be guaranteed a service life of at least 20 years. Accordingly, continuous research has been conducted on the vibration and noise of rotary machines. Itoh studied a method of using a damped free vibration mode shape for systems with complex structures (Itoh, 1973). Kahraman et al. (1992) calculated the critical speed considering the torsion of a gear and coupled effects of bending vibration, and found the response for an unbalanced mass and transmission error using a finite element method. To analyze the response of a planetary gear train using the finite element method, Parker et al. (2000) designed a finite element model of a planetary gear train and analyzed the dynamic response and unique characteristics such as the natural frequency and vibration modes. Dong et al. (2015) researched non-linear dynamic modeling, including torsion modeling, in order to examine the vibration characteristics of a planetary gear. Wang and Morse (1972) performed static and dynamic torsion response analyses of a general gear train system using a transfer matrix method. Choy et al. (1991) analyzed the steady state response by developing a three-stage spur gear system model that included the torsion of a gear train. To improve the analysis techniques for complex planetary gear systems considering various types of frictions, Tanaka analyzed the characteristics of a planetary gear in the form of a matrix by finding system equations from element equations, corresponding to the finite element method (FEM) (Tanaka, 1984). Iida et al. (1980) claimed that a gear train model yielded different results depending on

Received 10 May 2023, revised 6 July 2023, accepted 19 July 2023
Corresponding author Seok-Hwan Ahn: +82-43-830-8942, shahn@jwu.ac.kr

whether the dynamic coupling of a spur gear was considered. Bossanyi studied a method for controlling the torque applied to the yaw to balance the energy according to the load and for individually controlling the yaw system to reduce loads applied asymmetrically (Bossanyi, 2005). Prohl proposed a transfer matrix model of a gear train, and analyzed the critical speed, dynamic response, and unique characteristics of this gear train supported by a bearing based on the transfer matrix method (Prohl, 1945).

The aforementioned studies performed vibration analyses only for a gear train without considering the finite element models of the housing and carriers. Therefore, there is a need for a vibration analysis that considers a finite element model of the housing and gear, as well as the planetary gear train.

This study examined the vibration characteristics of the yaw system for a large-capacity wind turbine, and proposed a method for performing a vibration analysis of the yaw system by combining finite element models of the housing and carriers with a rotor vibration model of the planetary gear train using a substructure synthesis method. Furthermore, the characteristics were analyzed by comparing the natural frequency results with and without consideration given to the finite elements of the housing and carriers. The vibration excitation sources for the bearing defect error, gear mesh frequency, and mass imbalance acting on the yaw system were modeled, and the critical speed was analyzed to determine the resonance within the scope of the operation speed range.

2. Vibration Modeling and Vibration Characteristic Analysis of the Yaw System

2.1 Vibration Modeling of the Yaw System

In this study, modeling was performed using an 8-MW yaw decelerator model. The vibration model of the yaw system was designed using MASTA 12.1, which is a gear analysis program. Fig. 1 shows the vibration model of the yaw system, which consisted of a four-stage planetary gear system. The output axis of each stage, when a ring gear was fixed, was connected to the subsequent input axis through a spline. The power of a motor input through the first sun gear was delivered to the output axis through the second, third, and fourth planetary gear systems.

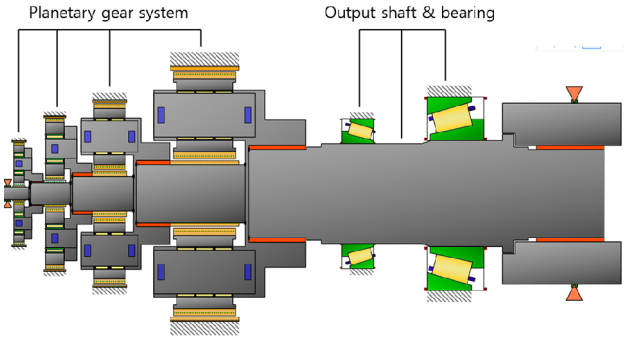

Fig. 1 Two-dimensional vibration model of yaw gear system

Table 1 Planetary information for 1st stage of yaw gear system

Stage 1	Sun	Planetary	Ring
Planetary gear		3	
Module		1.75	
Pressure angle (°)		20	
Number of teeth	14	39	94
Center distance (mm)		47.6	
Reduction ratio		7.714	

Table 2 Planetary information for 2nd stage of yaw gear system

Stage 2	Sun	Planetary	Ring
Planetary gear		3	
Module		2.5	
Pressure angle (°)		25	
Number of teeth	17	39	97
Center distance (mm)		71.7	
Reduction ratio		6.706	

Table 3 Planetary information for 3rd stage of yaw gear system

Stage 3	Sun	Planetary	Ring
Planetary gear		4	
Module		3.5	
Pressure angle (°)		25	
Number of teeth	21	30	83
Center distance (mm)		91.4	
Reduction ratio		4.952	

Table 4 Planetary information for 4th stage of yaw gear system

Stage 4	Sun	Planetary	Ring
Planetary gear		4	
Module		5	
Pressure angle (°)		25	
Number of teeth	21	28	79
Center distance (mm)		125.5	
Reduction ratio		0.950	

Detailed specifications of the four stages of the planetary gear system are presented in Tables 1, 2, 3, and 4, respectively. The reduction ratios of the planetary gear system were 7.714 in stage 1, 6.706 in stage 2, 4.952 in stage 3, and 0.95 in stage 4; the overall reduction ratio was approximately 1,219.96, with the 1,158.961 rpm rotational speed of the motor input in the first sun gear decelerated to 0.47 rpm.

2.2 Vibration Characteristic Analysis of the Yaw System

Most structural analyses are performed based on the finite element method, but an extensive amount of time is required for computing and dividing the mesh for large structures. To overcome this drawback, the

entire structure was divided into several elements, and then each modal variable was independently determined for each element. The elements were then synthesized using geometric suitability conditions for the elements as constraint conditions as part of the substructure synthesis method to find the modal variable, stress, and strain of the structure (Choi et al., 1989).

MASTA 12.1 was used for the rotor-vibration modeling of the yaw system gear train, and then the ANSYS 22 finite element models of the housing and carriers were connected through the substructure synthesis method. Fig. 2 shows the finite element model of the housing that was produced using ANSYS 22. Because the teeth of the ring gear were included in the MASTA 12.1 vibration model, they were excluded from the finite element model. If the mesh quality of a finite element model is poor when synthesizing it with the gear train model using MASTA 12.1, a matrix cannot be formed and an error occurs. Accordingly, the bolt holes of the ring gear, flange, and output housing were deleted when forming the mesh in order to improve the mesh quality. The finite element model consisted of 191,948 nodes and 744,424 elements.

Fig. 3 shows the part where the gear train and housing node are connected. The output axis bearing of the gear train is in contact with

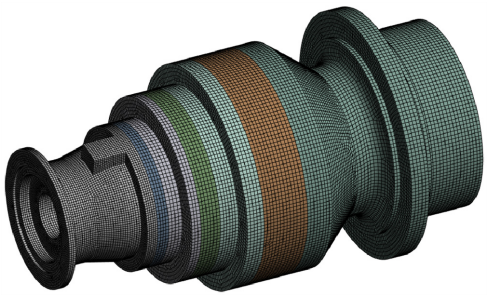

Fig. 2 Finite element model of housing

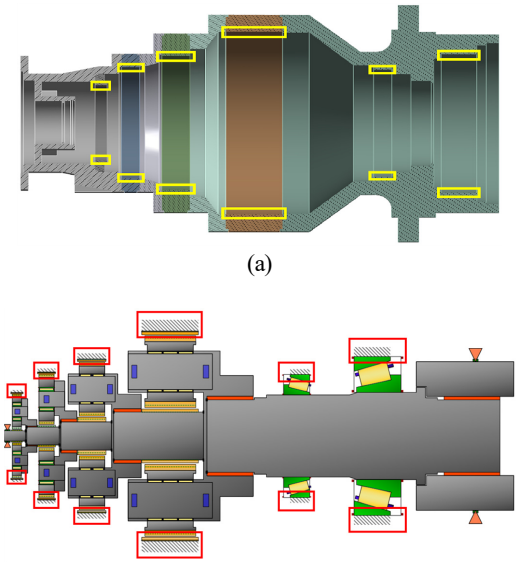

Fig. 3 Housing and gear train connection parts: (a) housing connection part and (b) gear train connection part

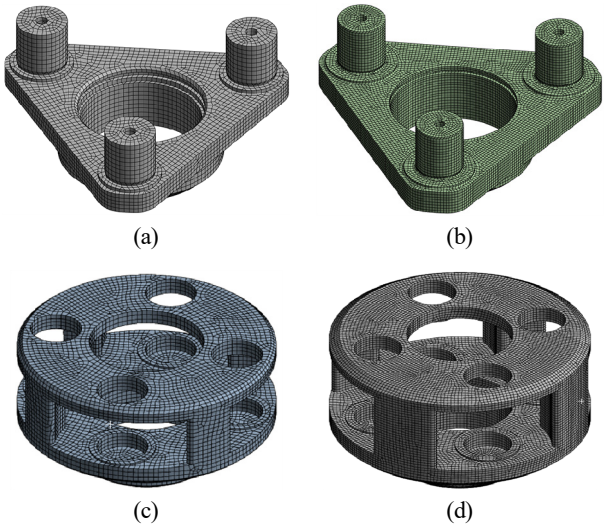

Fig. 4 Carrier finite element models: (a) 1st carrier, (b) 2nd carrier, (c) 3rd carrier, and (d) 4th carrier

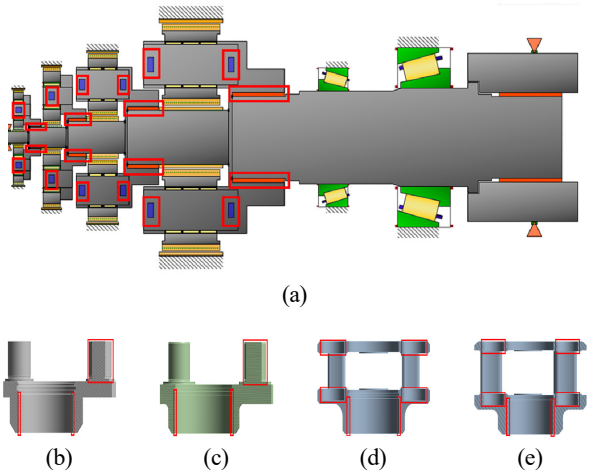

Fig. 5 Carrier and gear-train connection parts: (a) gear train, (b) 1st carrier, (c) 2nd carrier, (d) 3rd carrier, and (e) 4th carrier

the output housing, and the ring gear of each stage is connected with the ring gear of the housing.

Fig. 4 shows the finite element models of the carriers devised to be synthesized with the gear train model. The finite element model of the first carrier has 82,866 nodes and 23,228 elements, that of the second carrier has 253,896 nodes and 69,742 elements, that of the third carrier has 159,828 nodes and 46,432 elements, and that of the fourth carrier has 597,403 nodes and 163,068 elements.

Fig. 5 shows the part where the gear train and carriers are connected. The substructure synthesis of the carriers involves connecting each carrier with the node of the part contacting the planetary pin, and connecting the node of the spline at which the carrier is connected to the subsequent stage.

Fig. 6(a) shows the vibration model when only the gear train is considered, without considering the finite element models of the housing and carriers. Fig. 6(b) shows the vibration model when the

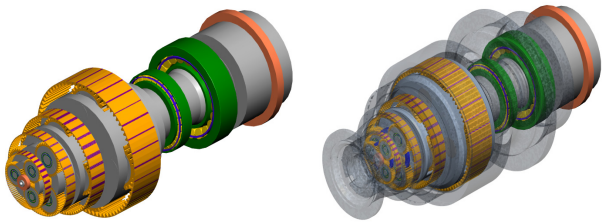

(a) (b)

Fig. 6 Natural frequency comparison models: (a) vibration model without finite element mode and (b) vibration modeling with infinite element mode

Table 5 Comparison of natural frequency analysis results

Mode	Natural frequency (Hz)	
	without finite element model	with finite element model
1	100.76	104.83
2	105.88	108.29
3	275.08	184.57
4	292.33	203.04
5	296.21	233.14
6	411.91	313.96

finite element models of the housing and carriers are synthesized with the planetary gear train using the substructure synthesis method. Table 5 presents a comparison of the natural frequencies in cases where the finite element models of the housing and carriers were and were not taken into consideration, under the condition that the torque was the largest among the load duration distribution (LDD) data. The natural frequency of the case where the finite element models of the housing and carriers were taken into consideration was lower than that where they were not taken into consideration.

3. Vibration Excitation Source Modeling and Critical Speed Analysis of the Yaw System

3.1 Modeling of the Vibration Excitation Source

The excitation sources applied to the yaw system included the mass imbalance, gear mesh frequency, and errors in the bearing installation. The gear mesh frequency is primarily caused by gear-teeth machining errors and system deformation due to loads, and is expressed as the product of the rotational speed and number of gear teeth. Mass imbalance occurs when there is an eccentric mass caused by machining errors, and is identical to the rotational speed. The types of excitation frequencies due to rolling-bearing defects include the fundamental train frequency (FTF), ball spin frequency (BS), outer racer frequency (OR), and inner racer frequency (IR) (Lee, 1999).

Table 6 presents the bearing characteristics of each stage, while Table 7 presents the excitation frequency ratio considering the mass imbalance and gear mesh frequency of the yaw system. Here, 1X indicates the changes in the rotational speed input in the first sun gear. The excitation sources related to bearing defects are listed in Table 8.

Table 6 Rolling bearing information

Stage	1	2	3	4	Ouput left	Output right
Number of ball	15	19	26	30	31	21
Pitch diameter	29	39	54	74	200.328	239.942
Ball diameter	4	4	4	4	19.153	34.335
Contact angle	0	0	0	0	17	16.1722

Table 7 Excitation frequency of mass imbalance and gear mesh frequency

Excictation source	Excitation frequency ratio		
		Sun	Planetary
Mass imbalance	Stage 1	1X	0.13X
	Stage 2	0.13X	0.019X
	Stage 3	0.019X	0.004X
	Stage 4	0.004X	0.001X
Gear mesh frequency	Stage 1	14X	
	Stage 2	2.204X	
	Stage 3	0.406X	
	Stage 4	0.082X	

Table 8 Excitation frequency ratio of bearing

Stage	1	2	3	4	Ouput left	Output right
FTF	1.073X	0.166X	0.034X	0.007X	0.008X	0.009X
BS	8.857X	1.791X	0.503X	0.145X	0.082X	0.054X
OR	16.104X	3.166X	0.902X	0.223X	0.25X	0.187X
IR	21.257X	3.89X	1.047X	0.249X	0.237X	0.144
rps	2.49	0.37	0.075	0.015	0.002	0.015

3.2 Critical Speed Analysis

Vibration and noise occur in the yaw system of a wind turbine when the excitation frequency and natural frequency of the yaw system are identical. If the excitation frequency is γ_i, where $i = 1, 2, 3, \cdots, N$, and the natural frequency of the yaw system is λ_i, where $i = 1, 2, 3, \cdots, N$, resonance occurs when $\gamma_i = \lambda_i$. If the excitation frequency is $\gamma_i = c_i \omega_{cr}$, critical speed ω_{cr} becomes $\omega_{cr} = \lambda_i / c_i$. Here, c_i is the coefficient of the excitation frequency (Kim et al., 2011).

The input speed of the yaw system was 1,158.96 rpm; Tables 6 and 8 present the excitation sources with respect to changes in the input speed. Figs. 7 and 8 show Campbell diagrams of the mass imbalance, gear mesh frequency, and bearing defects (FTF, BS, OR, IR).

Figs. 7–14 show that the critical speed of the mass imbalance, gear mesh frequency, and bearing defects did not occur within the operation speed (1,158.96 rpm) range.

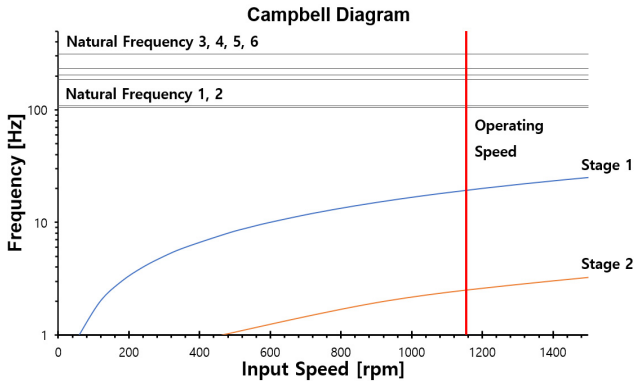

Fig. 7 Campbell diagram of mass unbalance

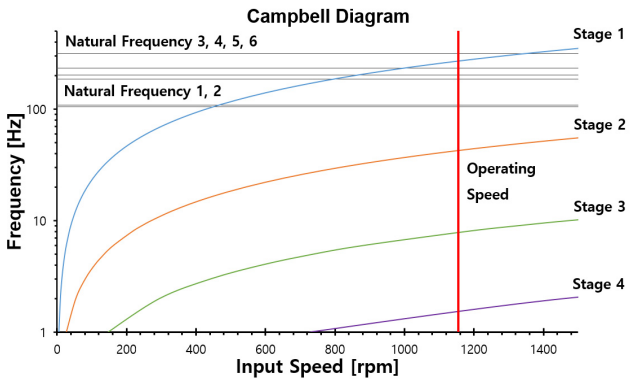

Fig. 8 Campbell diagram of gear mesh frequency

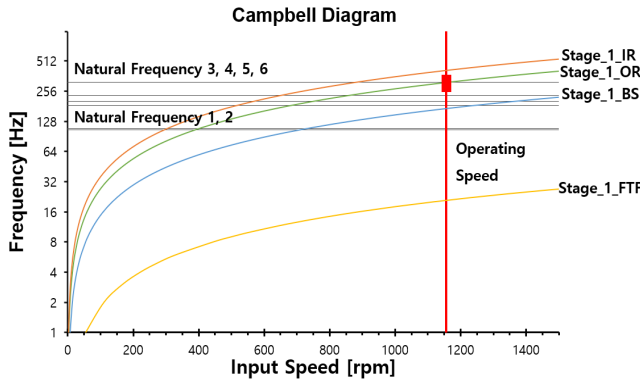

Fig. 9 Campbell diagram of stage 1 bearing

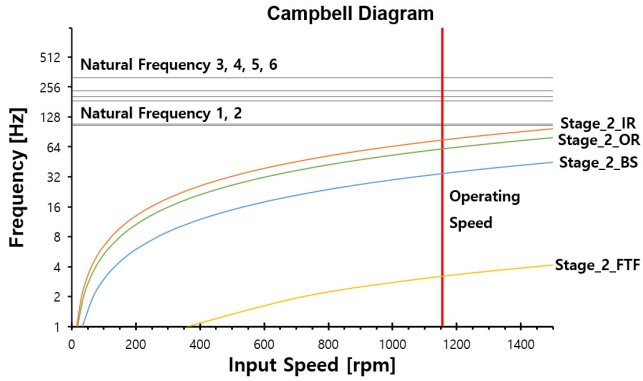

Fig. 10 Campbell diagram of stage 2 bearing

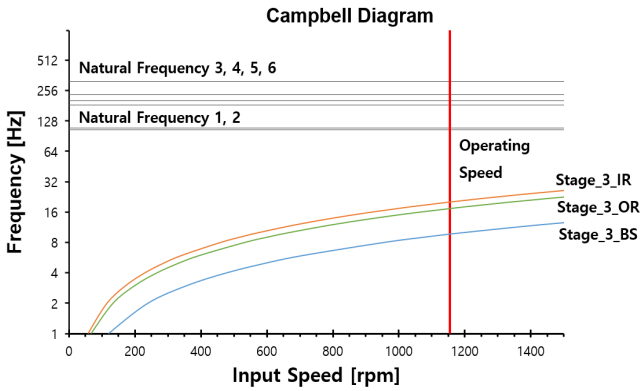

Fig. 11 Campbell diagram of stage 3 bearing

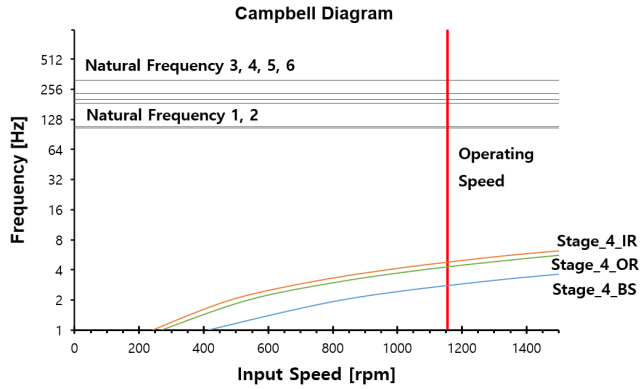

Fig. 12 Campbell diagram of stage 4 bearing

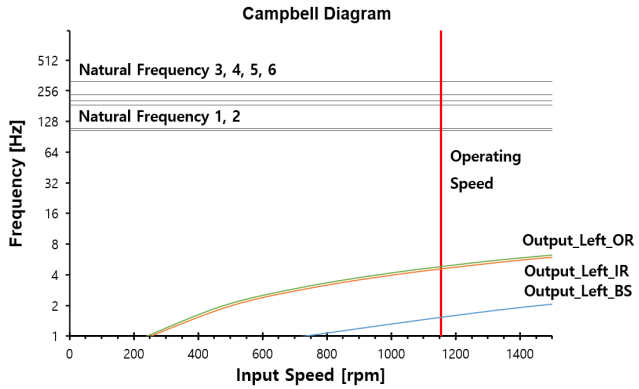

Fig. 13 Campbell diagram of output left bearing

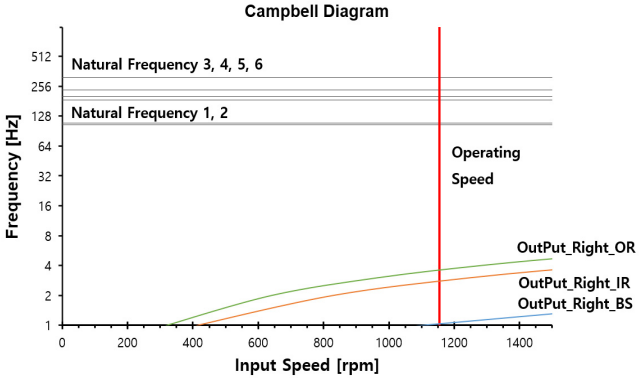

Fig. 14 Campbell diagram of output right bearing

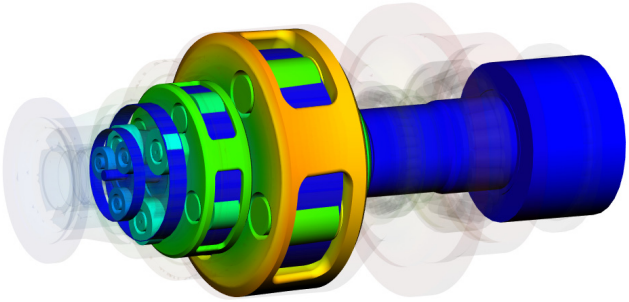

Fig. 15 Mode shape of mode 6

Fig. 9 presents the Campbell diagram of the stage 1 planetary gear, where the bearing outer ring of the first planetary gear coincides with the natural frequency of mode 6, as listed in Table 6; the mode shape of the sixth natural frequency is illustrated in Fig. 15. According to the mode shape results, a large vibration mode occurred in the vertical direction of the first planetary gear, which indicated that the bearing condition of the first planetary gear requires regular inspections.

4. Natural Frequency Characteristic Analysis with Respect to Changes in the LDD

The mathematical model of the vibration system of a wind turbine yaw system can be expressed as shown in Eq. (1).

$$[M]\ddot{q}+[C]\dot{q}+[K]q=0 \tag{1}$$

$$\{q\} = \begin{Bmatrix} x \\ y \\ z \\ \theta_x \\ \theta_y \\ \theta_z \end{Bmatrix} \tag{2}$$

Here, $[M]$ is the system mass matrix, $[C]$ is the system damping matrix, $[K]$ is the system stiffness matrix, and q is the system response (Min et al., 2015).

Eq. (2) expresses the torsion, rotational, and bending direction vectors, along with the three displacement vectors of x, y, and z.

A general industrial gear box receives a fairly constant load. The vibration analysis of a wind turbine must consider various types of LDDs. The rolling bearing stiffness of a wind turbine gear box varies depending on the applied torque; thus, further research is needed on the effects of changes in the LDD on the first natural frequency.

Because there is a lack of research on the changes in the characteristics of the natural frequency with respect to changes in the LDD, this system found the natural frequency of the yaw system in terms of changes in the LDD.

Figs. 16 and 17 illustrate the changes in the natural frequency with respect to the bearing stiffness when the largest load (116,320 Nm) of the LDD was considered to be one, and the load was increased in 10% increments from 10% of the largest load to 100%.

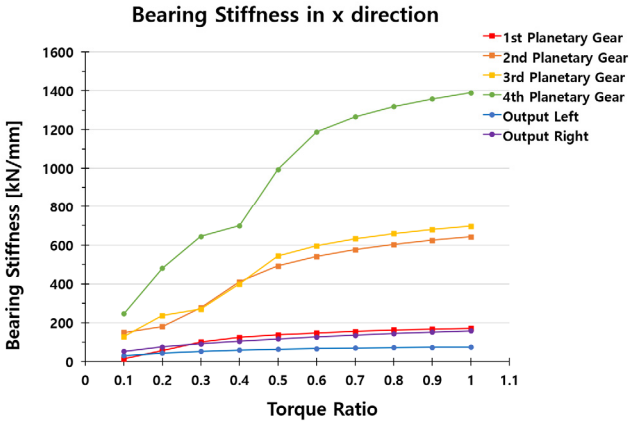

Fig. 16 Variation of bearing stiffness in x-direction according to load

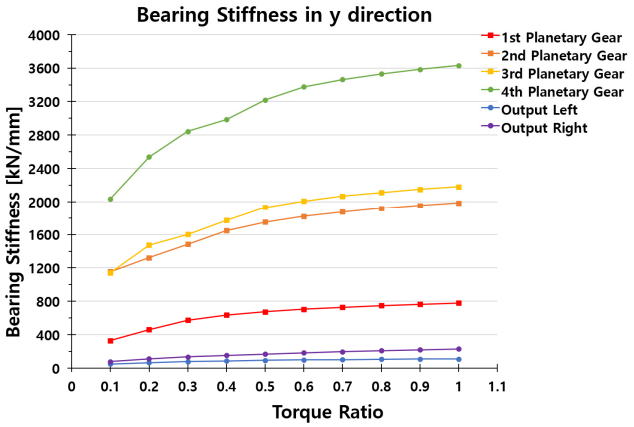

Fig. 17 Variation of bearing stiffness in y-direction according to load

Table 9 Changes in x-direction bearing stiffness according to load

Torque (Nm)	1	2	3	4	Ouput left	Output right
11,632	14.8	149.5	129.5	247.2	31.4	53.2
23,264	56.6	180.4	237.1	480.2	44.5	75.7
34,896	101.6	277.1	270.2	643.6	53.5	91.9
46,528	124.1	411.2	399.6	698.9	59.9	105
58,160	137.9	492	543.2	994.2	64	116.3
69,792	148	541	596	1187.6	67.4	126.4
81,424	155.8	575.8	641.6	1266	70.3	135.5
93,056	163.2	602.6	658.4	1318.9	72.5	143.9
104,688	167.5	624.3	679.4	1358.6	74	151.7
116,320	172.0	642.1	696.6	1389.6	75.3	159

Fig. 16 shows the stiffness variation in the x-direction of a bearing in each stage according to changes in the load. The stiffness in the x-direction varied significantly with respect to the load.

Fig. 17 shows the stiffness variation in the y-direction of a bearing in each stage according to changes in the load. The stiffness in the

Table 10 Changes in y-direction bearing stiffness according to load

Torque (Nm)	1	2	3	4	Ouput left	Output right
11,632	328.2	1154.8	1141.4	2036.3	48.6	78.6
23,264	459.4	1322.7	1473.8	2537	64.5	110.3
34,896	573.9	1483.2	1602.9	2844.4	77	133.1
46,528	634.7	1647.4	1770.8	2985.7	86.2	151.7
58,160	674.5	1751.6	1930.3	3218	92.4	167.9
69,792	704.7	1821.5	2008	3376.3	97.5	182.3
81,424	728.6	1874.9	2066.4	3462.8	101.8	195.3
93,056	748.2	1918.1	2112.2	3529.2	105.1	207.2
104,688	764.7	1954.6	2149.5	3583.9	107.5	218.5
116,320	779	1985.6	2180.9	3630.3	109.4	228.9

y-direction also varied significantly with respect to the load. The detailed numerical values shown in Figs. 16 and 17 are presented in Table 9 and Table 10, respectively.

Fig. 18 shows the variations in the first natural frequency with respect to the load. Because the lowest first natural frequency was 72.186 Hz, exceeding the operation speed of 1,158.96 rpm (19.316 Hz), all the LDD data were safely within the range of the operation speed. The detailed numerical values shown in Fig. 18 are presented in Table 11.

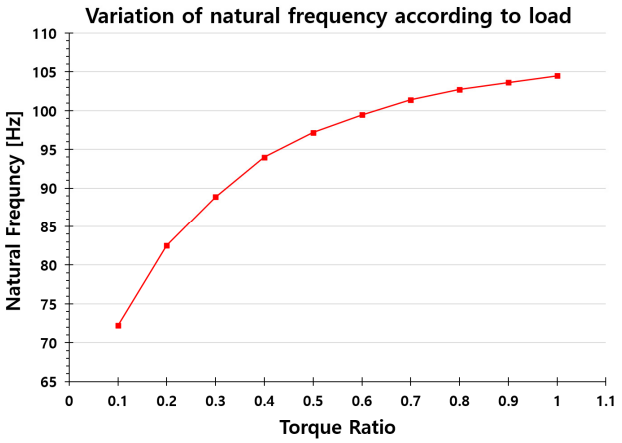

Fig. 18 Variation of natural frequency according to load

Table 11 Changes in natural frequency according to load

Torque (Nm)	Natural frequency (Hz)
11,632	72.1
23,264	82.5
34,896	88.8
46,528	93.9
58,160	97.1
69,792	99.4
81,424	101.3
93,056	102.7
104,688	103.6
116,320	104.4

5. Conclusion

This study investigated a method for combining finite element models of the housing and carriers with the rotor vibration model of a planetary gear train through substructure synthesis and analyzing the vibration of the yaw system with respect to variations in the LDD.

When the natural frequencies were compared for cases where the finite elements of the housing and carriers were and were not considered, the natural frequency was lower in the case where the finite element models were taken into consideration. In addition, the critical speed of the yaw system was analyzed by modeling the vibration excitation sources for the mass imbalance, gear mesh frequency, and bearing defect frequency applied to the yaw system, and the results demonstrated that the critical speed of the mass imbalance and gear mesh frequency did not occur within the operation-speed range. However, the bearing condition must be inspected periodically because the outer ring of the first planetary gear bearing coincided with the sixth natural frequency (313.96 Hz) in the critical speed analysis of the bearing installation error.

When the LDD was increased in 10% increments from 10% of the largest load to 100%, both the bearing stiffness and first natural frequency increased with the LDD. Furthermore, the first natural frequency was 72.186 Hz for the lowest LDD, which exceeded the operation speed of 1,158.96 rpm (19.316 Hz); thus, according to the changes in the LDD, the vibration did not occur within the operation-speed range. Because the rolling bearing stiffness varied with the LDD, further analysis of the vibration of a wind turbine must be performed while considering the LDD.

Conflict of Interest

Seok-Hwan Ahn serves as an editorial board member of the Journal of Ocean Engineering and Technology, but he had no role in the decision to publish this article. No potential conflict of interest relevant to this article was reported.

Funding

This thesis is research of a study conducted with the support of the ‘Renewable Energy Core Technology Development Project’ supported by the Korea Energy Technology Evaluation and Planning. (No. 20213030020020)

References

Bossanyi, E. A. (2005). Further load reductions with individual pitch control. *Wind Energy, 8*(4), 481–485. https://doi.org/10.1002/

we.166

Choi, J. W., Lee, S. S., & Park. Y. S. (1989). A review of mode synthesis techniques and its application between FE and experimental Model. *Transactions of the Korean Society of Mechanical Engineers, 13*, 799−806. https://doi.org/10.22634/KSME.1989.13.4.799

Choy, F. K., Tu, Y. K., Savage, M., & Townsend, D. P. (1991). Vibration signature and modal analysis of multi-stage gear transmission. *Journal of the Franklin Institute, 328*(2), 281−298. https://doi.org/10.1016/0016-0032(91)90035-2

Dong, H., Zhang, K., Wang, D., Wu, Y., & Bai, S. (2015). Dynamic modeling of planetary gear train for vibration characteristic analysis. *Mechanisms Trasmissions and Application, 31*, 187−195. https://doi.org/10.1007/978-3-319-17067-1_20

Hong, H. S., Park, J. I., Bang, J. H., Ryu, J. Y., & Kim, D. H. (2006). Research for 2MW wind turbine tower shell design optimization. *The Korean Society for New and Renewable Energy, 2*(4), 19−26.

Iida, H., Tamura, T., Kikuchi, K., & Agata, H. (1980). Coupled torsional-flexural vibration of a shaft in a geared system of rotors. *Bulletin of JSME, 23*(186), 2111−2117. https://doi.org/10.1299/jsme1958.23.2111

Itoh, T. (1973). Damped vibration mode superposition method for dynamic response anaylsis. *Earthquake Engineering Structural Dynamics, 2*(1), 47−57. https://doi.org/10.1002/eqe.4290020105

Kahraman, A., Ozguven, H. N., Houser, D. R., & Zakrajsek, J. J. (1992). Dynamic analysis of geared rotors by finite elements. *Journal of Mechanical Design, 114*(3), 507−514. https://doi.org/10.1115/1.2926579

Kim, J. S., Lee. H. W., Park, N. G., Kim, Y. D., Kim, S. Y., & Lee, D. H. (2011). Characteristic of vibration in wind turbine system. *Journal of the Korean Society of Marine Engineering, 35*(6), 786−795. https://doi.org/10.5916/jkosme.2011.35.6.786

Lee, H. Y. (1999). *An analytical investigation on vibrational characteristics of multi-mesh geared system using transfer aatrix method* [Master's thesis, Busan University].

Lee, H. Y., & Kang, D. K. (2014). Gear teeth modification for a 2.5MW wind turbine gearbox. *Journal of the Korean Society of Manufacturing Technology Engineers, 23*(2), 109−117. https://doi.org/10.7735/ksmte.2014.23.2.109

Min, Y. S., & Lee, H. W. (2015). A study on the design of cycloidal pitch reducer for the 2MW-class wind turbine. *Journal of the Korean Society of Marine Engineering, 39*(9), 895−902. https://doi.org/10.5916/jkosme.2015.39.9.895

Parker, R. G., Agashe, V., & Vijayakar, S. M. (2000). Dynamic response of a planetary gear system using a finite element/contact mechanics model. *Journal of Mechanical Design, 122*(3), 304−310. https://doi.org/10.1115/1.1286189

Prohl, M. A. (1945). A general method for calculating critical speeds of flexible rotors. *Journal of Applied Mechanics, 12*(3), 142−148. https://doi.org/10.1115/1.4009455

Tanata, M. (1984). Matrix methods in planetary gear train analyses. *Society of Automotive Engineers, 93*(5), 333−340. https://www.jstor.org/stable/44721481

Wang, S. M., & Morse. JR. I. E. (1972). Torsional response of a gear train system. *Manfacturing Science and Engineering, 94*(2), 583−592. https://doi.org/10.1115/1.3428200

Author ORCIDs

Author name	ORCID
Lee, HyoungWoo	0000-0002-7312-6910
Jang, SeoWon	0009-0000-7042-9644
Ahn, Seok-Hwan	0000-0002-9598-9995

KSOE

Technical Article

Journal of Ocean Engineering and Technology 37(4), 172-179, August, 2023
https://doi.org/10.26748/KSOE.2023.020

pISSN 1225-0767
eISSN 2287-6715

An Experimental Study of Non-Electrolysis Anti-Microfouling Technology Based on Bioelectric Effect

Young Wook Kim

Director of PAIST, ProxiHealthcare Inc., Seoul, Korea

KEYWORDS: Biofilms, Bioelectric Effect, Electrolysis, Biofouling, Antimicrofouling

ABSTRACT: *Biofouling initiated by biofilm (slime) formation is a key challenge for practical ocean engineering and construction. This study evaluated a new anti-biofilm technology using bioelectricity. The anti-microfouling electrical technology is based on the principles of the bioelectric effect, known as the application of an electrostatic force for biofilm removal. Previously, the electricity was optimized below 0.82V to avoid electrolysis, which can prevent the production of biocides. A test boat comprised of microelectronics for electrical signal generation with electrodes for an anti-biofouling effect was developed. The tests were conducted in the West Sea of Korea (Wangsan Marina, Incheon) for three weeks. The surface biofouling was quantified. A significant reduction of fouling was observed under the bioelectric effect conditions, with approximately 30% enhanced prevention of fouling progress ($P<0.05$). This technology can be an alternative eco-friendly technique for anti-microfouling that can be applied for canals, vessels, and coastal infrastructure because it does not induce electrolysis.*

1. Introduction

The ocean covers 70% of the Earth's surface, with approximately two billion vessels worldwide (Czermański et al., 2022). Marine organisms in the ocean occupy approximately 70% of total biomass (Bar-On et al., 2018). The organisms are viruses, bacteria, archaea, protists, microfungi, and microanimals (Hutchins, 2017). In nature, these organisms attach, grow, and proliferate on the surface or host (Palmer et al., 2007). Once they reach specific populations, they communicate to produce an extracellular matrix to protect them from external stimuli. Biofilms (Flemming and Wuertz, 2019) of multispecies of microorganisms accumulate on any surface, either hydrophilic or hydrophobic, and are established within two weeks. Thus, two billion vessels have biofilms on the surface and travel worldwide. The biofilms on the vessel increase fluidic friction, resulting in a reduction of fuel efficiency that contributes to the greenhouse effect on the earth (Cámara et al., 2022). Therefore, the effective management of biofilms is critical.

Biofilms are the initiative layer for biofouling (Beech, 2004). Various organisms, such as Algae, plants, and small animals (barnacles), attach to the biofilm and build their structure, which usually takes one or two months, depending on the environmental conditions (temperature, salt, and flow velocity). Once biofouling occurs, it requires significant physical brushing and often strong chemical treatments for cleaning (Yebra et al., 2004). The anti-biofouling market is 110 billion USD, including the reduced fuel efficiency caused by biofouling (Isla et al., 2012). Furthermore, biofouling has a global economic impact, including 23 billion USD for antifouling marine coatings to reduce the density and weight of biofilms. The marine environment also transfers invasive species worldwide, leading to significant socioeconomic impacts on fisheries, mariculture, and coastal infrastructure (Molnar et al., 2008); the estimated cost is 4–8 billion USD annually (Fitridge et al., 2012).

Current anti-microfouling technology is focused on surface engineering (Yang et al., 2011), including developing materials for surface coating and high electric current technologies based on the electrolysis of microorganisms (Xue et al., 2015). Developing a biosafe anti-microfouling technology is required because the painting material and induction of electrolysis can generate toxic biocides (Amara et al., 2018). Ultrasound and microbubble-generating technology have also been applied (Park et al., 2017). On the other hand, the technology has limitations in preventing microfouling and generating acoustic noise for marine operations. In general, developing a new solution for antifouling is an urgent challenge for industry and academia.

Our group has been dedicated to preventing biofilms for anti-

Received 23 June 2023, revised 9 August 2023, accepted 14 August 2023
Corresponding author Young Wook Kim: +82-2-713-9153, ywkim@proxihealthcare.com

microfouling processes instead of cleaning approaches. An electrostatic force, the Van der Waals force, was used for biofilm inhibition based on the principles of the bioelectric effect (BE) (Freebairn et al., 2013).

An external electric force can interrupt the biofilms and attached surfaces because biofilms are soluble and electrically charged materials.

This study examined the bioelectric effect in previous work and showed that a specific signal frequency is effective in biofilm treatment (Kim et al., 2015; Subramanian et al., 2020). This technology uses non-electrolysis-induced electrical power, preventing toxic biocides production. The proposed strategy is focused on preventing biofilm formation to control bulk biofouling (Fig. 1).

This study focused on demonstrating the electrical technology in real ocean conditions, which are not the same as the standard bacterial growth media, including the concentration of salt and composition of microorganisms. This study developed a non-electrolysis-induced electrical anti-microfouling system. A testing boat comprised of floating parts, electronics, and biofouling monitoring was fabricated. During the test in the West Sea of Korea (Wangsan Marina, Incheon, Korea) for three weeks, the bulk biofouling was monitored using a smartphone, and the surface coverage was quantified using standard software. The results revealed the significant prevention of biofouling.

2. Materials and Methods

2.1 Principles of Biofilm Inhibition (Bioelectric Effect)

An external electric force can inhibit the surface attachment of biofilms through the principle known as the “bioelectric effect” (BE). An alternating current can increase the permeability of the biofilms, resulting in a weak structure susceptible to external stimuli (Kim et al. 2016), and a direct current provides a static force that results in detachment (Del Pozo et al., 2008). The present system utilized an alternative and direct current to maximize the biofilm prevention efficacy. Based on previous work, it is characterized by a 0.7V amplitude of a sinusoidal signal at 10 MHz with a 0.7V offset voltage (Kim et al., 2015; Huiszoon et al. 2019) (Table 1). This signal does not induce electrolysis (Kim et al., 2015).

2.2 Electrical System for Testing Setup

Electrical signal generation was realized using a crystal oscillator with a microelectronic circuit design. The performance of the circuit was confirmed by electrical measurements (Fig. 2). Applications of the technology require electrode patterning on the surface. The electrode was fabricated through a traditional flexible printed circuit board (FPCB). The electrode was made of stainless steel to ensure anticorrosive properties. The distance and pitch between the electrodes were the same as in previous work (Kim et al., 2022). Table 2 provides details of the design and materials. The testing conditions were repeated on three plates at the same time. The BE was applied to the three plates for the entire testing period to investigate the efficacy of microfouling prevention. For comparison, an additional three plates have been installed in the boat without applying BE.

2.3 Fabrication of Testing Boat

Bulk biofouling initiates approximately within three weeks. A testing boat comprised of three major parts was designed and fabricated: (1) floating, (2) electrical system, and (3) biofouling monitoring parts. The floating part was a commercially available tube (maximum 20 kg weight); two tubes were installed in parallel. The electrical system is for a constant supply of the bioelectric effect during testing with a waterproof package. Finally, the biofouling monitoring part was designed to disassemble easily for a visual

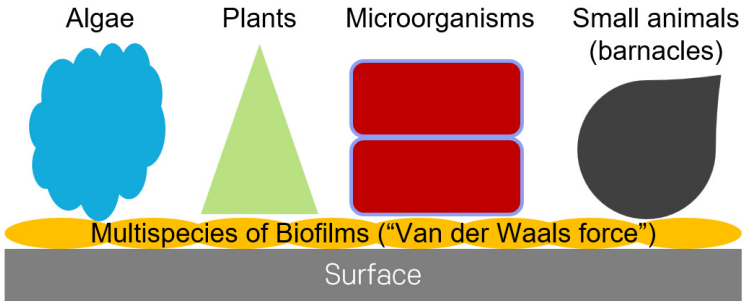

Fig. 1 Schematic diagram of biofouling, (1) attached multispecies of biofilms on surfaces (Van der Waals force), (2) marine organisms attached on the biofilms. We are focused on the inhibition of the biofilm layer.

Table 1 Details of the bioelectric effect

Contents	Details	Comments
Intensity	0.70 V	Below water electrolysis 0.82 V
Frequency	10 MHz	Effective frequency
Composition (Alternating current: Direct current)	1:1	Effective biofilm treatment

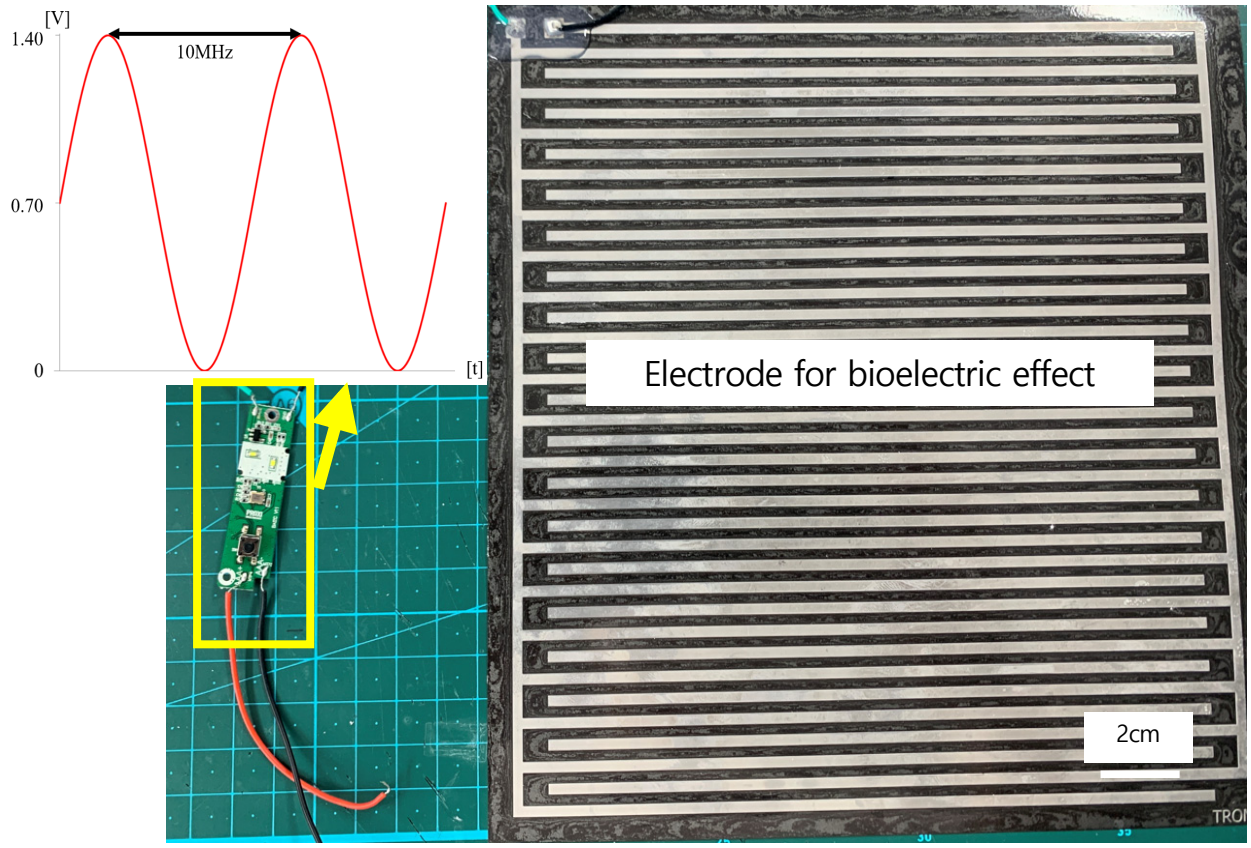

Fig. 2 Photo of the electric circuit and electrode for electric signal applications

Table 2 Details of the electrode design

Contents	Details	Comments
Width	2.5 mm	Printed circuit
Distance	5.0 mm	Electric field application
Thickness	2.0 mm	Printed circuit
Material	SUS 316L	Anticorrosive property

inspection (Fig. 3). The boat was placed in the West Sea of Korea, Incheon, from May 19th to June 9th, 2022. Considering the progress period of microfouling (Gizer et al. 2023), the surface was inspected at initial (day "0"), 8 d (day "8"), and 20 d (day "20") later.

2.4 Data Analysis

Surface coverage analysis, especially on microfouling, was performed as a rapid quantification method in ocean research (First et al., 2021). The testing period (three weeks) focused on the prevention of microfouling. The image was taken using a smartphone camera (Samsung Galaxy S22). The surface biofouling coverage was quantified by Image J 1.53 (NIH, USA) using binary image analysis.

The statistical analysis was performed using the analysis of variance (ANOVA): p-value analysis first and followed by post-hoc testing, which is a standard statistical tool for group data analysis (Bailey et al., 2008). ANOVA was performed on the bioelectric effect "ON" and "OFF" groups from the initial 8- and 20-day data groups. The statistical significance between the technology "ON" and "OFF" groups at each examination period was critical because this study focused on the technology validation.

3. Results

The results were collected three times during the experiments. A photograph of the biofouling monitoring part is summarized in Figs. 4–6. After eight days, biofouling was not significant in the bioelectric effect "ON" and "OFF" conditions, as shown by the clear electrode pattern. On the other hand, intensive biofouling was observed under the bioelectric effect "OFF," in which biomass covered the electrode pattern. When the bioelectric effect was applied, the image showed a significant reduction of biomass formation on the electrode (bioelectric effect "ON"). Thus, applying the bioelectric effect can prevent biofouling on the surface.

Quantitative analysis of the images was performed using the

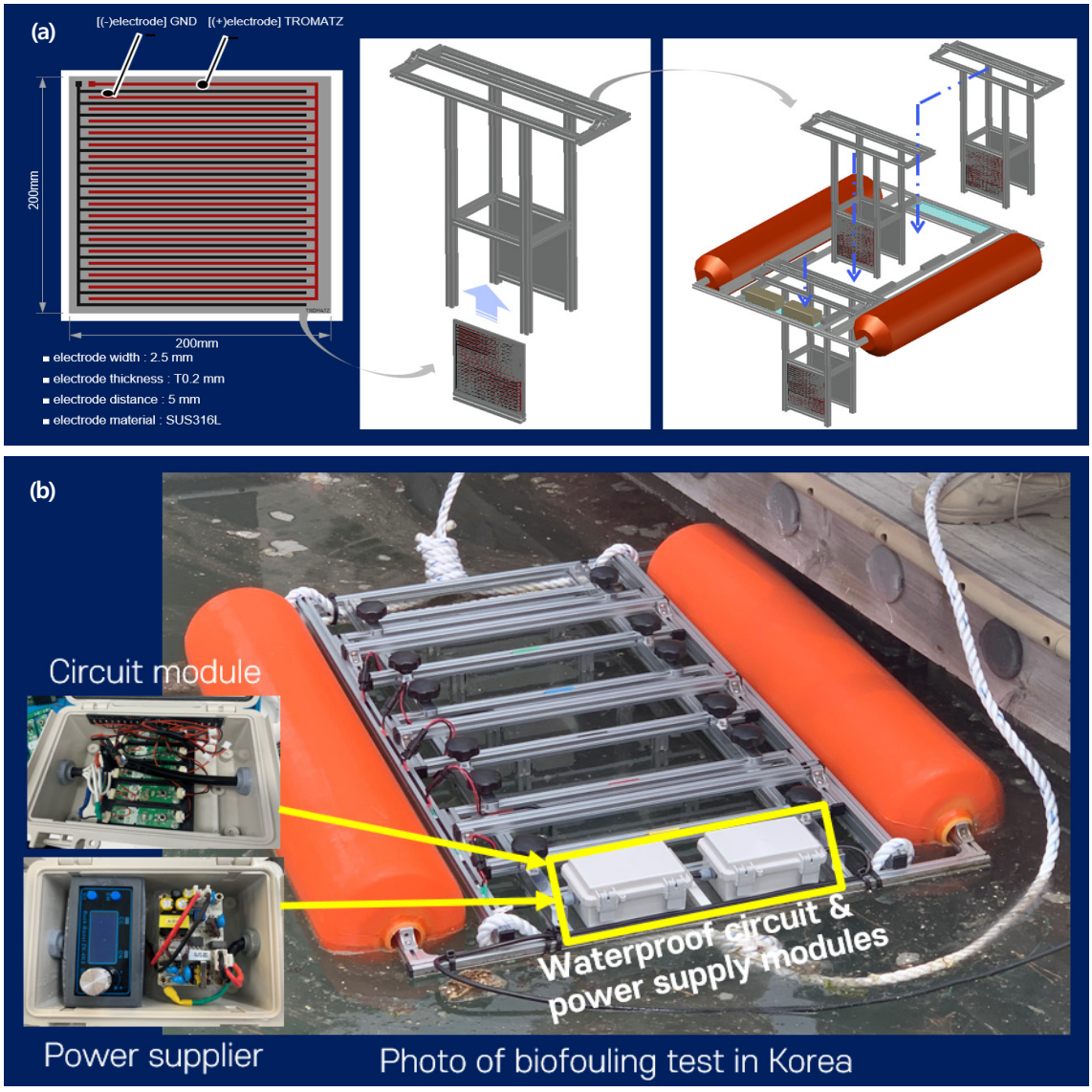

Fig. 3 Details of the testing boat: (a) Schematic of biofouling monitoring part; (b) photo of the testing boat and electrical system

Condition	Initial (Day 0)	Day 8 in the ocean	Day 20 in the ocean
Bioelectric effect "ON"		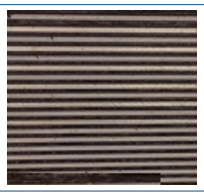	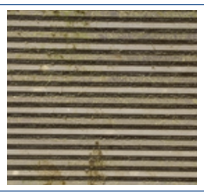
	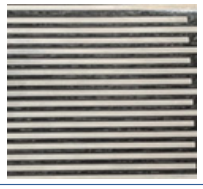		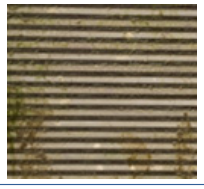
			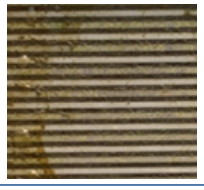

Fig. 4 Images of the biofouling part (Days 0, 8, and 20)

Condition	Initial (Day 0)	Day 8 in the ocean	Day 20 in the ocean
Bioelectric effect "OFF"	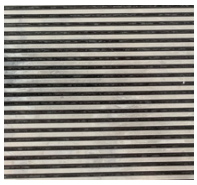		
			
		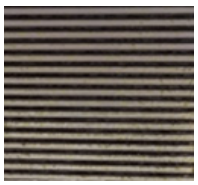	

Fig. 4 Images of the biofouling part (Days 0, 8, and 20) (Continuation)

Condition	Initial (Day"0") Bioelectric effect "OFF"	Day 20 in the ocean Bioelectric effect "ON"	Day 20 in the ocean Bioelectric effect "OFF"
Original image		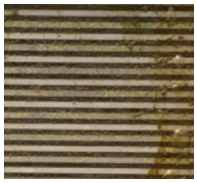	
Binary image (ImageJ 1.53)	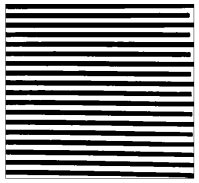	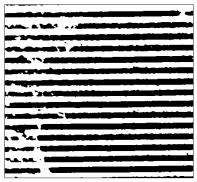	
Surface coverage (% of white area, ImageJ 1.53)	49.81	53.52	64.67

Fig. 5 Binary image conversion (Representative images)

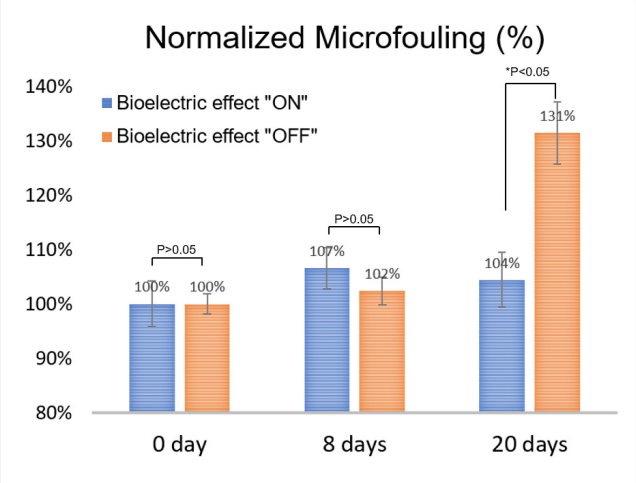

Fig. 6 Normalized microfouling in the bioelectric effect "ON" and "OFF"

standard image process software (ImageJ 1.53., NIH, USA) (Kim et al., 2015; Kim et al., 2016). The image focused on the surface coverage of the electrode (bright area compared to the dark background). The photograph was loaded on the ImageJ program and converted binary (black and white), as shown in Fig. 5. The surface coverage was quantified, focusing on the area of the black respected to the entire area. Table 3 lists the surface coverage data (binary option: iteration 1, count 1). The initial data was approximately 50% surface coverage because of the electrode portion (Fig. 5). Compared to the initial stage, the biofouling process was analyzed by normalizing the surface coverage (Table 3). The quantitative data also showed significant prevention of microfouling when the bioelectric effect was applied ($p < 0.05$, ANOVA). Therefore, the bioelectric application demonstrates the effective prevention of biofouling.

Table 3 Normalized biofouling (%) using Fig. 4, biofouling has been significantly prevented under bioelectric effect "ON" conditions compared to the initial day (Analysis of Variance: ANOVA, $p < 0.05$).

Condition	Surface coverage (%) [ImageJ 1.53, NIH, USA]			Normalization (%) respected to average (0 d)		
	0 d	8 d	20 d	0 d	8 d	20 d
Bioelectric effect "ON"	51.24	54.81	49.21	103	110	99
	47.51	53.75	53.52	95	108	107
	51.06	51.18	53.71	102	102	108
Average	49.94	53.25	52.15	100	107	104
Standard deviation	2.10	1.87	2.55	4	4	5
Bioelectric effect "OFF"	51.27	52.82	63.98	102	105	127
	49.54	50.43	69.24	99	100	138
	49.81	50.94	64.67	99	101	129
Average	50.21	51.40	65.96	100	102	131
Standard deviation	0.93	1.26	2.86	2	3	6

4. Discussion

Some local biofouling progress was observed when the bioelectric effect was applied, as shown in Figs. 4–6. In this study, the intensity of the field can be varied, especially on the corner of the electrode, because the electric field is not uniform in the biofouling monitoring part. The electric charge density of the rectangular shape is higher than the parallel electrode (Itoh and Itho, 1996). The following variables were examined to optimize the spatial electric field distribution: (1) electrode rounding at the corner, (2) electrode density (surface coverage), (3) electrode width, and (4) electrode pattern (rectangular and circular). Although this study was not optimized in electric field distribution, the results showed a significant decrease in the biofouling progress.

The bioelectric effect is based on applying an electrostatic force, Van der Waals force. Biofilms are attached to the surface using the Van der Waals force (Garrett et al., 2008). Therefore, when the same force mechanism is applied, it can induce the detachment of the biofilms. The typical thickness of biofilms is 100 μm (Kim et al. 2012) and comprises more than 700 species of bacteria and microorganisms (Clarke, 2016). Owing to the heterogeneous composition of biofilms, the electric field or force effect is considered a general method for various biofilm treatment applications, including clinical infections (Ehrlich et al., 2005) and environmental contamination management (Hu et al., 2022). For ocean applications, its efficacy will be examined further under various ocean conditions, including the changes of salt in seawater with temperature.

The bioelectric effect applied in this study was characterized as non-electrolysis-induced technology because the effective electric voltage was below 0.82V (Kim et al., 2015). This is critical, especially considering eco-friendly technology development for ocean engineering. The electrolysis creates biocidal radicals and by-products, which can be toxic to humans and marine organisms. Therefore, this technology can contribute to developing an alternative eco-friendly anti-microfouling technology for vessel and ocean engineering structure applications.

The future implementation of the technology on the vessel will require overcoming some expected challenges. First, the electrode should be patterned on the vessel surface, which is required to develop a new electrically conductive material paint to provide a bioelectric effect. The reliability of the conductive paint is critical as the vessel lifetime is expected to be over thirty years. For effective operation, a real-time monitoring system of the anti-microfouling is also required. This study is currently working on optimizing the bioelectric effect for the anti-microfouling process and designing the real-time detection of biofouling based on previous work (Kim et al., 2012). In particular, a conductive painting process will be developed to provide the microcurrent on the niche area of the vessel where surface cleaning is challenged. The electronics part is developing further with a combination of deep-learning algorithms to minimize the antifouling efficacy on various vessels and coastal infrastructures.

5. Conclusions

This paper reported a non-electrolysis-induced anti-microfouling technology that prevents biofilm formation in the ocean. The principles of biofilm prevention are known as the bioelectric effect, which uses the electric force (Van der Waals) for surface detachment. A testing system was developed, and an investigation was performed for three weeks in the West Sea of Korea. The results show that the bioelectric effect significantly inhibits biofouling, with approximately 30% more reduction than under the non-bioelectric effect. This technology can be an appropriate method for eco-friendly biofouling management owing to non-electrolysis induction. Bioelectric effect technology will be developed further for vessel and ocean engineering applications.

Conflicts of Interest

The authors declare no conflict of interest.

Funding

This research was supported by the Korea Institute of Marine Science & Technology Promotion (KIMST), funded by the Ministry of Oceans and Fisheries (2021050012).

Acknowledgments

Author thank the College of Medicine, University of Ulsan, for the technical support.

References

Amara, I., Miled, W., Slama R. B., & Ladhari, N. (2018). Antifouling processes and toxicity effects of antifouling paints on marine environment. A review. *Environ Toxicol Pharmacol, 57*, 115–130. https://doi.org/10.1016/j.etap.2017.12.001

Bailey, R. A. (2008). *Design of comparative experiments*. Cambridge University Press. ISBN 978-0-521-68357-9.

Bar-On, Y. M., Phillips, R., & Milo, R. (2018). The biomass distribution on earth. *Proceedings of the National Academy of Sciences, 115*(25), 6506–6511. https://doi.org/10.1073/pnas.1711842115

Beech, B. (2004). Corrosion of technical materials in the presence of biofilms-current understanding and state-of-the art methods of study. *International Biodeterioration & Biodegradation, 53*(3), 177–183. https://doi.org/10.1016/S0964-8305(03)00092-1

Cámara, M., Green, W., MacPhee, C. E., Rakowska, P. D., Raval, R., Richardson, M. C., Slater-Jefferies, J., Steventon, K., & Webb, J. S. (2022). Economic significance of biofilms: a multidisciplinary and cross-sectoral challenge. *npj Biofilms and Microbiomes, 8*, 42. https://doi.org/10.1038/s41522-022-00306-y

Clarke, E. (2016). Levels of selection in biofilms: multispecies biofilms are not evolutionary individuals. *Biology & Philosophy, 31*, 191–212. https://doi.org/10.1007/s10539-016-9517-3

Czermański, E., Oniszczuk-Jastrząbek, A., Spangenberg, E. F., Kozłowski, Ł., Adamowicz, M., Jankiewicz, J., & Cirella, G. T. (2022). Implementation of the energy efficiency existing ship index: An important but costly step towards ocean protection, *Marine Policy, 145*, 105259.

Del Pozo, J. L., Rouse, M. S., & Patel, R. (2008). Bioelectric Effect and Bacterial Biofilms. a Systematic Review. *The International journal of artificial organs, 31*(9), 786–795. https://doi.org/10.1177/03913988080310090

Ehrlich, G. D., Stoodley, P., Kathju, S., Zhao, Y., McLeod, B. R., Balaban, N., Hu, F. Z., Sotereanos, N. G., Costerton, J. W., Stewart, P. S., Post, J. C., & Lin, Q. (2005). Engineering approaches for the detection and control of orthopaedic biofilm infections. Clinical orthopaedics and related *research, 437*, 59–66. https://doi.org/10.1097/00003086-200508000-00011

First, M. R., Riley, S. C., Islam, K. A., Hill, V., Li, J., Zimmernan, R. C., & Drake, L. A. (2021). Rapid quantification of biofouling with an inexpensive, underwater camera and image analysis. *Management of Biological Invasions, 12*(3), 599–617. https://doi.org/10.3391/mbi.2021.12.3.06

Fitridge, I., Dempster, T., Guenther, J., & de Nys, R. (2012). The impact and control of biofouling in marine aquaculture: a review. *Biofouling, 28*, 649–669. https://doi.org/10.1080/08927014.2012.700478

Flemming, H. C., & Wuertz, S. (2019). Bacteria and archaea on Earth and their abundance in biofilms. *Nature Reviews Microbiology. 17*, 247–260. https://doi.org/10.1038/s41579-019-0158-9

Freebairn, D., Linton, D., Harkin-Jones, E., Jones, D. S., Gilmore, B. F., & Gorman, S. P. (2013). Electrical methods of controlling bacterial adhesion and biofilm on device surfaces. *Expert Review of Medical Devices, 10*(1), 85–103. https://doi.org/10.1586/erd.12.70

Garrett, R., Bhakoo, M., & Zhang, Z. (2008). Bacterial adhesion and biofilms on surfaces. *Progress in Natural Science, 18*(9), 1049–1056. https://doi.org/10.1016/j.pnsc.2008.04.001

Gizer, G., Onal, U., Ram, M., & Sahiner, N. (2023). Biofouling and mitigation methods: A review, *Biointerface Research in Applied Chemistry, 13*(2), 185. https://doi.org/10.33263/BRIAC132.185

Hu, Y., Han, X., Shi, L., & Cao, B. (2022). Electrochemically active biofilm-enabled biosensors: Current status and opportunities for biofilm engineering. *Electrochim Acta*, *428*, 140917. https://doi.org/10.1016/j.electacta.2022.140917

Huiszoon, R. C., Subramanian, S., Rajasekaran, P. R., Beardslee, L. A., Bentley, W. E., & Ghodssi, R. (2019). Flexible platform for in situ impedimetric detection and bioelectric effect treatment of escherichia coli biofilms. *IEEE Transactions on Biomedical Engineering. 66*(5), 1337–1345. https://doi.org/10.1109/TBME.2018.2872896.

Hutchins, D., & Fu, F. (2017). Microorganisms and ocean global change. *Nature Microbiology, 2*, 17058. https://doi.org/10.1038/nmicrobiol.2017.58

Isla, F., Tim, D., Jana, G., & Rocky, N. (2012). The impact and control of biofouling in marine aquaculture: a review. *Biofouling, 28*(7), 649–669. https://doi.org/10.1080/08927014.2012.700478

Itoh, K., & Itoh, S. I. (1996). The role of the electric field in confinement. *Plasma Physics and Controlled Fusion*, 38(1), https://doi.org/10.1088/0741-3335/38/1/001

Kim, Y. W., Sardari, S. E., Meyer, M. T., Iliadis, A. A., Wu, H. C., Bentley, W. E., & Ghodssi, R. (2012). An ALD aluminum oxide passivated surface acoustic wave sensor for early biofilm detection, *Sensors and Actuators B: Chemical, 163*(1), 136–145. https://doi.org/10.1016/j.snb.2012.01.021

Kim, Y. W., Subramanian, S., Gerasopoulos, K., Ben-Yoav, H., Wu, H. C., Quan, D., Carter, K., Meyer, M. T., Bentley, W. E., & Ghodssi, R. (2015). Effect of electrical energy on the efficacy of biofilm treatment using the bioelectric effect. *npj Biofilms Microbiomes. 1*, 15016. https://doi.org/10.1038/npjbiofilms.2015.16

Kim, Y. W., Meyer, M. T., Berkovich, A., Subramanian, S., Iliadis, A. A., Bentley, W. E., & Ghodssi, R. (2016). A surface acoustic wave biofilm sensor integrated with a treatment method based on the bioelectric effect. *Sensors and Actuators A: Physical* 238, 140–149.

Kim, Y. W., Lee, J., Lee, T. H., & Lim, S. (2022). Bioelectric effect utilized a healthcare device for effective management of dental biofilms and gingivitis. *Medical Engineering & Physics, 104*, 103804. https://doi.org/10.1016/j.medengphy.2022.103804

Molnar, J. L., Gamboa, R. L., Revenga, C., & Spalding, M. D. (2008). Assessing the global threat of invasive species to marine biodiversity. *Frontiers in Ecology and the Environment, 6*(9), 485–492. https://doi.org/10.1890/070064

Palmer, J., Flint, S., & Brooks, J. (2007). Bacterial cell attachment, the beginning of a biofilm. *Journal of Industrial Microbiology and Biotechnology, 34*(9), 577–588. https://doi.org/10.1007/s10295-007-0234-4

Park, J.- S., & Lee, J.- H. (2018). Sea-trial verification of ultrasonic antifouling control. *Biofouling. 34*(1), 98–110. https://doi.org/10.1080/08927014.2017.1409347

Subramanian, S., Huiszoon, R. C., Chu, S. W., Bentley, W. E., & Ghodssi, R. (2020). Microsystems for biofilm characterization and sensing – A review. *Biofilm,* 2, 100015. https://doi.org/10.1016/j.bioflm.2019.100015

Xue, Y., Zhao, J., Qiu, R., Zheng, J., Lin, C., Ma, B., & Wang, P. (2015). In situ glass antifouling using Pt nanoparticle coating for periodic electrolysis of seawater. Applied Surface Science, *357*(A), 60–68. https://doi.org/10.1016/j.apsusc.2015.08.232

Yang, Y. F., Wan, L. S., Xu, Z. K. (2011). Surface engineering of microporous polypropylene membrane for antifouling: A mini-review. Journal of Adhesion Science and Technology, *25*(1–3), 245–260. https://doi.org/10.1163/016942410X520835

Yebra, D. M., Kiil, S., & Dam-Johansen, K. (2004). Antifouling technology—past, present and future steps towards efficient and environmentally friendly antifouling coatings. *Progress in Organic Coatings, 50*(2), 75–104. https://doi.org/10.1016/j.porgcoat.2003.06.001

Author ORCID

Author name	ORCID
Kim, Young Wook	0000-0003-2071-4054

Instructions for Authors

General information

To submit a manuscript to the Journal of Ocean Engineering and Technology (JOET), it is advised to first carefully read the aims and the scope section of this journal, as it provides information on the editorial policy and the category of papers it accepts. Unlike many regular journals, JOET usually has no lag in acceptance of a manuscript and its publication. Authors that find a match with the aims and the scope of JOET are encouraged to submit as we publish works from all over the world. JOET adheres completely to guidelines and best practices published by professional organizations, including Principles of Transparency and Best Practice in Scholarly Publishing (joint statement by COPE, DOAJ, WAME, and OASPA (http://doaj.org/bestpractice) if otherwise not described below. As such, JOET would like to keep the principles and policies of those professional organizations during editing and the publication process.

Research and publication ethics

Details on publication ethics are found in http://joet.org/authors/ethics.php. For the policies on research and publication ethics not stated in the Instructions, Guidelines on Good Publication (http://publicationethics.org/) can be applied.

Requirement for membership

One of the authors who submits a paper or papers should be member of the Korean Society of Ocean Engineers (KSOE), except a case that editorial board provides special admission of submission.

Publication type

Article types include scholarly monographs (original research articles), technical articles (technical reports and data), and review articles. The paper should have not been submitted to other academic journal. When part or whole of a manuscript was already published to conference papers, research reports, and dissertations, then the corresponding author should note it clearly in the manuscript.

Copyright

After published to JOET, the copyright of manuscripts should belong to KSOE. A transfer of copyright (publishing agreement) form can be found in submission website (http://www.joet.org).

Manuscript submission

Manuscript should be submitted through the on-line submission website (http://www.joet.org). The date that manuscript was received through on-line website is the official date of receipt. Other correspondences can be sent by an email to the Editor in Chief or secretariat. The manuscript must be accompanied by a signed statement that it has been neither published nor currently submitted for publication elsewhere. The manuscript should be written in English or Korean. Ensure that online submission are in a standard word processing format. Corresponding author must write the manuscript using the JOET template provided in Hangul or MS Word format. Ensure that graphics are high-resolution. Be sure all necessary files have been uploaded/ attached.

Authors' checklist

Please refer to “Authors' Checklist” for details.

Article structure

Manuscript must be edited in the following order: (1) Title, (2) Authors' names and affiliations, (3) Keywords, (4) Abstract, (5) Nomenclature (optional), (6) Introduction, (7) Main body (analyses, tests, results, and discussions), (8) Conclusions, (9) Conflict of interest, (10) Funding (optional), (11) Acknowledgements (optional), (12) References, (13) Appendices (optional), (14) Author’s ORCIDs.

Abstract

A concise and factual abstract is required. The abstract should state briefly the background, purpose and methods of the research, the principal results and conclusions. An abstract should be written in 150-200 words. References are not cited in abstract whenever possible. Also, non-standard or uncommon abbreviations should be avoided, but if essential they must be defined at their first mention in the abstract itself.

Keywords

Immediately after the abstract, provide a maximum of 5 or 6 keywords.

Unit

Use the international system units(SI). If other units are mentioned, please give their equivalent in SI.

Equations

All mathematical equations should be c1early printed/typed using well accepted explanation. Superscripts and subscripts should be typed clearly above or below the base line. Equation numbers should be given in Arabic numerals enclosed in parentheses on the right-hand margin.

Tables

Tables should be numbered consecutively with Arabic numerals. Each table should be fully titled. All tables should be referred to in the texts.

Figures

Figures should be numbered consecutively with Arabic numerals. Each figure should be fully titled. All figures should be referred to in the texts. All the illustrations should be of high quality meeting with the publishing requirement with legible symbols and legends.

Conflict of interest

It should be disclosed here according to the statement in the Research and publication ethics regardless of existence of conflict of interest. If the authors have nothing to disclose, please state: “No potential

conflict of interest relevant to this article was reported."

Funding

Funding to the research should be provided here. Providing a FundRef ID is recommended including the name of the funding agency, country and if available, the number of the grant provided by the funding agency. If the funding agency does not have a FundRef ID, please ask that agency to contact the FundRef registry (e-mail: fundref.registry@crossref.org). Additional detailed policy of FundRef description is available from http://www.crossref.org/fundref/. Example of a funding description is as follows:

The study is supported by the Inha University research fund (FundRef ID: 10.13039/501100002632), and the Korea Health Personnel Licensing Examination Institute research fund (FundRef ID: 10.13039/501100003647).

Acknowledgments

Any persons that contributed to the study or the manuscript, but not meeting the requirements of an authorship could be placed here. For mentioning any persons or any organizations in this section, there should be a written permission from them.

References in text

References in texts follow the APA style. Authors can also see how references appear in manuscript text through the 'Template'.

Reference list

Reference list follows the APA style. Authors can see how references should be given in reference section through the 'Template'.

Appendices

The appendix is an optional section that can contain details and data supplemental to the main text. If there is more than an appendix, they should be identified as A, B, C, etc. Formulae and equations in appendices should be given separate numbering: Eq. (A1), Eq. (A2), etc.; in a subsequent appendix, Eq. (B1) and so on. Similarly for tables and figures: Table A1; Fig. A1, etc.

ORCID (Open Researcher and Contributor ID)

All authors are recommended to provide an ORCID. To obtain an ORCID, authors should register in the ORCID web site: http://orcid.org. Registration is free to every researcher in the world. Example of ORCID description is as follows:

Joonmo Choung: https://orcid.org/0000-0003-1407-9031

Peer review and publication process

The peer review process can be broadly summarized into three groups: author process, review process, and publishing process for accepted submissions. General scheme is presented in Figure 1.

Check-in process for review

If the manuscript does not fit the aims and scope of the Journal or does not adhere to the Instructions to Authors, it may be rejected immediately after receipt and without a review. Before reviewing, all submitted manuscripts are inspected by Similarity Check powered by iThenticate (https://www.crossref.org/services/similarity-check/), a plagiarism-screening tool. If a too high degree of similarity score is found, the Editorial Board will do a more profound content screening.

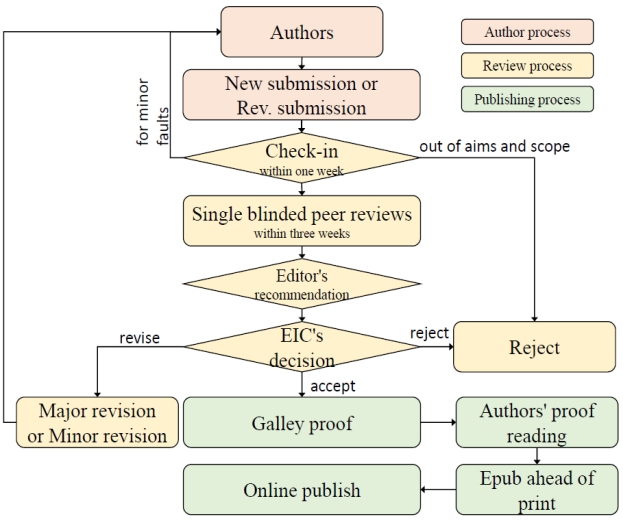

Figure 1 Flow chart of the peer review and publication process of JOET

The criterion for similarity rate for further screening is usually 15%; however, rather than the similarity rate, the Editorial Board focuses on cases where specific sentences or phrases are similar. The settings for Similarity Check screening are as follows: It excludes quotes, bibliography, small matches of 6 words, small sources of 1%, and the Methods section.

Number of reviewers

Reviewers will be selected from the list of reviewers. Manuscripts are then peer reviewed by at least 2 experts in the corresponding field, usually by 2.

Peer review process and the author response to the reviewer comments

JOET adopts single blind review, which means that the authors do not know the identity of the reviews. All papers, including those invited by the Editor, are subject to peer review.

The review period is 4 weeks. Usually the first decision is made within a week after completion of the review. The Editorial Board's decision after the review will be one of followings: Accept, Minor revision, Major revision, or Rejection. The Editorial Board may request the authors to revise the manuscript according to the reviewers' comments. If there are any requests for revision of the manuscript by the reviewers, the authors should do their best to revise the manuscript. If the reviewer's opinion is not acceptable or is believed to misinterpret the data, the author should reasonably indicate that. After revising the manuscript, the author should upload the revised files with a separate response sheet to each item of the reviewer's commentary. The author's revisions should be completed within 3 months after the request. If it is not received by the due date, the Editorial Board will notify the author. To extend the revision period beyond 3 months, the author should negotiate that with the Editorial Board. The manuscript review process can be provided for up two rounds. If the authors wish further review, the Editorial Board may consider it. The Editorial Board will make a final decision on the approval of the submitted manuscript for publication and can request any further corrections, revisions, and deletions of the article text if necessary. Statistical editing is also performed if the data requires professional statistical review by a statistician.

Processing after acceptance

If the manuscript is finally accepted, the galley proof will be sent to the corresponding author after professional manuscript editing and English proofreading. Proofreading should be performed for any misspellings or errors by the authors. Proofreading manuscript for publication is provided to the corresponding author, and the corresponding author must review the proofreading manuscript. Corresponding authors are responsible for the content of the proofreading manuscript and any errors. After final proofreading, the manuscript may appear at the journal homepage as an article in press with a unique DOI number for rapid communication. All published articles will be replaced by the replacement XML file and a final PDF.

Feedback after publication

If the authors or readers find any errors, or contents that should be revised, it can be requested from the Editorial Board. The Editorial Board may consider erratum, corrigendum or a retraction. If there are any revisions to the article, there will be a CrossMark description to announce the final draft. If there is a reader's opinion on the published article with the form of Letter to the editor, it will be forwarded to the authors. The authors can reply to the reader's letter. Letter to the editor and the author's reply may be also published.

How the journal handle complaints and appeals

The policy of JOET is primarily aimed at protecting the authors, reviewers, editors, and the publisher of the journal. If not described below, the process of handling complaints and appeals follows the guidelines of the Committee of Publication Ethics available from: https://publicationethics.org/appeals

- *Who complains or makes an appeal?*

Submitters, authors, reviewers, and readers may register complaints and appeals in a variety of cases as follows: falsification, fabrication, plagiarism, duplicate publication, authorship dispute, conflict of interest, ethical treatment of animals, informed consent, bias or unfair/inappropriate competitive acts, copyright, stolen data, defamation, and legal problem. If any individuals or institutions want to inform the cases, they can send a letter via the contact page on our website: https://www.joet.org/about/contact.php. For the complaints or appeals, concrete data with answers to all factual questions (who, when, where, what, how, why) should be provided.

- *Who is responsible to resolve and handle complaints and appeals?*

The Editorial Board or Editorial Office is responsible for them. A legal consultant or ethics editor may be able to help with the decision making.

- *What may be the consequence of remedy?*

It depends on the type or degree of misconduct. The consequence of resolution will follow the guidelines of the Committee of Publication Ethics (COPE).

Article processing charge

Payment due

Article processing charge (APC) covers the range of publishing services JOET provides. This includes provision of online tools for editors and authors, article production and hosting, and customer services. Upon editorial acceptance of an article for the regular review service and upon submission of an article for the fast review service, the corresponding author will be notified that payment is due.

APC

The APC up to 6 pages is ₩300,000 (or ＄300) and ₩650,000 (or ＄650) for the for the regular and fast review services, respectively. An extra APC of $100 per page is charged for papers longer than 6 pages, No taxes are included in this charge. For the fast review service, an advance fee of ₩250,000 ($250) should be paid on submission.

Payment methods

Credit card payment can be made online using a secure payment form as soon as the manuscript has been editorially accepted. We will we send a receipt by email once payment has been processed. Please note that payment by credit card carries a surcharge of 10% of the total APC.

Invoice payment is due within 7 days of the manuscript receiving editorial acceptance. Receipts are available on request.

JOET Template 2022.08.27

Journal of Ocean Engineering and Technology 00(0), 000-000, December, 2100
https://doi.org/10.26748/KSOE.2100.000
pISSN 1225-0767
eISSN 2287-6715

Original Research Article, Technical Article, Review Article, etc

Title of Article

Firstname Lastname[1], Firstname Lastname[2] and Firstname Lastname[3]

[1]*Professor, Department of OO, OO School, OO University, Busan, Korea*
[2]*Graduate Student, Department of OO, OO University, Seoul, Korea*
[3]*Senior Researcher, Department of OO, OO Engineering. Corp., Seoul, Korea*

KEYWORDS: Lumped mass line model, Explicit method, Steel lazy wave riser (Provide a maximum of 5 or 6 keywords.)

ABSTRACT:

Abstract Construction Guidelines
1) Describe the research background and aims in 1-2 sentences
2) Describe the research/analysis method (method section) in 2-3 sentences.
3) Describe the research/analysis results (results) in 2-3 sentences.
4) Describe the research conclusion in 1-2 sentences.
Abstract Editing Guidelines
1) Review English grammar.
2) Describe in 150-200 words.
3) When using an abbreviation or acronym, write the acronym after full words.
4) Abbreviations (acronyms) used only once should be written in full words only, and no acronyms.
5) References are not included in the abstract.

Nomenclature (Optional)

ITOC	Increment of total operating cost ($/yr)
LHV	Lower heating value (kJ/kg)
Pw	Power (kW)
T	Temperature (K)
V	Volume (m^3)
ρ	Density (kg/m^3)

1. Introduction

The introduction should briefly place the study in a broad context and highlight why it is important. It should define the purpose of the work and its significance. The current state of the research field should be reviewed carefully and key publications cited. Please highlight controversial and diverging hypotheses when necessary. Finally, briefly mention the main aim of the work and highlight the principal conclusions. As far as possible, please keep the introduction comprehensible to scientists outside your particular field of research.

Received 00 February 2100, revised 00 October 2100, accepted 00 October 2100
Corresponding author Firstname Lastname: +82-51-759-0656, e-mail@e-mail.com
It is a recommended paper from the proceedings of 2019 spring symposium of the Korea Marine Robot Technology (KMRTS).

2. General Information for Authors

2.1 Research and Publication Ethics

Authorship should be limited to those who have made a significant contribution to the conception, design, execution, or interpretation of the reported study. All those who have made significant contributions should be listed as co-authors. Where there are others who have participated in certain substantive aspects of the research project, they should be acknowledged or listed as contributors.

The corresponding author should ensure that all appropriate co-authors and no inappropriate co-authors are included on the paper, and that all co-authors have seen and approved the final version of the paper and have agreed to its submission for publication.

Details on publication ethics are found in the journal's website (http://joet.org/authors/ethics.php). For the policies on research and publication ethics not stated in the Instructions, Guidelines on Good Publication (http://publicationethics.org/) can be applied.

2.2 Requirement for Membership

One of the authors who submits a paper or papers should be member of The Korea Society of Ocean Engineers (KSOE), except a case that editorial board provides special admission of submission.

2.3 Publication Type

Article types include scholarly monographs (original research articles), technical articles (technical reports and data), and review articles. The paper should have not been submitted to another academic journal. When part or whole of a manuscript was already published to conference papers, research reports, and dissertations, then the corresponding author should note it clearly in the manuscript.

Example: It is noted that this paper is revised edition based on proceedings of KAOST 2100 in Jeju.

2.4 Copyright

After published to JOET, the copyright of manuscripts should belong to KSOE. A transfer of copyright (publishing agreement) form can be found in submission website (http://www.joet.org).

2.5 Manuscript Submission

Manuscript should be submitted through the on-line submission website (http://www.joet.org). The date that manuscript was received through on-line website is the official date of receipt. Other correspondences can be sent by an email to the Editor in Chief or secretariat. The manuscript must be accompanied by a signed statement that it has been neither published nor currently submitted for publication elsewhere. The manuscript should be written in English or Korean. Ensure that online submission is in a standard word processing format. Corresponding author must write the manuscript using the JOET template provided in Hangul or MS Word format. Ensure that graphics are high-resolution. Be sure all necessary files have been uploaded/ attached.

2.5.1 Authoer’s checklist

Authoer’s checklist and Transfer of copyright can be found in submission homepage (http:/www.joet.org).

3. Manuscript

Manuscript must be edited in the following order: (1) Title, (2) Authors' names and affiliations, (3) Keywords, (4) Abstract, (5) Nomenclature (optional), (6) Introduction, (7) Main body (analyses, tests, results, and discussions), (8) Conclusions, (9) Conflict of interest, (10) Funding (optional), (11) Acknowledgements (optional), (12) References, (13) Appendices (optional), (14) Author’s ORCIDs.

3.1 Unit

Use the international system units (SI). If other units are mentioned, please give their equivalent in SI.

3.2 Equations

All mathematical equations should be clearly printed/typed using well accepted explanation. Superscripts and subscripts should be typed clearly above or below the base line. Equation numbers should be given in Arabic numerals enclosed in parentheses on the right-hand margin. The parameters used in equation must be defined. They should be cited in the text as, for example, Eq. (1), or Eqs. (1)–(3).

$$G_{GEV}(x;\mu,\sigma,\xi)=\begin{cases}\exp[-(1+\xi(x-\mu)/\sigma)^{-1/\xi}] & \xi\neq 0\\ \exp[-\exp(-(x-\mu)/\sigma)] & \xi=0\end{cases} \quad (1)$$

in which μ, σ, and ξ represent the location ("Shift" in figures), scale, and shape parameters, respectively.

3.3 Tables

Tables should be numbered consecutively with Arabic numerals. Each table should be typed on a separate sheet of paper and be fully titled. All tables should be referred to in the texts.

Table 1 Tables should be placed in the main text near to the first time they are cited

Item	Buoyancy riser
Segment length[1)] (m)	370
Outer diameter (m)	1.137
Inner diameter (m)	0.406
Dry weight (kg/m)	697
Bending rigidity ($N\cdot m^2$)	1.66E8
Axial stiffness (N)	7.098E9
Inner flow density ($kg\cdot m^3$)	881
Seabed stiffness ($N/m/m^2$)	6,000

[1)]Tables may have a footer.

3.4 Figures

Figures should be numbered consecutively with Arabic numerals. Each figure should be fully titled. All the illustrations should be of high quality meeting with the publishing requirement with legible symbols and legends. All figures should be referred to in the texts. They should be referred to in the text as, for example, Fig. 1, or Figs. 1−3.

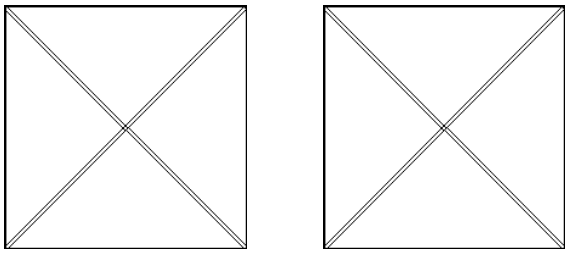

(a) (b)

Fig. 1 Schemes follow the same formatting. If there are multiple panels, they should be listed as: (a) Description of what is contained in the first panel; (b) Description of what is contained in the second panel. Figures should be placed in the main text near to the first time they are cited

3.5 How to Describe the References in Main Texts

- JOET recommends to edit authors' references using MS-Word reference or ZOTERO plug-in
- How to add a new citation and source to a document using MS-Word is found in MS Office web page: https://support.microsoft.com/en-us/office/add-citations-in-a-word-document-ab9322bb-a8d3-47f4-80c8-63c06779f127
- How to add a new citation and source to a document using ZOTERO is found in zotero web page: https://www.zotero.org/

4. Results

This section may be divided by subheadings. It should provide a concise and precise description of the experimental results, their interpretation as well as the experimental conclusions that can be drawn. Tables and figures are recommended to present the results more rapidly and easily. Do not duplicate the content of a table or a figure with in the Results section. Briefly describe the core results related to the conclusion in the text when data are provided in tables or in figures. Supplementary results can be placed in the Appendix.

5. Discussion

Authors should discuss the results and how they can be interpreted in perspective of previous studies and of the working hypotheses. The findings and their implications should be discussed in the broadest context possible. Future research directions may also be highlighted

6. Conclusions

This section can be added to the manuscript.

Conflict of Interest

It should be disclosed here according to the statement in the Research and publication ethics regardless of existence of conflict of interest. If the authors have nothing to disclose, please state: “No potential conflict of interest relevant to this article was reported.”, “The authors declare no potential conflict of interest.”, “The authors declare that they have no conflict of interests.”

Funding (Optional)

Please add: “This research was funded by Name of Funder, grant number XXX” and “The OOO was funded by XXX”. Check carefully that the details given are accurate and use the standard spelling of funding agency names at https://search.crossref.org/funding

Acknowledgments (Optional)

In this section you can acknowledge any support given which is not covered by the author contribution or funding sections. This may include administrative and technical support, or donations in kind (e.g., materials used for experiments). For mentioning any persons or any organizations in this section, there should be a written permission from them.

References

JOET follows the American Psychological Association (APA) style.

- Some samples are found in following web pages: https://apastyle.apa.org/style-grammar-guidelines/references/examples or https://www.ntnu.edu/viko/apa-examples
- JOET recommends editing authors’ references using MS-Word reference or ZOTERO plug-in
- How to add a new citation and source to a document using MS-Word is found in MS Office web page: https://support.microsoft.com/en-us/office/add-citations-in-a-word-document-ab9322bb-a8d3-47f4-80c8-63c06779f127
- How to add a new citation and source to a document using ZOTERO is found in ZOTERO web page: https://www.zotero.org/

Appendix (Optional)

The appendix is an optional section that can contain details and data supplemental to the main text. For example, explanations of experimental details that would disrupt the flow of the main text, but nonetheless remain crucial to understanding and reproducing the research shown; figures of replicates for experiments of which representative data is shown in the main text can be added here if brief, or as Supplementary data. Mathematical proofs of results not central to the paper can be added as an appendix.

All appendix sections must be cited in the main text. In the appendixes, Figures, Tables, etc. should be labeled starting with ‘A’, e.g., Fig. A1, Fig. A2, etc.

Examples:

https://doi.org/10.26748/KSOE.2019.022

https://doi.org/10.26748/KSOE.2018.4.32.2.095

Author ORCIDs

All authors are recommended to provide an ORCID. To obtain an ORCID, authors should register in the ORCID web site: http://orcid.org. Registration is free to every researcher in the world. Example of ORCID description is as follows:

Author name	**ORCID**
So, Hee	0000-0000-000-00X
Park, Hye-Il	0000-0000-000-00X
Yoo, All	0000-0000-000-00X
Jung, Jewerly	0000-0000-000-00X

Authors' Checklist

The following list will be useful during the final checking of a manuscript prior to sending it to the journal for review. Please submit this checklist to the KSOE when you submit your article.

< Checklist for manuscript preparation >

☐ I checked my manuscript has been 'spell-checked' and 'grammar-checked'.

☐ One author has been designated as the corresponding author with contact details such as
- E-mail address
- Phone numbers

☐ I checked abstract 1) stated briefly the purpose of the research, the principal results and major conclusions, 2) was written in 150−200 words, and 3) did not contain references (but if essential, then cite the author(s) and year(s)).

☐ I provided 5 or 6 keywords.

☐ I checked color figures were clearly marked as being intended for color reproduction on the Web and in print, or to be reproduced in color on the Web and in black-and-white in print.

☐ I checked all table and figure numbered consecutively in accordance with their appearance in the text.

☐ I checked abbreviations were defined at their first mention there and used with consistency throughout the article.

☐ I checked all references mentioned in the Reference list were cited in the text, and vice versa according to the APA style.

☐ I checked I used the international system units (SI) or SI-equivalent engineering units.

< Authorship checklist >

JOET considers individuals who meet all of the following criteria to be authors:

☐ Made a significant intellectual contribution to the theoretical development, system or experimental design, prototype development, and/or the analysis and interpretation of data associated with the work contained in the article.

☐ Contributed to drafting the article or reviewing and/or revising it for intellectual content.

☐ Approved the final version of the article as accepted for publication, including references.

< Checklist for publication ethics >

☐ I checked the work described has not been published previously (except in the form of an abstract or as a part of a published lecture or academic thesis).

☐ I checked when the work described has been published previously in other proceedings without copyright, it has clearly noted in the text.

☐ I checked permission has been obtained for use of copyrighted material from other sources including the Web.

☐ I have processed Plasgiarism Prevention Check through reliable web sites such as www.kci.go.kr, http://www.ithenticate.com/, or https://www.copykiller.org/ for my submission.

☐ I agree that final decision for my final manuscript can be changed according to results of Plasgiarism Prevention Check by JOET administrator.

☐ I checked one author at least is member of the Korean Society of Ocean Engineers.

☐ I agreed all policies related to 'Research and Publication Ethics'

☐ I agreed to transfer copyright to the publisher as part of a journal publishing agreement and this article will not be published elsewhere including electronically in the same form, in English or in any other language, without the written consent of the copyright-holder.

☐ I made a payment for reviewing of the manuscript, and I will make a payment for publication on acceptance of the article.

☐ I have read and agree to the terms of Authors' Checklist.

Title of article	:	
Date of submission	: DD/MM/YYYY	
Corresponding author	:	signature
Email address	:	

※ E-mail this with your signature to ksoehj@ksoe.or.kr

Publishing Agreement

ARTICLE DETAILS

Title of article :

Corresponding author :

E-mail address :

DOI : https://doi.org/10.26748/KSOE.2XXX.XXX

YOUR STATUS

I am one author signing on behalf of all co-authors of the manuscript.

ASSIGNMENT OF COPYRIGHT

I hereby assign to the Korean Society of Ocean Engineers, the copyright in the manuscript identified above and any tables, illustrations or other material submitted for publication as part of the manuscript (the "Article"). This assignment of rights means that I have granted to Korean Society of Ocean Engineers the exclusive right to publish and reproduce the Article, or any part of the Article, in print, electronic and all other media (whether now known or later developed), in any form, in all languages, throughout the world, for the full term of copyright, and the right to license others to do the same, effective when the Article is accepted for publication. This includes the right to enforce the rights granted hereunder against third parties.

SCHOLARLY COMMUNICATION RIGHTS

I understand that no rights in patents, trademarks or other intellectual property rights are transferred to the Journal owner. As the author of the Article, I understand that I shall have: (i) the same rights to reuse the Article as those allowed to third party users of the Article under the CC-BY-NC License, as well as (ii) the right to use the Article in a subsequent compilation of my works or to extend the Article to book length form, to include the Article in a thesis or dissertation, or otherwise to use or re-use portions or excerpts in other works, for both commercial and non-commercial purposes. Except for such uses, I understand that the assignment of copyright to the Journal owner gives the Journal owner the exclusive right to make or sub-license commercial use.

USER RIGHTS

The publisher will apply the Creative Commons Attribution-Noncommercial Works 4.0 International License (CC-BY-NC) to the Article where it publishes the Article in the journal on its online platforms on an Open Access basis.

The CC-BY-NC license allows users to copy and distribute the Article, provided this is not done for commercial purposes and further does not permit distribution of the Article if it is changed or edited in any way, and provided the user gives appropriate credit (with a link to the formal publication through the relevant DOI), provides a link to the license, and that the licensor is not represented as endorsing the use made of the work. The full details of the license are available at http://creativecommons.org/licenses/by-nc/4.0/legalcode.

REVERSION OF RIGHTS

Articles may sometimes be accepted for publication but later rejected in the publication process, even in some cases after public posting in "Articles in Press" form, in which case all rights will revert to the author.

☑ I have read and agree to the terms of the Journal Publishing Agreement.

Corresponding author:

name signature

※ E-mail this with your signature to ksoehj@ksoe.or.kr (Papers will not be published unless this form is signed and returned)

Research and Publication Ethics

Journal of Ocean Engineering and Technology (JOET) adheres to the guidelines published by professional organizations, including Committee on Publication Ethics (COPE; https://publicationethics.org/)

1. Authorship

JOET considers individuals who meet all of the following criteria to be authors:

1) Made a significant intellectual contribution to the theoretical development, system or experimental design, prototype development, and/or the analysis and interpretation of data associated with the work contained in the article.
2) Contributed to drafting the article or reviewing and/or revising it for intellectual content.
3) Approved the final version of the article as accepted for publication, including references.

Contributors who do not meet all of the above criteria may be included in the Acknowledgment section of the article. Omitting an author who contributed to your article or including a person who did not fulfill all of the above requirements is considered a breach of publishing ethics.

Correction of authorship after publication: JOET does not correct authorship after publication unless a mistake has been made by the editorial staff.

2. Originality and Duplicate Publication

All submitted manuscripts should be original and should not be in consideration by other scientific journals for publication. Any part of the accepted manuscript should not be duplicated in any other scientific journal without permission of the Editorial Board, although the figures and tables can be used freely if the original source is verified according to the Creative Commons Attribution License (CC BY-NC). It is mandatory for all authors to resolve any copyright issues when citing a figure or table from other journal that is not open access.

3. Conflict-of-Interest Statement

Conflict of interest exists when an author or the author's institution, reviewer, or editor has financial or personal relationships that inappropriately influence or bias his or her actions. Such relationships are also known as dual commitments, competing interests, or competing loyalties. These relationships vary from being negligible to having a great potential for influencing judgment. Not all relationships represent true conflict of interest. On the other hand, the potential for conflict of interest can exist regardless of whether an individual believes that the relationship affects his or her scientific judgment. Financial relationships such as employment, consultancies, stock ownership, honoraria, and paid expert testimony are the most easily identifiable conflicts of interest and the most likely to undermine the credibility of the journal, the authors, or of the science itself. Conflicts can occur for other reasons as well, such as personal relationships, academic competition, and intellectual passion. If there are any conflicts of interest, authors should disclose them in the manuscript. The conflicts of interest may occur during the research process as well; however, it is important to provide disclosure. If there is a disclosure, editors, reviewers, and reader can approach the manuscript after understanding the situation and the background of the completed research.

4. Management Procedures for the Research and Publication Misconduct

When JOET faces suspected cases of research and publication misconduct such as a redundant (duplicate) publication, plagiarism, fabricated data, changes in authorship, undisclosed conflicts of interest, an ethical problem discovered with the submitted manuscript, a reviewer who has appropriated an author's idea or data, complaints against editors, and other issues, the resolving process will follow the flowchart provided by the Committee on Publication Ethics (http://publicationethics.org/resources/flowcharts). The Editorial Board of JOET will discuss the suspected cases and reach a decision. JOET will not hesitate to publish errata, corrigenda, clarifications, retractions, and apologies when needed.

5. Editorial Responsibilities

The Editorial Board will continuously work to monitor and safeguard publication ethics: guidelines for retracting articles; maintenance of the integrity of the academic record; preclusion of business needs from compromising intellectual and ethical standards; publishing corrections, clarifications, retractions, and apologies when needed; and excluding plagiarism and fraudulent data. The editors maintain the following responsibilities: responsibility and authority to reject and accept articles; avoiding any conflict of interest with respect to articles they reject or accept; promoting publication of corrections or retractions when errors are found; and preservation of the anonymity of reviewers.

6. Hazards and human or animal subjects

If the work involves chemicals, procedures or equipment that have any unusual hazards inherent in their use, the author must clearly identify these in the manuscript. If the work involves the use of animal or human subjects, the author should ensure that the manuscript contains a statement that all procedures were performed in compliance with relevant laws and institutional guidelines and that the appropriate institutional committee(s) has approved them. Authors should include a statement in the manuscript that informed consent was obtained for experimentation with human subjects. The privacy rights of human subjects must always be observed.

Ensure correct use of the terms sex (when reporting biological factors) and gender (identity, psychosocial or cultural factors), and, unless inappropriate, report the sex and/or gender of study participants, the sex of animals or cells, and describe the methods used to determine sex and gender. If the study was done involving an exclusive population, for example in only one sex, authors should justify why, except in obvious cases. Authors should define how they determined race or ethnicity and justify their relevance.

7. Secondary publication

It is possible to republish manuscripts if the manuscripts satisfy the conditions of secondary publication. These are:

- The authors have received approval from the Editorial Board of both journals (the editor concerned with the secondary publication must have access to the primary version).
- The priority for the primary publication is respected by a publication interval negotiated by editors of both journals and the authors.
- The paper for secondary publication is intended for a different group of readers
- The secondary version faithfully reflects the data and interpretations of the primary version.
- The secondary version informs readers, peers, and documenting agencies that the paper has been published in whole or in part elsewhere, for example, with a note that might read, "This article is based on a study first reported in the [journal title, with full reference]"
- The title of the secondary publication should indicate that it is a secondary publication (complete or abridged republication or translation) of a primary publication.

8. Complaints and Appeals

The process of handling complaints and appeals follows the guidelines of the COPE available from: https://publicationethics. org/appeals

9. Post-publication discussions and corrections

The post-publication discussion is available through letter to editor. If any readers have a concern on any articles published, they can submit letter to editor on the articles. If there found any errors or mistakes in the article, it can be corrected through errata, corrigenda, or retraction.

The Korean Society of Ocean Engineers